DEUTSCHES ELEKTRONEN-SYNCHROTRON

DESY-THESIS-2001-014 (nicht online)
March 2001

Creation of Free Excitons in Solid Krypton Investigated by Time-Resolved Luminescence Spectroscopy

by

V. Kisand

ISSN 1435-8085

NOTKESTRASSE 85 - 22607 HAMBURG

To be sure that your reports and preprints are promptly included in the HEP literature database
send them to (if possible by air mail):

DESY
Zentralbibliothek
Notkestraße 85
22603 Hamburg
Germany

DESY
Bibliothek
Platanenallee 6
15738 Zeuthen
Germany

Creation of Free Excitons in Solid Krypton Investigated by Time-Resolved Luminescence Spectroscopy

DISSERTATION
zur Erlangung des Doktorgrades
des Fachbereichs Physik
der Universität Hamburg

vorgelegt von
Vambola Kisand
aus Põlva

Hamburg
2001

Gutachter der Dissertation:	Prof. Dr. G. Zimmerer Prof. Dr. U. Merkt
Gutachter der Disputation:	Prof. Dr. G. Zimmerer Prof. Dr. G. Huber
Datum der Disputation:	16.03.2001
Dekan des Fachbereichs Physik und Vorsitzender des Promotionsausschusses:	Prof. Dr. F.W. Büßer

Abstract

The creation and relaxation of secondary excitons in solid Kr were investigated using energy- and time-resolved luminescence spectroscopy in vacuum ultraviolet region. The spectrally selected luminescence of the free exciton (FE) was used as a probe for secondary exciton creation. This was possible due to the good 'quality' of the samples and high purity Kr gas, used for sample growth, since the intensity of the free exciton emission line is extremely sample sensitive.

For the first time, time-resolved excitation spectra and decay curves of free exciton emission in solid Kr were systematically investigated for an excitation exceeding the band gap energy (up to 35 eV). Also luminescence of self-trapped excitons was studied in solid Kr using time-resolved methods. Additionally, high-resolution reflection spectra were measured and a new member (n=5) of the exciton series was revealed. A series of samples were grown and investigated, demonstrating a good reproducibility of the main experimental results.

Delayed electron-hole recombination and 'prompt' (in the meaning of the time-resolution of experimental set-up) creation of secondary excitons were separated using the time-resolved experimental technique. A detailed model for the dynamics of electron-hole recombination into the FE state was developed. The delayed component of the free exciton decay curve was reproduced with model calculations including thermalization of the carriers via scattering on acoustic phonons and the effect of recombination cross-section, which depends on the actual carrier temperatures. A reasonable agreement between experiment and theory was found.

Time-resolved excitation spectra show that the 'prompt' creation of FE takes place in the region above the threshold $h\nu=E_{th}$ $\approx$21.7 eV. The shape of the decay curves changes significantly above this threshold as well. The experimental threshold value is nearly equal to the sum of the band gap energy and the free exciton energy ($E_{th}=E_g+E_{ex}$). In order to explain the threshold in time-resolved excitation spectra of 'prompt' processes two possibilities are discussed: (i) inelastic scattering of the electrons in the framework of the multiple-parabolic-branch band model, and (ii) creation of the electronic polaron complex. 'Prompt' creation of excitons above E_{th} is ascribed to a superposition of both processes. At threshold itself, the creation of electronic polaron complexes is the dominant process, while at higher excitation energies, electron-electron scattering may dominate.

Erzeugung freier Exzitonen in festem Krypton, untersucht mit Hilfe der zeitaufgelösten Lumineszenzspektroskopie

Kurzfassung

Die Erzeugung und Relaxation sekundärer Exzitonen in festem Kr wurde mittels zeit- und energieaufgelöster Lumineszenzspektroskopie im vakuumultravioletten Spektralbereich untersucht. Zur Charakterisierung der Erzeugung sekundärer Exzitonen wurde die spektral ausgewählte Lumineszenz des freien Exzitons (FE) herangezogen. Dies war aufgrund der hohen Probenqualität und der hohen Reinheit des zur Probenpräparation verwendeten Kr-Gases möglich, da die Intensität der freien Exzitonlinie stark von der Probengüte abhängt.

Zum ersten Mal wurden zeitaufgelöste Anregungsspektren und Abklingkurven der FE-Emission in festem Kr für Anregungen oberhalb der Bandkante (bis 35 eV) systematisch untersucht. Zusätzlich wurde auch die Lumineszenz von lokalisierten ('self-trapped') Exzitonen in festem Kr durch zeitaufgelöste Spektroskopie betrachtet. Weiterhin wurden hochaufgelöste Reflexionsspektren gemessen und daraus ein weiteres Element der Exzitonenserie (n=5) bestimmt. Die Messungen wurden an verschiedenen Proben wiederholt und zeigen eine gute Reproduzierbarkeit der experimentellen Ergebnisse.

Mittels der zeitaufgelösten Meßtechnik kann zwischen verzögerter Elektron-Loch-Rekombination und 'prompter' (im Rahmen der experimentellen Zeitauflösung) Erzeugung sekundärer Exzitonen unterschieden werden. Es wurde ein detailliertes Modell der Dynamik der Elektron-Loch-Rekombination in den FE-Zustand aufgestellt. Die verzögerte Komponente der Abklingkurven für das FE wurde mittels Modellrechnungen reproduziert, die die Thermalisierung der Ladungsträger durch Streuung an akustischen Phononen beinhalten und die Abhängigkeit des Wirkungsquerschnittes der Rekombination von der Ladungsträgertemperatur berücksichtigen. Modellrechnungen und experimentelle Daten weisen eine gute Übereinstimmung auf.

Die zeitaufgelösten Anregungsspekten zeigen, daß eine 'prompte' Erzeugung des FE im Bereich oberhalb der Schwelle von $h\nu=E_{th}$ $\approx$21.7 eV statt findet. Dies spiegelt sich ebenfalls in der veränderten Form der Abklingkurven oberhalb der Schwelle wider. Der experimentelle Schwellenwert entspricht nahezu der Summe der Bandlückenenergie und der Energie des FE ($E_{th}=E_g+E_{ex}$). Zur Erklärung dieses Schwellenwertes werden zwei Modelle diskutiert: (i) inelastische Streuung der Elektronen im Rahmen des *'multiple-parabolic-branch band'* Modells, und (ii) Erzeugung des elektronischen Polaron-Komplexes. Die 'prompte' Erzeugung von Exzitonen oberhalb von E_{th} wird einer Überlagerung aus beiden Prozessen zugeordnet. Nahe an der Schwelle ist die Erzeugung des elektronischen Polaron-Komplexes der dominante Prozess, während Elektron-Elektron-Streuung bei höheren Anregungsenergien überwiegen könnte.

Contents

Chapter 1

Introduction

Energy dissipation in solids following primary excitation by X-rays or high-energy particles (electrons, ions) is one of fundamental problems in condensed matter physics. A detailed understanding of dissipative processes is very important for practical applications, *e.g.* development of displays, scintillators for high energy physics, computer tomography *etc.*, as well.

A high-energy core-excitation typically causes a relaxation cascade, where energy dissipation at first occurs via Auger processes, electron-electron and electron-hole scattering. After some time, in each insulator a situation is reached, in which further Auger relaxation is not any more energetically possible. Nevertheless, 'hot' electrons (or holes) still have sufficient kinetic energy for the creation of electron-hole pairs or excitons (bound electron-hole pairs).

Such a situation is the starting point of the present work. In this thesis, the final steps of 'high-energy' excitation relaxation cascades are under investigation in solid krypton. However, the 'hot' electrons are created directly, using spectrally selected synchrotron radiation with a photon energy up to $\sim$35 eV. An adjustable energy of exciting photons offers the possibility to tune the kinetic energy of electrons. The time-structure of the DORIS storage ring is particularly suitable for time-resolved spectroscopy and gives a good possibility to investigate the time-evolution of relaxation processes from sub-ns to the μs regime.

Solid Kr, like other rare gas solids (RGS), is one of the simplest solids, and therefore it is an ideal model substance. The peculiar properties of RGS are a consequence of the closed shell electronic configuration of the atoms (He:$1s^2$; Ne to Xe ns^2np^6, n=2,...,5). The binding energies of the valence electrons are so large that the closed-shell nature of the atoms is conserved in the condensed phase, in which the atoms are held together by Van der Waals forces. As a result of the high ionization energy of atoms, RGS are dielectrics with extremely large forbidden gaps (for solid Kr: E_g=11.59 eV). Kr crystals exhibit simultaneously strong

broad-band self-trapped exciton (STE) luminescence as well as considerable narrow-band luminescence of the free excitons (FE). In the present work, both narrow-band emission from the lowest FE state and the singlet ($^1\Sigma_u^+$) component of the STE emission are used as probes.

The main purpose of the present work is an investigation of the different exciton creation processes in the case of photoexcitation, where the photon energy is exceeding the band gap energy. First of all, an understanding of such processes requires knowledge about creation and decay of excitons, excited directly in the excitonic region. Studies about this most direct FE creation process in solid Kr have been performed earlier [Var94]. Nevertheless, experiments concerning FE creation with excitation in the excitonic region are repeated in the present work. A new aspect is the use of high purity Kr, which permits to investigate luminescence of solid Kr without disturbing emission of Xe impurity.

Using photoexcitation with a photon energy exceeding the band gap energy, it is feasible to create directly (*i.e.* in a one step process) electron-hole pairs. Moreover, a photocreated electron in the conduction band has the possibility to create secondary electronic excitations (excitons or electron-hole pairs) via electron-electron scattering. In RGS, the width of the valence band (2.3 eV in Kr) is much smaller than the band gap energy (E_g=11.59 eV in Kr) and therefore, 'hot' holes cannot create any secondary electronic excitations. Additionally to electron-electron scattering, a more sophisticated possibility exists, where two excitations (*e.g.* electron-hole pair plus exciton) are formed directly in a one step photoexcitation process (electronic polaron complex). Electron-electron scattering as well as creation of an electronic polaron complex only take place above a certain threshold energy of primary photoexcitation.

If the kinetic energy of the electron does not exceed the threshold energy for electron-electron scattering, relaxation via electron-phonon scattering occurs. Due to the very simple crystal structure, only acoustic phonons exist in RGS. Hence, the phonon-assisted relaxation processes are much slower than in systems with optical phonons. Therefore, in solid Kr, thermalization of electrons takes place in a nanosecond time-range. After thermalization, the exciton creation through electron-hole recombination becomes possible.

All such processes are under investigation in this thesis. Thereby, the usage of time-resolved techniques is very important, since it directly allows to discriminate between 'slow' phonon-assisted, and 'prompt' (in the meaning of the time-resolution of experimental set-up) FE creation processes.

The present work is divided into the following chapters. In chapter 2, the experimental set-up is described including its optical and electronic components, also the applied spectroscopic methods and a preparation technique for solid Kr samples are introduced. In chapter

3, a short overview about the properties of solid Kr is given and different excitonic effects are described. Different possibilities for creation of excitons are also discussed. A detailed model for the dynamics of electron-hole recombination into the FE state is introduced as well. In chapter 4, the experimental data of time-resolved luminescence spectroscopy are presented and discussed. Moreover, the fitting results of experimental decay curves are presented. The results of the present work are compared with results of other experimental studies known from the literature. In the summary, the main conclusions are resumed.

Chapter 2

Experiment

The experiments of the present work were carried out at the experimental station SUPERLUMI located in HASYLAB (*Hamburger Synchrotronstrahlungslabor*) at DESY (*Deutsches Elektronen-Synchrotron*). In this chapter, a short review of the SUPERLUMI set-up is given and also some important experimental aspects are discussed, especially essential for the experiments with rare gas solids (RGS). SUPERLUMI is a complex experimental station for time- and energy-resolved vacuum ultraviolet (VUV) luminescence spectroscopy. Photons with energy from 3.7 to 40 eV are available for photoexcitation. Three different secondary monochromators coupled with various detectors are accessible for the analysis of the luminescence. Luminescence photons can be detected between energies of 1.8 eV and 25 eV. It is also feasible to measure reflection spectra from the sample at the angle of incidence 17.5°. In VUV spectral region, all materials (including air) have extremely high absorption coefficient. Therefore the light path from the source to the experimental chamber and the experimental chamber itself are pumped down to ultra high vacuum (UHV) conditions. The SUPERLUMI set-up offers also possibilities to work at low temperatures (a flow-type helium cryostat), which is a necessary presumption for the investigations of RGS. A gas inlet system and *in situ* crystal growing system have been built for the RGS experiments at SUPERLUMI.

Several Ph.D. and diploma thesis and papers containing information about SUPERLUMI have been published earlier: [WBHS83] (beamline), [Roi84] (primary monochromator, single-photon counting), [MKZ85] (high-resolution VUV-2 monochromator), [GRZP83] (high-flux VUV-1 monochromator), [Hag89] (position sensitive detector for VUV region), [Kam89] (mechanical chopper), [Bec97] (BM/50 monochromator with position sensitive detector for visible region), [Kör97] (microsphere plate detector).

2.1 Synchrotron radiation

Synchrotron radiation (SR) is a very bright, broad band, polarized, pulsed light source extending from the infrared to the x-ray region. Most of the studies in VUV range are carried out by means of SR. It is well known from classical theory of electrodynamics that charges, moving with acceleration, emit electromagnetic radiation. In the case of synchrotron radiation, relativistic electrons (or positrons like in DORIS III) are accelerated in a circular orbit and emit electromagnetic radiation in a broad spectral range. The total intensity and distribution of the radiation depend on the energy and the number of the charged particles. Synchrotron radiation was observed for the first time in 1947 by Elder *et al.* [EGLP47]. General reviews about the development of the field of SR have been given by Kunz *et al.* [Kun79] and Margaritondo [Mar88]. The properties of SR make it superior to other light sources in many respects.

State of the art of modern technology is applied in constructing storage rings for particles which produce SR. Various magnets keep the electron or positron bunches circulating under UHV ($\sim 10^{-10}$ Torr) conditions for several hours, before a new filling of the storage ring takes place from an injection device. The total radiated power from the ring is given by

$$P(kW) = 8.85 \cdot 10^{-2} \cdot \frac{E^4(GeV)}{R(m)} I(mA)\,, \tag{2.1}$$

where E is the energy of the particles (4.45 GeV is typical for DORIS III), R is the radius of curvature of bending magnets (12.2 m for DORIS III) and I is the circulating current (average value for DORIS III is 100 mA) in respective units. The radiated power is distributed continuously over a wide spectral range. Half of the power is radiated below the critical wavelength λ_c of the storage ring given by

$$\lambda_c = \frac{4\pi R}{3\gamma^3} \tag{2.2}$$

and the second half above, where γ is the energy of the particle divided by its rest mass [SE98]. The critical wavelength is 0.75 Å (*i.e.* 16 keV in the energy scale) for DORIS III. In the case of accelerated electrons (or positrons) the total number of photons emitted over all vertical angles per one milliradian of orbit per second, for 0.1 % bandwidth, is given by

$$N(\lambda) = 2.23 \cdot 10^{10} \cdot I(mA) \cdot E(GeV) \cdot G(\lambda_c/\lambda), \tag{2.3}$$

where $G(\lambda_c/\lambda)$ is a universal function given analytically in terms of the modified Bessel function [CG90]. The typical flux from a bending magnet of DORIS III at its maximum

reaches about $4 \cdot 10^{13}$ photons per second, mrad^2 and 0.1 % bandwidth at 100 mA of storage ring current. The synchrotron sources provide linearly polarized light in the orbit plane and elliptically polarized light above and below that plane. A typical duration of the synchrotron light pulse is about 100 ps whereas the time interval between pulses extends from ns to μs in different facilities.

2.2 Light source and beamline

Due to the relatively long storage ring circumference (289.2 m), DORIS III has a special time-structure, which is particularly suitable for the time-resolved spectroscopy. DORIS provides light-pulses with the FWHM 130 ps and a period of 964 ns in *single bunch mode*. Normally DORIS is filled with 5 bunches with the same FWHM (130 ps) (*multi bunch mode)*. Then, the interval between the first and the last (fifth) bunch is 196 ns and between all others is 192 ns.

The SUPERLUMI set-up (Fig. 2.1) is located above the DORIS III storage ring plane at the beamline I. Two mirrors are used to illuminate the entrance slit of the primary monochromator [WBHS83]. The first, a cylindrical water-cooled mirror (M1, located in the plane of orbit, not shown in Fig. 2.1) accepts 50 mrad of the horizontal and 2.2 mrad vertical divergence of the source. The mirror M1 focuses light horizontally to a 10 mm wide image at the entrance slit of the primary monochromator. The second, a plane elliptic mirror (M2, located 3.7 m above storage ring plane, on a level of the entrance slit) does the same vertically providing an 0.1 mm high image at the entrance slit of the primary monochromator. The light is dispersed in the vertical direction by the primary monochromator. A third rotational-elliptic mirror (M3, located in the sample chamber) focuses the dispersed light onto the sample. As a result the 6×2 mm^2 light source transforms into the 4×0.15 mm^2 light spot on the sample.

2.3 Monochromators at SUPERLUMI

The SUPERLUMI set-up consists of 4 monochromators: the primary dispersing SR and three for analysis of luminescence. Such a combination of spectrometers meets nearly all wishes of physicists working with wide band gap materials. A comparison of the monochromator characteristics is presented in table 2.1.

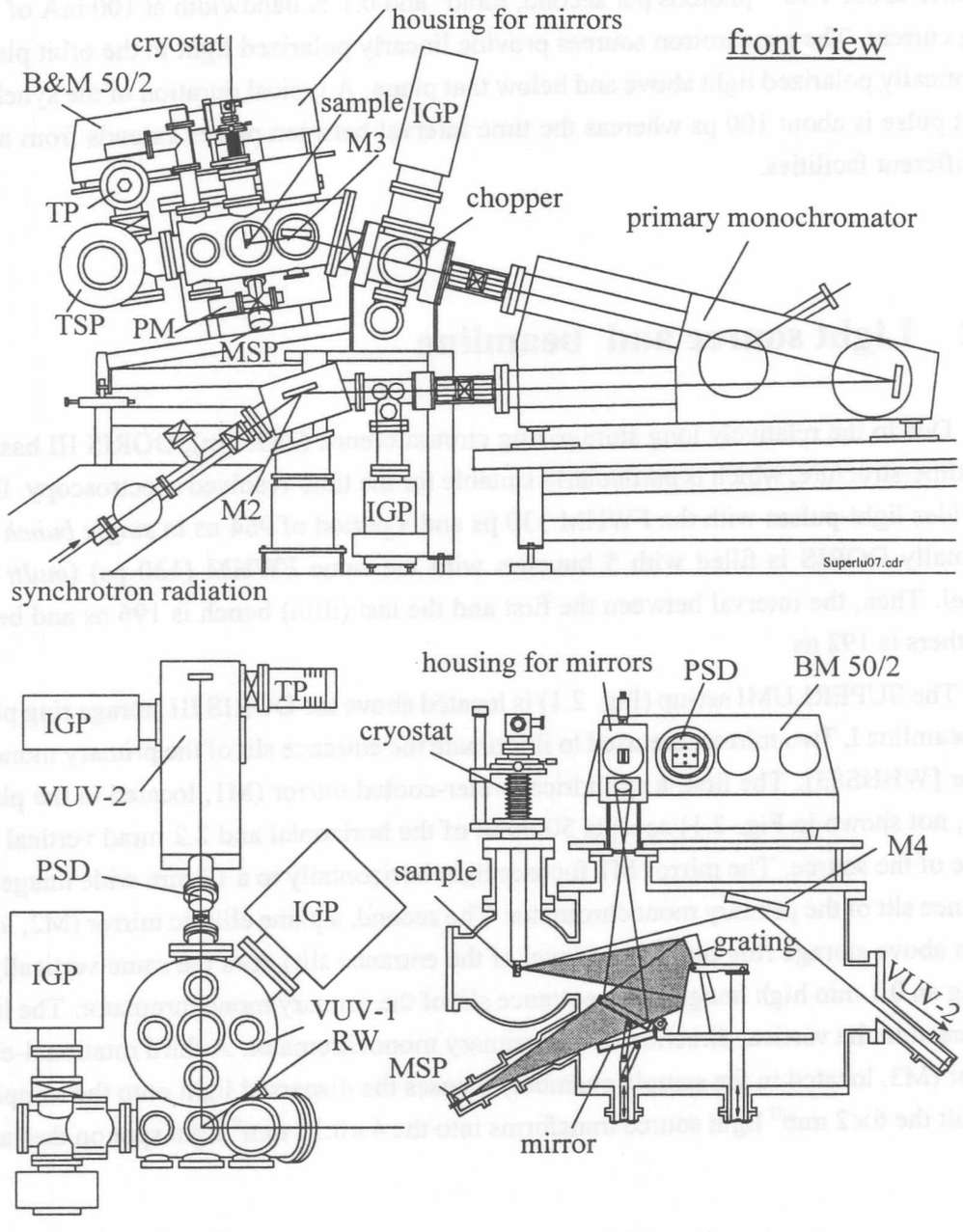

Figure 2.1: *SUPERLUMI set-up. TP: turbomolecular pump, TSP: titanium sublimation pump, MSP: microsphere plate detector, PM: photomultiplier, IGP: ion-getterpump, RW: reflection window, PSD: position sensitive detector, M2,M3,M4: mirrors, VUV-1: high-flux secondary monochromator, VUV-2: high-resolution secondary monochromator, BM 50/2: secondary monochromator for the visible and UV region.*

Monochromator	Primary	VUV1	VUV2	BM 50/2
Mounting	McPherson 15°	Pouey 28°	McPherson 15°	Czerny-Turner
Aperture	f:20	f:2.8	f:10	f:5
Focal length (mm)	2000	500	1000	500
Grating size* (mm)	Ø100	130×130	Ø105	80×110
Groove density (1/mm)	1200	1650**	1200	1200/300
Linear dispersion (Å/mm)	4	10	8	16/64
Coating	Al+MgF_2 Pt	Al+MgF_2	Al+MgF_2	Al
Working range (nm)	Al: 65 - 330† Pt: 30 - 330†	50-300	50-300	190-1200
Blaze (nm)	120 (Al) Pt***	250	120	400

Table 2.1: *Technical data of the monochromators at SUPERLUMI. *Horizontal ×vertical or diameter. **Mean value. ***Platinum grating is a laminar type. †For optimal incident flux, it is reasonable to use the Al grating for wavelengths above ∼80 nm and Pt grating below ∼80 nm (see Fig. 2.2).*

2.3.1 Primary monochromator

The primary monochromator has a 2 m focal length in 15° McPherson mounting with a linear dispersion 4 Å/mm, when grating with 1200 grooves per mm is used [WBHS83]. The monochromator has three entrance slits with fixed widths of 30, 100 and 500 μm. The corresponding best resolution achievable is 0.2, 0.5 and 2.3 Å (FWHM), respectively. The exit slit is adjustable between 10 μm and 2 mm. All necessary alignments can be carried out *in situ*, without breaking the ultrahigh vacuum. The lowest resolution of the primary monochromator (3.3 Å) is not determined by the exit slit, but by the size of chopper slits, located near the exit slit and having width of 925 μm. Two different gratings are mounted on a grating holder and can be interchanged *in situ*. The MgF_2 coated aluminium grating covers wavelengths from 65 nm to 330 nm and the platinum grating from 30 nm to 330 nm.

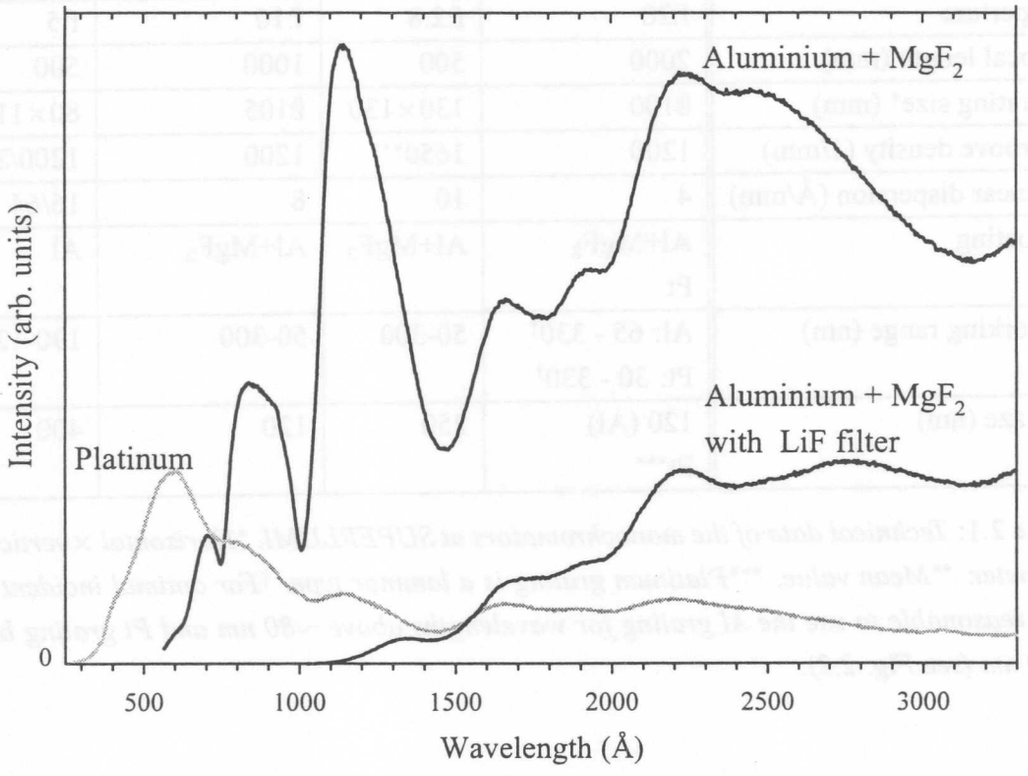

Figure 2.2: *The incident photon flux on the sample for different grating-filter combinations at the SUPERLUMI set-up measured in April, 1999. All curves are presented in the same intensity scale.*

The flux of the exciting photons at various excitation energies is determined by the characteristics of the light source, the grating and the optical elements of the beamline. Sodium salicylate (NaSal) luminescence yield is known to be independent from excitation

energy. Therefore, it is possible to measure the intensity as a function of the excitation energy using the luminescence of sodium salicylate. Typical spectra for the incident photon flux for the aluminium and the platinum grating are shown in Fig. 2.2. As Fig. 2.2 demonstrates, the aluminium grating is well suited for wavelengths longer than ~80 nm and the platinum grating is better for wavelengths shorter than ~80 nm. A LiF and a quarz filter remove higher orders of excitation, inevitable satellites of diffraction gratings. The flux of the aluminium grating with the LiF filter is also shown in Fig. 2.2. The performance of the grating of the primary monochromator degrades under intense synchrotron radiation. VUV radiation causes different photochemical reactions and photolysis of molecules and atoms of the residual gas. Mainly carbon species deposited on the grating surface are responsible for the degradation. Therefore gratings of the primary monochromator are replaced after few years. During a long time period radiation damage occurs in the MgF_2 coating of aluminium grating as well as in all other filters and windows, attenuating light intensity falling onto the sample.

2.3.2 High-flux VUV-1 monochromator

The VUV-1 monochromator is a high transmission instrument (modified Pouey mounting, f:2.8) without entrance slit [GRZP83]. The VUV-1 is located in its own vacuum chamber (Fig.2.1), separated from the sample chamber with an UHV valve. The monochromator has an asymmetric design, the exit arm (652 mm) being longer than the entrance arm (391 mm). The extremely large f-number is due to an especially designed 130×130 mm^2 large toroidal grating (Al with MgF_2 coating) with non-uniform distribution of grooves (mean value n=1650 1/mm). The spectral resolution of the monochromator is mainly limited by the size of the exciting light spot on the sample. With minimized spot size, the best resolution of 5 Å (FWHM) is achievable. The working range of the Pouey monochromator extends from 500 to 3000 Å.

The exit arm of VUV-1 is equipped with two detectors. An open microsphere plate (MSP) is located directly behind the adjustable exit slit and a *solar-blind* photomultiplier is situated in perpendicular direction to the exit arm. This photomultiplier is separated from the VUV-1 monochromator chamber with a LiF window and is illuminated via a removable mirror (Al with MgF_2 coating).

2.3.3 High-resolution VUV-2 monochromator

The VUV-2 monochromator is designed for high-resolution luminescence analysis [Möl86]. It is an 1-meter spectrometer in 15° McPherson mounting manufactured by *Acton*

Research (Fig.2.1). As diffraction element, a holographic MgF_2 coated aluminium grating (diameter 105 mm) with 1200 grooves/mm is used. The VUV-2 entrance slit is illuminated via the toroidal mirror M4, located in the VUV-1 monochromator chamber. The entrance slit is adjustable between 5 μm and 2.5 mm. A multichannel plate type position sensitive detector (PSD) is mounted on the focal plane of the exit arm. An order of magnitude better resolution, compared to the Pouey monochromator, is feasible due to the longer focal length (1000 mm), usage of an entrance slit and smaller grating size. The typical resolution of VUV-2 monochromator was $\sim$1 Å in the first diffraction order. Performing measurements in the second diffraction order of the grating can increase the resolution as well.

2.3.4 Monochromator for the visible and ultraviolet region

The SUPERLUMI set-up is equipped also with a 0.5 m double monochromator, usually operating in single configuration, for the visible and ultraviolet (UV) region. This instrument (BM 50/2) in Czerny-Turner mounting is manufactured by *BM Spectronic* [Bec97]. This monochromator has two different gratings with 1200 and 300 grooves per mm. The typical resolution of BM 50/2 monochromator was $\sim$30 Å. The BM 50/2 is located outside the vacuum-system and therefore the air absorption determines the short-wavelength edge of the working range. During experiments with the BM 50/2 monochromator, the VUV-1 monochromator grating is used in the zeroth order as a mirror. With an additional removable mirror, the light reflected from the grating is directed through the sapphire window into the BM 50/2 monochromator (Fig. 2.1). An UV-visible sensitive PSD or conventional photomultipliers are used as detectors. In present work, the BM 50/2 monochromator was only used for the measurements of the incident flux.

2.4 Detectors and electronics at SUPERLUMI

All photon detectors at the SUPERLUMI set-up use the principle of single-photon counting and afford an amplification factor up to 10^8. For the VUV range, an open microsphere plate detector (MSP) and an open position sensitive detector (PSD) are used. Both detectors are mounted in the UHV system of the respective monochromators. Experiments with open detectors require a vacuum of at least $\sim 10^{-6}$ Torr in the sample chamber. Otherwise gas discharges could destroy the detector, since the vacuum inside the detector is much worse than in sample chamber. There are also different photomultipliers and a PSD for UV and visible region, all separated from the common UHV system with windows.

2.4.1 Microsphere plate detector

Most of the experiments presented in this thesis were carried out with the MSP detector attached to the high-flux VUV-1 monochromator. The MSP is a plate consisting of glass spheres (diameter ranging from 20 to 100 μm). The surface of the spheres is coated with high-resistance, but still conductive material which is also a good electron emitter. Both sides of the MSP are coated with a conductive electrode for applying high voltage. If a photon impacts into the cathode under negative high voltage, an electron is emitted. The electrical field accelerates electrons and they move through irregular channels between spheres in the direction of the anode. If an electron collides with a sphere, secondary electrons are emitted and so the signal is amplified. The working principle of the MSP and a microchannel plate is very similar, but there is one substantial difference. In channelplates, an *ion feedback* exists: the electrical field accelerates ionized residual gas molecules in the direction of the cathode, hitting the cathode and producing new electrons. In such a way, every 'real' incident pulse is accompanied by a series of after-pulses. Due to the irregular channels, the acceleration of residual gas ions is strongly suppressed in a MSP.

Producer		*El Mul*
Type		E033DTA1F
Working range	(nm)	$\leq$180
Diameter	(mm)	32.8
Cathode effective diameter	(mm)	27.0
Thickness	(mm)	1.41
Cathode coating		CsI (1 μm)
Amplifier gain		$5 \cdot 10^6$
Time resolution (FWHM, ~3.2 kV)*	(ps)	320
Integral dark pulse rate	(cps)	5...10
Max. operating pressure	(Torr)	10^{-5}...10^{-4}
Operating voltage	(kV)	-3.0...-3.5

Table 2.2: *Technical data of the mircosphere plate (MSP). *The apparatus function obtained from the measurement of synchrotron radiation pulse (see section 4.5.1).*

A high voltage up to 3.5 kV can be applied to the MSP used in the SUPERLUMI set-up, but the maximum value would cause a decrease of the lifetime of the detector. Time-resolution decreases as well at higher voltages. Most of the experiments were performed with a high voltage value of 3.2 kV. The cathode of the MSP is coated with a 1 μm thick CsI layer to increase the sensitivity of the detector in the long wavelength region $\leq$ 180 nm. The

MSP has a very low dark pulse rate which can be as small as 5...10 cps (counts per second). In the experiments presented in this thesis, the signal to noise ratio of the MSP detector was optimized and the corresponding average dark pulse rate was a few tens cps. The most important characteristics of the MSP detector are summarized in table 2.2. A more detailed description of the MSP is published in the diploma thesis of S. Körding [Kör97].

2.4.2 Position sensitive detector for the high-resolution VUV-2 monochromator

The VUV-2 monochromator has about 10 times better spectral resolution than the VUV-1 and therefore the number of photons detectable is also significantly smaller. This disadvantage can be essentially compensated with using a position sensitive detector for the VUV [Hag89]. The PSD (*Surface Science Laboratories* 3391A) is a modified channelplate detector which consists of 5 channelplates located one on top of the other, and from a modified anode. The quadrangular anode provides 4 different output signals from each corner. The special design of the resistive anode affords free diffusion of the charge carriers and makes possible to calculate the position of the photon incident. This again permits to determine the wavelength of the incident photon. The technical data about the VUV sensitive PSD are collected in table 2.3.

Producer		*SSL*
Type		3391 A
Working range	(nm)	50...180
Cathode		CsI
Amplifier gain		$1.3 \cdot 10^7$
Time resolution (FWHM)	(ns)	1.5
Integral dark pulse rate	(cps)	1...3
Max. quantum yield	(%)	15
at wavelength	(nm)	120
Operating voltage	(kV)	-3.25

Table 2.3: *Technical data of the VUV sensitive position sensitive detector.*

Producer		*Hamamatsu*	*Valvo*	*Valvo*
Type		R2059	XP2020 Q	XP2230 B
Working range	(nm)	160...650	160...600	250...650
Photocathode		bialkali	SbKCs	SbKCs
Window		quartz	quartz	borosilicate
Cathode diameter	(mm)	46	44	44
Amplifier gain		$2{\cdot}10^7$	$3{\cdot}10^7$	$3{\cdot}10^7$
Rise time	(ns)	0.7	0.7	0.7
Dark pulses	(cps)	10...15	~200	50
at temperature	(°C)	-15...-30	-15...-30	-15...-30
Max. quantum efficiency	(%)	30	25	28
at wavelength	(nm)	420	400	400
Typical voltage	(kV)	-2.2	-2.2	-2.2

Table 2.4: *Technical data of conventional photomultipliers at the SUPERLUMI set-up.*

2.4.3 Photomultipliers

Conventional photomultipliers were used in the present investigations for the measurements of incident flux and reflectivity. In both cases, the VUV light was converted into fast broad-band visible emission peaking at ~420 nm using sodium salicylate. Therefore, the spectral characteristics of the photomultipliers are not especially important, because the light intensity was always measured at the same wavelength. In order to decrease the dark pulses, the photomultipliers were cooled with Peltier elements. Additionally, the signal to noise ratio can be improved, if the luminescence is measured within a time window not exceeding the decay time of sodium salicylate. Therefore, the counting of dark pulses from the photomultiplier outside the time-window is prohibited until the arrival of the next excitation pulse. Despite of the relatively strong signals in reflection and incident flux measurements the signal to noise ratio was further improved using the time-window technique. The technical data for various photomultipliers at SUPERLUMI are shown in table 2.4.

Finally, the SUPERLUMI set-up has an additional VUV detector, namely a *solar blind* photomultiplier (*Hamamatsu R6836*) with a working range 115 - 320 nm. The short wavelength edge of sensitivity for the *solar blind* photomultiplier is restricted by the transmission of its MgF_2 window. Also the time-resolution is not so good as that of the MSP and therefore the *solar blind* detector was not used in the present work. The advantage of the *solar blind* photomultiplier is that it can be used in the measurements of RGS at 'higher temperatures'. The strong sublimation from RGS at elevated temperatures prevents the use of open cathode

detectors as the MSP.

2.4.4 Experimental electronics

Several electronic devices are applied for signal processing at the SUPERLUMI set-up. The method of 'time correlated single photon counting' is used for measurements. A single photon causes a signal pulse from the detector and afterwards this pulse is processed separately. A short overview of the electronic devices at the SUPERLUMI set-up is given in this section.

Weak detector signals are amplified by a charge sensitive preamplifier and processed by a discriminator, which provides output pulses according to the widely used NIM (*Nuclear Instruments Method*) standard. In the present study, a fast preamplifier (*Ortec VT120)* together with a constant-fraction discriminator (*Canberra* 2126) or an integrated preamplifier - constant-fraction discriminator (*Ortec* 9327) were used. The constant-fraction principle offers good time-stability since timing of the output signal is independent from the amplitude of the detector signal.

Time-to-amplitude converter (TAC) *Canberra* 2145 or 2146 was used in the time-resolved measurements. The TAC works as a stopwatch covering time-range from ns to ms. The TAC has two inputs: one for the start signal (NIM) and a second one for the stop signal (NIM). The TAC gives an output pulse with an amplitude (voltage between 0 and 10 V) proportional to the time interval between the start and subsequent stop pulse. At the SUPERLUMI set-up, the TAC works in an 'inverse' regime, this means that the detector signal is used as a start pulse and a *raster* signal from the *bunch clock* of DORIS is used as a stop signal. It is important for the measurements with the TAC that not more than one event is counted per excitation pulse. If there are more events, the TAC takes into account only the first event and the short-time part in the spectrum or decay curve is overestimated (*pile-up* effect).

The TAC has also an integrated single-channel analyzer (SCA). The SCA works as a selective gate and gives an output signal only if the input signal voltage is located between an adjustable upper and lower level. In co-operation with the TAC, the SCA affords the possibility to measure spectra in different time-windows. The TAC together with a multichannel analyzer (*Canberra 3501*) is used for the recording of decay curves as well. In the 'pulse height' mode of the multichannel analyzer, the input pulses are sorted by their voltage amplitude (*i.e.* time) to a histogram. This histogram represents the frequency of occurrence for the emitted photons in the selected time interval - *i.e.* the decay curve.

Due to the various loss processes, the current in the storage ring decreases leading to a proportional change of the intensity of synchrotron radiation. Therefore it is necessary

to increase the counting time proportionally for every experimental point. This is realized using a dual counter (*Canberra* 1776). The DORIS control room provides every experiment with a voltage proportional to the storage-ring current. This voltage is converted to pulses by a voltage-to-frequency converter (~50 000 counts per sec at 100 mA). The dual counter integrates such reference pulses and gives a stop signal for any other device after a preselected number of reference pulses.

The position sensitive detector for the VUV is provided with four charge-sensitive amplifiers for signals from each corner of the anode. A position-computer (*Surface Science Laboratories* 2401A) processes such input signals and generates several output signals. Three of them are used as described below:

x-position: a signal with duration 2.5 μs and amplitude between 0.5 and 4.5 V, gives the x-coordinate of the incident photon

y-position: similar signal parameters, but for the y-coordinate

strobe: position computer output rate - the rate of the detector signal within the detector region determined by edge-gate discriminators (TTL, 2 μs)

The PSD is mounted to the monochromator in such a way, that the y-direction of the detector is parallel to the dispersion plane of the monochromator. Therefore, the y-position carries information about the wavelength of the incident photons.

2.5 Experimental Method

2.5.1 Single-photon counting

A detected photon causes a weak current pulse in the detector. For example, it can be measured with a very sensitive electrometer. If the following electronics is sensitive 'enough', the signals caused by single photons can be separated and processed afterwards digitally. This is indispensable for time-resolved spectroscopy. The general advantage of single photon counting is the possibility to improve the signal to noise ratio significantly. A discriminator processes every signal pulse separately and ignores pulses which do not have sufficient height and shape being characteristic for the detector. In the ideal case, dark pulses of the detector are the only source of noise, because they are not distinguishable from pulses caused by photons. The maximum permitted count-rate depends on the repetition rate of the excitation pulses, on the processing dead-time of the electronics and also on the properties of the signal pulses from the detector. The counting rate should be significantly smaller than the repetition rate of the excitation pulses ($5.2 \cdot 10^6$ Hz for DORIS in the *multi bunch mode*). If more than one signal pulse occurs per excitation pulse, then a short-time part in spectrum or

decay curve is overestimated (*pile-up* effect). A saturation effect shows up if the electronics cannot separate two sequential signal pulses any more, causing nonlinearity. Most of the experiments in present work were carried out with a MSP detector. An analysis showed that the nonlinearity for this detector starts at a counting rate of some 10^4 cps [Kör97]. Therefore, always smaller counting rates were used.

2.5.2 Data registration

High-resolution emission spectra

An emission spectrum displays the luminescence intensity as a function of emitted photon energy for fixed photon energy of excitation. The high-resolution VUV monochromator (VUV-2) equipped with the PSD was used for the measurements of time-integrated high-resolution luminescence spectra of the free and self-trapped excitons, essential for estimating the 'quality' of the sample. Using the PSD, luminescence emission spectra can be measured at selected positions (central wavelength) of the secondary monochromator. The covered wavelength range is determined by the size of the PSD, extending $\pm$ 10 nm from the central wavelength. Fig. 2.3 shows a principal scheme for high-resolution luminescence measurements. The four signals of the quadrangular anode are amplified and fed into the position computer in which the x- and y-coordinate are calculated for each event. From the position computer, the MCA uses the y-signal as input signal and sorts all pulses forming a histogram as a function of the y-coordinate. After transforming the y-coordinate to the wavelength scale, this intensity distribution presents the time-integrated luminescence spectrum. By selecting the preset of the dual counter, the spectra are normalized to the same number of excitation photons already during measurements.

Time-resolved emission and excitation spectra

Most of the luminescence and excitation spectra in present work, time-integrated as well as time-resolved, were measured with the high-flux monochromator VUV-1 in combination with the MSP detector. Fig. 2.4 depicts the schematic diagram of the electronics for such measurements. No principal difference exists for luminescence emission and excitation measurements. Only, the monochromator to be scanned is different. The photon energy of excitation is selected for luminescence measurements and the luminescence intensity is measured as a function of the emitted photon energy. On the contrary, the photon energy of luminescence is fixed for the excitation spectra. The intensity of the respective luminescence is measured as a function of photon energy of excitation. Detailed information about the electronic devices shown in Fig. 2.4 was given in the section 2.4.4.

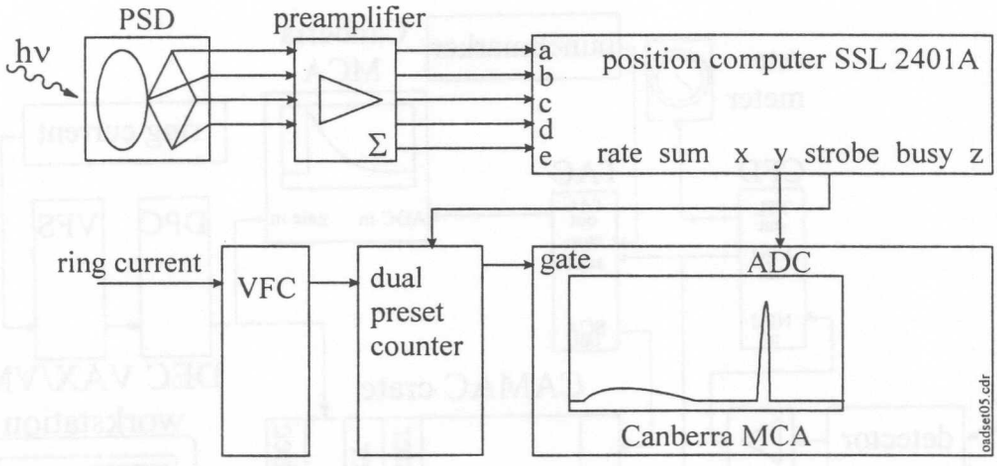

Figure 2.3: *Principal scheme for the high-resolution luminescence measurements with the PSD and the VUV-2 monochromator. PSD: position sensitive detector, MCA: multi-channel analyzer, ADC: input of the MCA with analog-to-digital converter, VFC: voltage-to-frequency converter.*

The control of the experiment is achieved with a *Digital DEC 30000/300* workstation and using the *Mess95* program [Bec97]. This program permits to control scanning parameters and to watch spectra graphically in real-time. The SUPERLUMI set-up is CAMAC-based [Bec97]. It means that the computer does not communicate with periphery devices directly, but via the CAMAC ('computer automated measurements and control') interface. Each measurement starts with a computer control of the wavelength of the respective monochromator according to the settings given by user. Subsequently, the CAMAC-based counters are started, collecting data until the dual counter gives a stop signal. The counterboard has 6 counters which can be used simultaneously. For time-integrated measurements, the amplified and discriminated detector signal pulses from the CFD are counted. Time-resolved measurements are performed by means of TAC's. Each TAC provides one time-window. The SCA of the TAC gives an output signal for the counter only for those pulses which arrive within the length of selected time-window. The moment of the excitation pulse is determined by the *raster* signal of the *bunch clock*, delivered from the DORIS control room.

Decay curves

For the measurements of the decay curves, it is essential to connect the TAC output to the ADC input of the MCA. The MCA operating in the 'pulse height' mode sorts every pulse to the respective time-interval. As a result, a histogram of the number of pulses per channel versus time is formed, *i.e.* the decay curve (Fig. 2.4). The TAC allows for time-resolved

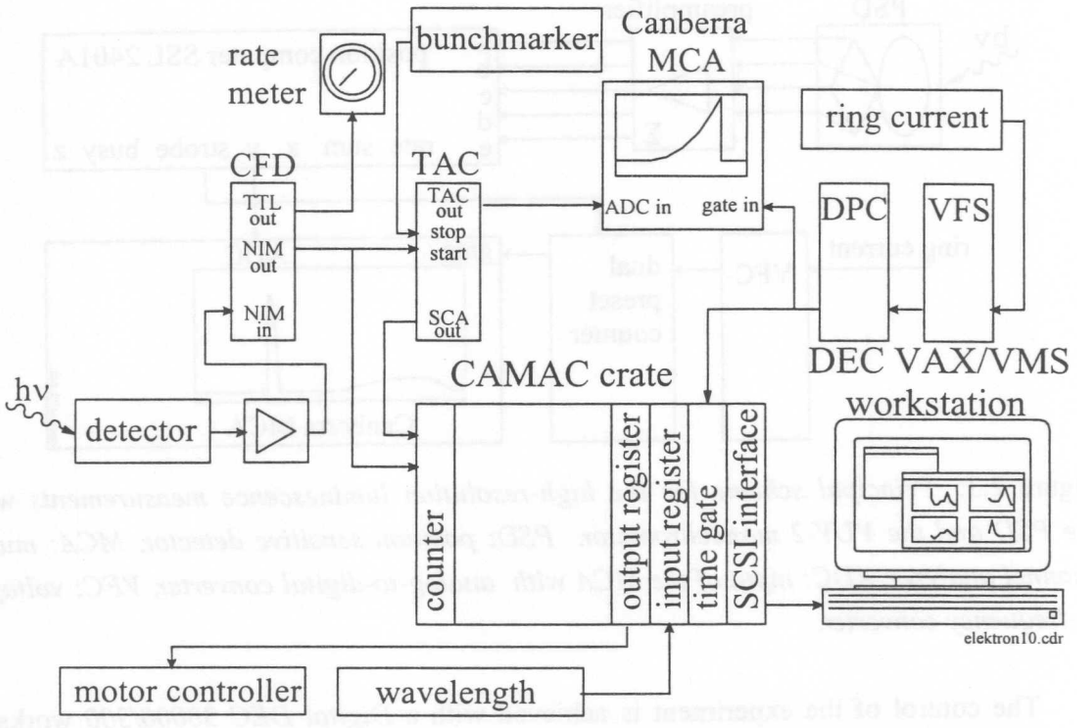

Figure 2.4: *Principal scheme for time-resolved luminescence and excitation measurements. Secondary monochromator is scanned for luminescence measurements and primary monochromator for excitation measurements. TAC: time-to-amplitude converter, CFD: constant-fraction discriminator, VFC: voltage-to-frequency converter, DPC: dual preset counter, TTL: transistor-to-transistor logic, NIM: 'nuclear instruments method', CAMAC: 'computer automated measurements and control'*

measurements in different time-ranges from 20 ns to 1 ms. Nevertheless, the maximum decay time range at SUPERLUMI is determined by the time interval between synchrotron bunches. It equals to 964 ns when DORIS is operated in *one bunch mode*. For the longer time-range, SUPERLUMI offers additionally the unique possibility to work with a chopper, running under UHV conditions [Run97].

Reflection spectra

For the reflection measurements, the sample is adjusted in a way that the specular reflection from the sample surface is directed to the sodium salicylate coated window. The sodium salicylate luminescence, excited by the reflected light, is measured instead of the direct VUV reflection. The broad band emission of sodium salicylate (maximum at 420 nm, decay time ~10 ns) is assumed to have a constant quantum yield under UV to VUV

excitation [Sam67]. The intensity of the luminescence is measured with a conventional UV-visible sensitive photomultiplier (see section 2.4.3). Assuming the constant quantum efficiency under VUV excitation and the invariable shape of sodium salicylate emission measured by the detector, the recorded reflection spectra do not depend on the detector sensitivity. Between the sodium salicylate coated window and the photomultiplier, the filter (BG25) is also applied to select emission of sodium salicylate. The axes of the reflection channel and of the exciting beam are geometrically located under the 35°. Scanning of the primary monochromator occurs exactly in same way as measuring the excitation spectra (Fig. 2.4). The excitation and reflection spectra can be recorded simultaneously at the SUPERLUMI set-up.

2.5.3 Data processing

The raw data are affected by different properties of the experimental set-up, as:

- spectral-resolution
- time-resolution
- spectral sensitivity of the registration systems
- spectral distribution of the exciting light
- time-dependence of the intensity of the exciting light
- dark pulse rate of detectors

Due to the energy dependence of the excitation intensity (caused by the light source and the transmission of the beamline and the primary monochromator) it is necessary to correct the excitation and reflection spectra to the incident photon flux. All reflection and excitation spectra presented in this work are normalized. The flux spectrum incident on the sample depends strongly on the optimization of the mirrors of the beamline. Therefore, at the beginning of each beamtime period the incident flux spectrum was measured, and the positions of the first mirrors were kept constant during experiments.

Monochromators operate usually in wavelength units. An equality $E = hc/\lambda$ is used for transforming wavelength (λ) to the energy scale (E). Therefore, all luminescence spectra plotted in energy scale are deformed because $\Delta\lambda = -(hc/E^2)\Delta E$ is not linear in energy. Luminescence spectra are influenced also by the transmission function of the secondary monochromator and detector sensitivity. In this work, the emission spectra are not corrected for two reasons, (i) they do not cover a large range of photon energy, and (ii) no quantitative conclusions are drawn for the relative intensities.

2.6 Gas-handling system and sample preparation

Rare gas atoms interact each other via very weak van der Waals forces. Therefore, RG are in the gaseous state at room temperature and normal pressure. In order to obtain the liquid or solid state, it is necessary to apply high pressure or low temperature as shown by the phase diagram in Fig. 2.7. Preparing samples for VUV spectroscopy, the only possibility is to use low temperature, because no optically transparent materials for a pressure cell exist in this spectral range.

The preparation of RGS samples depends on many parameters. Not all of them are perfectly reproducible and so every sample is in certain sense 'unique'. Therefore, it is very important to control the reproducibility of the experimental results in different samples. On the other side, it is also significant to measure as much as possible experimental data for the each particular sample. That is essential for data analysis. A comparison of decay curves and excitation spectra, measured at same sample, gives more adequate information as comparing the analogous spectra measured at different samples.

The most important factors affecting the quality of RGS samples are the following:

- purity of the gas
- cleanliness (residual gas pressure) of the gas-handling system and sample chamber
- sample temperature and temperature fluctuations during preparation
- gas pressure and pressure fluctuations in the preparation chamber during sample growth
- sample growing rate
- rate of the sample cooling to the measurement temperature
- temperature fluctuations during measurements
- radiation defects of the sample caused by the exciting light

The purity specification and typical contaminants of gases used in the experiments at the SUPERLUMI set-up are shown in table 2.5.

Gas	Xe	Kr	Ar	Ne
Supplier	*Spectra Gases*	*Spectra Gases*	*Spectra Gases*	Unknown*
Purity specification	5.0	5.0	5.5	4.8
%	99.9990	99.9990	99.9995	99.998
Typical contaminants (*ppm*)				
Ar	1.0	2.0		
CF_4	0.5	0.5		
CH_4		0.5		0.5
C_nH_m	0.5		0.1	
CO			0.1	0.5
CO_2	1.0	0.5	0.1	0.5
H_2	2.0	0.5	0.5	
H_2O	0.5	0.5	0.2	0.5
He				8.0
Kr	5.0			
N_2	2.0	2.0	2	1.0
O_2	0.5	0.5	0.1	0.5
SF_6				
Xe		5.0		

Table 2.5: *Purity specification and typical concentration of contaminants for gases used in experiments at the SUPERLUMI set-up (status of 1998-1999). *A supplier is unknown, therefore data about typical contaminants are taken from 'Spectra Gases' specification for similar purity grade.*

2.6.1 Gas inlet and sample growing system

The gas inlet system (Fig. 2.5) permits to control the amount of gas during sample preparation and also to mix different gases for growing doped RGS samples. All gas cylinders are located in the gas cabinet for safety reasons. Every cylinder is provided with a pressure reducer and a mechanical manometer. Several UHV valves used in the gas-handling system, permit to mix different gases without polluting gases in different cylinders. A gas mixing chamber is provided with two pressure gauges (*MKS Baratron*) with different sensitivity: a high- (10 Torr range) and a low-sensitivity (1000 Torr range) gauge. The high-sensitivity gauge is used particularly for doping experiments to control the amount of the dopant. The low-sensitivity gauge affords to monitor the sample growing rate and also to control the amount of the matrix gas in the case of doped samples. A turbomolecular pump (*Pfeiffer TMU 260*) is used for evacuating the system. It is mounted on the bottom of gas mixing chamber, being separated from the chamber with a 'big' UHV valve (CF 100). The typical pressure of residual gases in the mixing chamber is below 10^{-9} Torr.

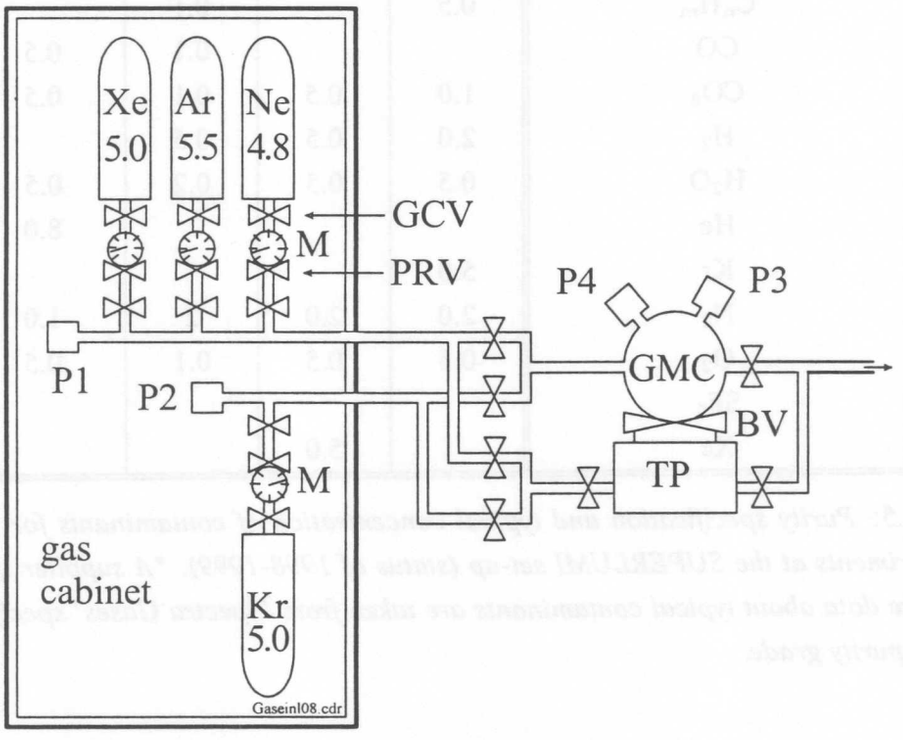

Figure 2.5: *Gas inlet system. P1,P2: UHV pressure gauges, P3,P4: gas pressure gauges (MKS Baratron), TP: turbomolecular pump, BV: 'big' UHV valve, M: mechanical manometer, GMC: gas mixing chamber, PRV: pressure reducing valve, GCV: gas cylinder valve. All other valves, shown in the picture, are high conductivity UHV valves.*

	Time	
	20 min	3 days
Pressure before reconstruction (Torr)	worser as 10^{-2}	10^{-4}
Pressure after reconstruction (Torr)	10^{-6}	10^{-8}

Table 2.6: *Pumping rate of the residual gases in the gas inlet system before and after reconstruction (measured with P1). Time is measured from the start of the turbopump after the complete venting of the gas-system.*

During the present work, a significant reconstruction of the gas inlet system was performed. Due to the small diameter (3 mm) tubes and valves used earlier between the gas mixing chamber and the gas cylinders, the pressure near the gas cylinders was relatively bad (table 2.6). Therefore, the purification of the system occurred only with the help of multiple rinsing with valuable rare gas. Nevertheless, the cleaning of the system was not sufficient and always some additional tens of ppm of impurities (gas which has been used in the previous experiment) was found in the grown samples. For example, if xenon has been used before an experiment with krypton, a remarkable xenon impurity line at 9.7 eV was observed in krypton luminescence spectra. Such a vacuum problem in gas-handling system arose some years ago, when new safety regulation in HASYLAB were introduced. As a result of storing gases in a special cabinet, a pumping efficiency of the gas-handling system was significantly reduced.

By replacing the 3 mm diameter gas tubes and low-conductivity valves with 15 mm diameter bellows and high-conductivity UHV valves, the vacuum conditions in the gas system were considerably improved again. As table 2.6 demonstrates, at the maximal distance from the turbomolecular pump (at the pressure gauge P1), pumping is now faster by **four orders of magnitude** than before. It is especially important for the doping experiments, where during relatively short time different gases are used.

The system for sample growth is shown in Fig. 2.6. In the present work, a He-flow cryostat (*Leybold)* with an integrated heating element (resistance 6.5 Ω) was utilized. For the temperature control, a temperature controller (*Lake Shore Cryotronics*, model 330) and a silicon diode (DT-470, *Lake Shore Cryotronics*) were applied. The temperature control was based on changing of the heating power at a constant flux of helium. The working range of this cryostat is 5 - 400 K. The upper limit of the temperature is determined by the melting point of indium (an indium seal is used between cryostat and sample holder for improving heat conductivity) and the lower limit is due to the liquid helium cooling.

The copper sample holder has an elevation with a conical shape which fits to a movable cylindrical stainless steel preparation chamber with a wedge-shaped edge. The preparation

chamber is connected with the gas inlet system by a thin stainless steel tube. Under UHV conditions, the chamber can be pressed against the sample holder by the aid of a linear manipulator. A variable leak valve (*Granville Philips,* model 203) is used to change gas flux during growing process. The growing rate is calculated on the basis of change of the pressure in the gas mixing chamber. There is also a high sensitive pressure gauge (*MKS Baratron*, 10 Torr range) which affords measurements of the pressure in the preparation chamber. It is important to note, that the pressure measured by the gauge at 30 cm distance is not exactly equal to that in the preparation chamber.

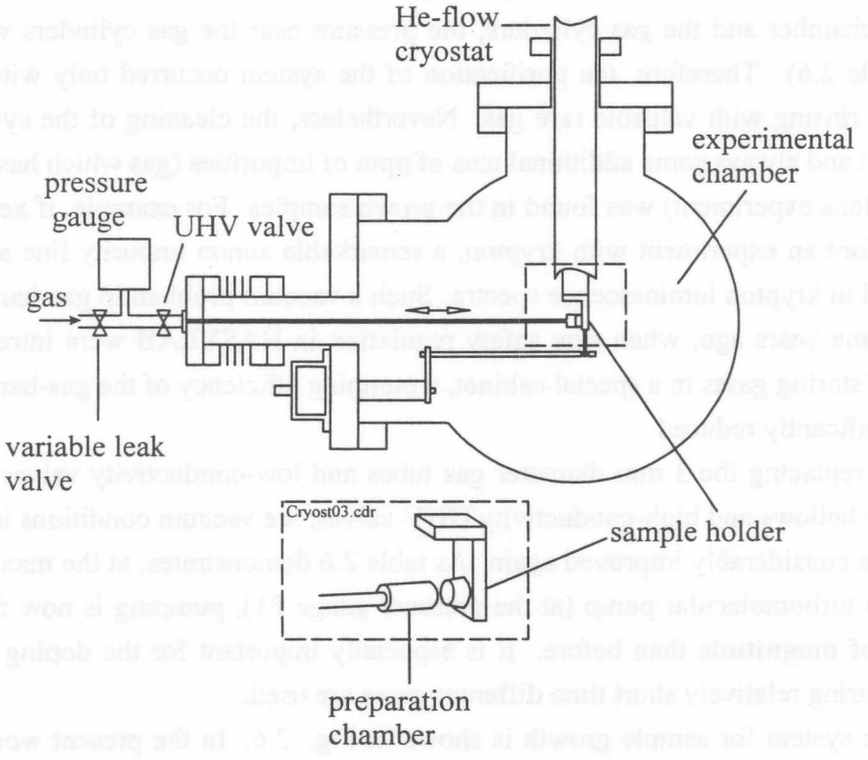

Figure 2.6: *Crystal growth system.*

2.6.2 Sample preparation

Various growth methods of RGS samples exist [KV77]. To illustrate different growing methods, the p-T diagram for Kr is shown in Fig. 2.7 [And89, KV77]. The simplest possibility to prepare RGS sample is to direct the gas onto the cold sample holder. 'Cold' is here a relative notion and is determined with the sublimation temperature at given pressure. The thermodynamic equilibrium conditions are not fulfilled for such kind of sample preparation. The prepared samples have irregular macroscopic structure consisting of tiny crystallites and look like snow in visual observation.

Theory predicts that the best crystals can be grown through the liquid phase in nearly thermodynamic equilibrium conditions. Such kind of growing technique has been developed and used for several years in Tartu for growing large single crystals with volume 1 to 2 cm^{-3} [KKLN87]. The upper arrow in Fig. 2.7 characterizes such kind of growing method.

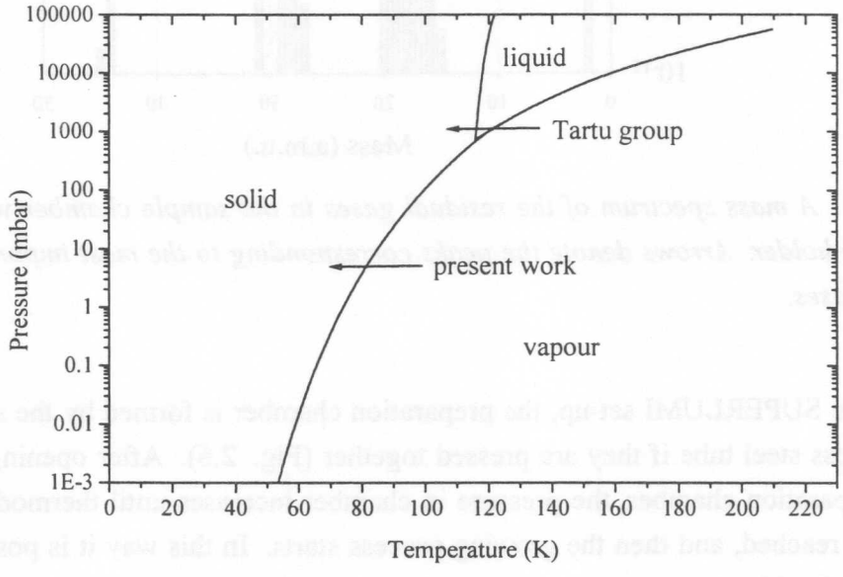

Figure 2.7: *p - T diagram for the krypton on the basis of data from [KV77, And89]. Two different preparation methods are sketched with arrows.*

In the present work, the growth from vapour was used, giving good quality polycrystalline samples (the lower arrow in Fig. 2.7). The basic principles of the crystal growth predict good samples if the phase transition from gas to solid takes place at nearly thermodynamic equilibrium conditions at relatively 'high' temperature (as near to the triplet point as possible). To fulfil the required conditions, it is essential to use a preparation chamber in order to maintain a relatively 'high' pressure.

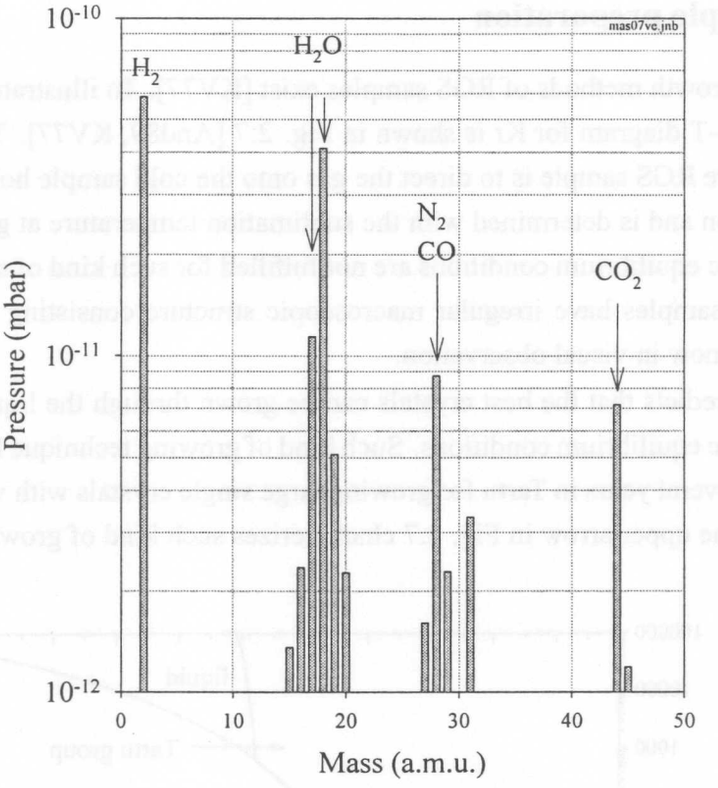

Figure 2.8: *A mass spectrum of the residual gases in the sample chamber with cooled (7 K) sample holder. Arrows denote the peaks corresponding to the most important traces of residual gases.*

At the SUPERLUMI set-up, the preparation chamber is formed by the sample holder and stainless steel tube if they are pressed together (Fig. 2.6). After opening the gas flux to the preparation chamber, the pressure in chamber increases until thermodynamic equilibrium is reached, and then the growing process starts. In this way it is possible to grow samples at 'high' substrate temperatures under nearly thermal equilibrium conditions. Without any additional gasket, a vapour pressure up to 10 Torr is achievable inside the preparation chamber. Such a pressure in the preparation chamber causes a rise of background pressure in the experimental chamber up to 10^{-5} Torr. The growing rate of the sample is controlled with the variable leak valve. If the desired thickness of the sample is obtained, the gas inlet is closed, and the sample will be cooled down. The cooling rate has to be small (in the present work $\sim$1 K/min or slower). Very quick cooling down can damage the sample due to the internal stress. In order to open the preparation chamber, temperature below 40 K is needed for Kr samples. At higher temperature, the sample sublimates due to the very small background pressure in the sample chamber. During further cooling down, some cracks ap-

		Krypton sample 13	Krypton sample 24
Preparation temperature	*K*	84.0	84.3
Preparation pressure	*Torr*	6.2	7.3
Growing rate (used gas amount)	*Torr·l/h*	5.6	4.7
Growing rate	μm/min	2.7	1.9
Preparation time	*h*	2.5	2.7
Average cooling down rate	*K/min*	1.0	1.0
Sample thickness	*mm*	0.4	0.3
Peak maximum intensity ratio FE/STE*		1.5	0.54
Integral intensity ratio FE/STE*		0.041	0.016

Table 2.7: *The preparation parameters and luminescence properties of two different samples. *Measured with spectral resolution 1.1 Å.*

pear in the sample around 20 K due to the different expansion coefficients of solid Kr and the copper sample holder.

Immediately after the opening of preparation chamber, residual gas layers start to condense on the surface of RGS sample. Fig. 2.8 demonstrates a typical mass spectrum of the residual gases in the sample chamber in the case of a cooled (7 K) sample holder. Due to the very good vacuum conditions at the SUPERLUMI set-up the contamination of the surface is much slower compared to most of earlier studies of RGS.

Some preparation parameters used for growing two typical samples are shown in table 2.7. In the present work, in most cases, a pressure of $p \approx 8$ Torr and a temperature $T \approx 84$ K were used for preparation. These values are not exactly coinciding with those of the phase diagram, because the pressure is not measured directly in the preparation chamber (see section 2.6.1). The average growing rate (in terms of used gas amount) was normally about 5 *Torr·l/h*. The used amount of gas is found from the decrease of the gas pressure in the known volume: gas mixing chamber (1.0 l) together with the bellow between gas mixing chamber and preparation chamber (0.7 l). Since the sample diameter is specified by sample-holder diameter (9 mm), the sample thickness was estimated from these data.

The intensity of free exciton (FE) luminescence line depends very strongly on the sample quality. Therefore, the FE and self-trapped exciton (STE) luminescence intensity ratio is used as measure of the sample quality. The integral FE/STE ratios and FE/STE peak maxima intensity ratios are also given in table 2.7.

Chapter 3

Theoretical overview

From several points of view, rare gas solids (RGS) are the simplest solids that exist in nature. The peculiar properties of RGS are a consequence of the closed shell electronic configuration of the atoms (He:$1s^2$; Ne to Rn ns^2np^6, n=2,...,6). The binding energies of the valence electrons are so large that the closed-shell nature of the atoms is conserved in the condensed phase, in which the atoms are held together by weak Van der Waals forces. As a result of the high ionization energy of atoms, RGS are dielectrics with extremely large band gap. Due to the special properties of helium (strong quantum mechanical effects) and radon (instability), in the present work the term *rare gas* (RG) is used only for neon, argon, krypton and xenon.

First of all, in this chapter a short overview about the properties of RGS (band structure, Van der Waals interaction) is given. Then, different excitonic effects are discussed, like free excitons (FE), self trapped excitons (STE), exciton polaritons, *etc.* Several models for creation of excitons will be also discussed: FE creation through electron-hole recombination, FE creation via electron-electron scattering and creation of electronic polaron complex. A detailed model for the dynamics of electron-hole recombination into the FE state is presented as well.

Surveys about excitonic properties of RGS can be found in several review papers by Zimmerer [Zim87] and Fugol [Fug78, Fug88]. A large amount of theoretical and experimental results (published in the field of the RGS until 1975) are collected in the books edited by Klein and Venables [KV76, KV77]. More recent information about electronic excitations in RGS is published by Schwentner *et al.* [SKJ85]. Profound information about classical exciton theory is presented in the books by Dexter and Knox [Kno63, DK65].

3.1 Some historical remarks

The discovery of the rare gases occurred about a century ago [KV76]. The reasons why rare gases have not been found earlier, were due to the chemical inertness and a small concentration in the atmosphere (1.28 wt. % argon, other gases in smaller amount). As a result of the spectroscopic investigations in 1868, the astronomer Lockyer discovered a new extraterrestial element helium (from Greek *helios* - 'sun') which showed up as a number of bright lines in the spectrum of the solar chromosphere. In spite of this discovery, it took additional 27 years, until W. Ramsay understood the real nature of helium. The discovery of argon ('the idle one') is linked with the names of Lord Rayleigh and Sir William Ramsay. Lord Rayleigh tried to prepare highly pure nitrogen and noticed that nitrogen prepared from ammonia, and expected to be pure, is slightly lighter than atmospheric nitrogen. In collaboration with Sir Ramsay, they found out that the reason was a heavy gas in atmospheric nitrogen. From the ratio of the specific heats, C_p/C_v, they also concluded that argon must be monoatomic. This together with the zero valence caused new problems, how to find proper place for argon in the periodic table. Either there existed a whole family of new gases, or Ramsay had a real problem in his hands. In 1895, Ramsay separated terrestrial helium. Helium fitted into the periodic table of elements without any problems. The new column VIII was created and there were more rare gases to be found. Krypton ('the hidden one') was discovered in May 1898 , neon ('the new one') in June and xenon ('the strange one') in July. The last rare gas, radon, was found by Ernest Rutherford in 1900 and together with Ramsay he proved that it was a member of the rare gas family (1907). Radon does not have a stable isotope and it decays with half-life of 3.8 days. In 1904, Lord Rayleigh received the Nobel Prize in physics for his contribution to the discovery of argon. In the same year, Sir William Ramsay won the Nobel Prize in chemistry for his work in the discovery of argon and the other noble gases and for his hypothesis that inert gases constitute a new family of elements in the periodic table, fully confirmed by his studies.

3.2 Rare gas solids

3.2.1 Van der Waals interaction

Rare gas atoms are electrically neutral, but they induce dipole moments in each other, and the induced dipole moments cause an attractive interaction between the atoms. Such kind of interaction is called the Van der Waals interaction. At large internuclear distances, the Van der Waals attraction of two rare gas atoms behaves like $P_{att}(r) = -A/r^6$ (dipole-dipole interaction, $A > 0$). Higher order interactions as quadrupole-dipole ($\propto 1/r^8$),

quadrupole-quadrupole ($\propto 1/r^{10}$) *etc.* can be ignored in first approximation [Fug78]. As soon as the electronic clouds of adjacent atoms penetrate into each other, strong repulsive forces show up, the reasons for which are given by the Pauli exclusion principle. The repulsive part of the potential energy can be well approximated by $P_{rep}(r) = B/r^n$ where $10 \leq n \leq 14$ and $B > 0$. One of the most widely used potentials is the Lennard-Jones [12-6] potential, which has the form

$$P(r) = 4\varepsilon \left[\left(\frac{\sigma}{r}\right)^{12} - \left(\frac{\sigma}{r}\right)^{6} \right], \tag{3.1}$$

where ε is the depth of the potential well, r is the internuclear distance and σ is the distance between the atoms in the case of $P(r) = 0$, being equal to the atomic core diameter.

3.2.2 Excimer molecules

Luminescence spectra of the self-trapped excitons in RGS and rare gas molecules in gaseous phase have several common properties [Zim87]. Therefore, a short overview about luminescence of the rare gas molecules is presented. In the ground state, RG atoms interact with each other only via weak Van der Waals forces, as was described in the previous section. The situation changes drastically, if we regard a pair of atoms, where one atom is in an excited (R*) or ionized (R^+) state. Interaction of such an atom (or ion) with the atom in the ground state leads to the formation of an excimer (*i.e.* excited dimer) molecule (R_2^*) or molecular ion (R_2^+) [Mul70]. The excimer molecule is a simple analogue of the trapped molecular-type exciton in RGS (see section 3.4) and the molecular ion is that of the trapped hole center in RGS.

In the context of present work, the lowest excited states $^1\Sigma_u^+$ (O_u^+) and $^3\Sigma_u^+$ (1_u,O_u^-) of the excimer molecule are most important. The potential curves for these states and for the ground state $^1\Sigma_g^+$ (O_g^+) are shown in Fig. 3.1 [KMC97, BWS87]. O_u^+ is short lived (radiative lifetime at zero pressure: $\tau_{O_u^+}$=4.7 ns [KMC97] or $\tau_{O_u^+}$=3.4 ns [MRG$^+$89]) and 1_u long lived (radiative lifetime at zero pressure τ_{1_u}=172 ns) state [KMC97]. The third O_u^- state is situated about 1.5 meV below the 1_u state and has strongly metastable character. The 1_u and O_u^- states are easily mixed in the gas-cell experiments. As a result they emit like a common state $1_u/O_u^-$ with the lifetime τ_{1_u/O_u^-}=264 ns, being in good agreement with gas phase measurements [KMC97, MRG$^+$89].

The molecular emission spectra of the rare gas excimers are characterized by three types of continua in the VUV spectral region. The most important one for the present work is *the second emission continuum* of the rare gases with its maximum at 9.9, 8.4 and 7.1 eV for Ar, Kr and Xe [GKLS92], respectively. The second continuum is well known and

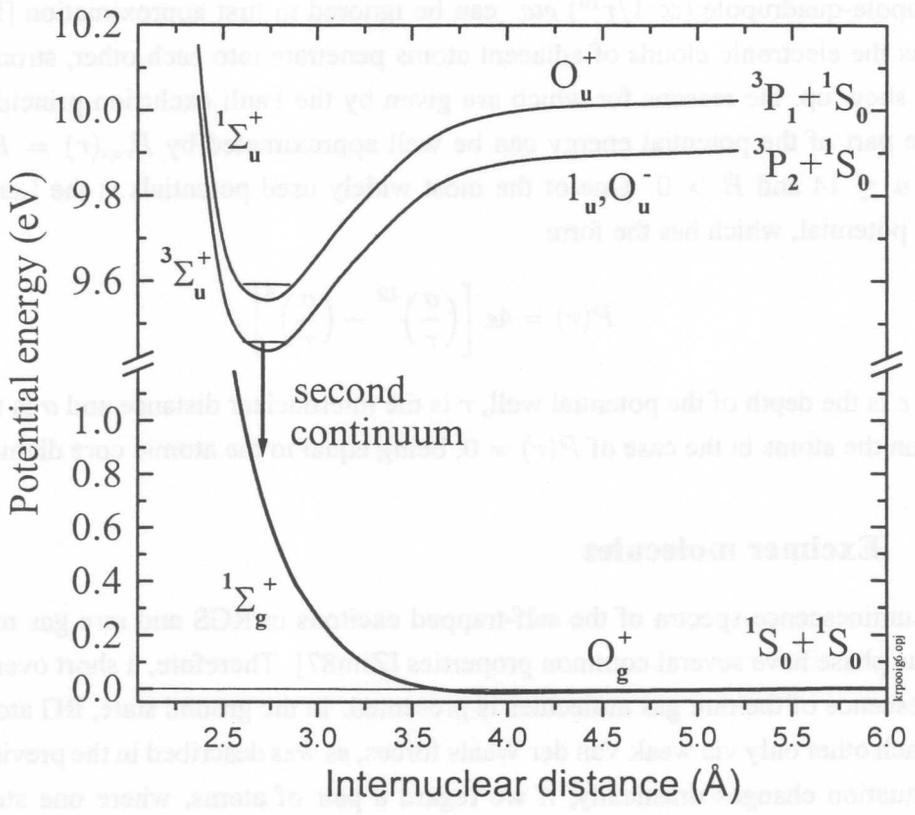

Figure 3.1: *Some relevant potential curves for Kr_2^* eximer (on the basis of [KMC97] and [BWS87]).*

can be unambiguously assigned to the transitions from vibrationally relaxed 1_u and O_u^+ excimer states to the repulsive ground state O_g^+. The exact position and shape of the second continuum depend to some extent on the experimental conditions. The second continuum is the analogue of the molecular type STE luminescence in RGS. At low gas pressures (~100 mbar) another well-known feature, the so called *first continuum*, appears in the emission spectra of pure gases on the long wavelength side of the $^3P_1 \longrightarrow {}^1S_0$ atomic resonance line. The *first continuum* is attributed to the transitions from vibrationally unrelaxed excimers to the ground state at internuclear distances near the shallow van der Waals minima in the ground state [KDS95]. Such an emission from the vibrationally unrelaxed states is a simple analogue of the 'hot luminescence' in RGS.

The atomic lines $^3P_1 \longrightarrow {}^1S_0$ and $^3P_2 \longrightarrow {}^1S_0$ have energetic locations of 10.033 eV and 9.915 eV in Kr, respectively [Moo58]. Opposite to the energetic separation of atomic lines (118 meV), the difference between the two lowest potential curve is not precisely known. In the literature several experimental values are quoted: Morikawa *et al.* 60 meV, Dössel *et al.* 110 meV, Audoard *et al.* 98 meV [AS91, and references therein].

3.2.3 Properties of rare gas solids

Rare gases condense only at low temperatures or at high pressure (phase diagram for Kr is shown in Fig. 2.7 p. 27). They form a *face centered cubic* (fcc) crystal lattice, only helium crystallizes in a *hexagonal closed-packed* structure (hcp) under high pressure. Since the hcp structure is only slightly energetically less favorable than the fcc structure, under some preparation conditions (for example near crystal defects) the hcp phase can coexist with the fcc structure in other RGS as well [Fug78]. Each atom in the fcc lattice is surrounded by 12 nearest neighbours. As the Wigner Seitz cell of the rare gas crystals contains a single atom, their phonon spectra consist of three acoustic branches only, namely one longitudinal and two transverse.

The cohesive energy of a solid is the energy required to disassemble it into its constituent parts - *i.e.*, its binding energy. If we neglect the kinetic energy of the inert gas atoms and take into account only interaction between pairs of atoms (*i.e.* namely, the pair approximation), the cohesive energy of an inert gas crystal is given as a sum over the Lennard-Jones potentials (Eq. 3.1) of all pairs of atoms in the crystal. If there are N atoms in the crystal, the total potential energy is

$$U_{total}(R) = \frac{1}{2}N(4\varepsilon)\left[\sum_{j,i\neq j}\left(\frac{\sigma}{p_{ij}R}\right)^{12} - \sum_{j,i\neq j}\left(\frac{\sigma}{p_{ij}R}\right)^{6}\right], \tag{3.2}$$

where $p_{ij}R$ is the distance between the reference atom i and any other atom j, expressed in terms of the nearest neighbor distance R. The factor 1/2 is needed, because each pair of atoms is counted twice. For the fcc structure, the cohesive energy is

$$U_{total}(R) = 2N\varepsilon\left[12.13\left(\frac{\sigma}{R}\right)^{12} - 14.45\left(\frac{\sigma}{R}\right)^{6}\right]. \tag{3.3}$$

Quantum-mechanical corrections reduce the binding energy by 28, 10, 6 and 4 per cent for Ne, Ar, Kr and Xe respectively [Kit86]. Simultaneously, multi-particle interactions increase energy again about 6 % in the case of Xe [Fug78].

Assuming U_{total} as the total energy of the crystal, the equilibrium value of the nearest neighbour distance R_0 is obtained from

$$\frac{dU_{total}}{dR} = 0 \quad \text{which gives} \quad \frac{R_0}{\sigma} = 1.09. \tag{3.4}$$

This theoretical ratio is the same for all elements with the fcc structure and it is in good accordance with experimental results.

Some important physical properties of krypton atoms and solid krypton are given in table 3.1.

		Value	Reference
Atomic number		84	
Molecular weight	(amu)	83.8	
Electronic configuration		$4s^2 4p^6$	
Triple point temperature	(K)	115.76	[KV76]
Triple point pressure	(mbar)	729.94	[KV76]
Sublimation temperature at 10^{-5} Torr	(K)	45.5	[KV76]
Density at 5 K	(g/cm^3)	3.0926	[KV77]
Lattice constant a at 5 K	(Å)	5.646	[KV77]
Nearest-neighbour distance, f.c.c.	(Å)	3.98	[Fug78]
Binding energy per atom	(meV)	123.2	[Fug78]
Debye energy	(meV)	6.2	[Fug78]
Debye temperature Θ_D	(K)	71.7	[Fug78]
Lennard-Jones parameters			
Depth of the potential well ε	(meV)	14.2	[Fug78]
Atomic core diameter σ	(Å)	3.6	[Fug78]
Maximal phonon energy			
Transverse	(meV)	4.3	[KV77]
Longitudinal	(meV)	6.2	[KV77]
Velocity of sound at 10 K			
Transverse v_t	(m/s)	765	[BTB72]
Longitudinal v_l	(m/s)	1369	[BTB72]
Ionization energy of the atoms I_a	(eV)	13.996	[Moo49]
Band gap energy at the Γ point E_g	(eV)	11.61, 11.59	[Sai80], this work
Total width of the valence band	(eV)	2.3	[SHS+75]
Spin-orbit splitting Δ	(eV)	0.69, 0.70	[Sai80], this work
Low frequency dielectric constant ε_r		1.88	[Fug78]

Table 3.1: *Some physical properties of krypton atoms and solid krypton.*

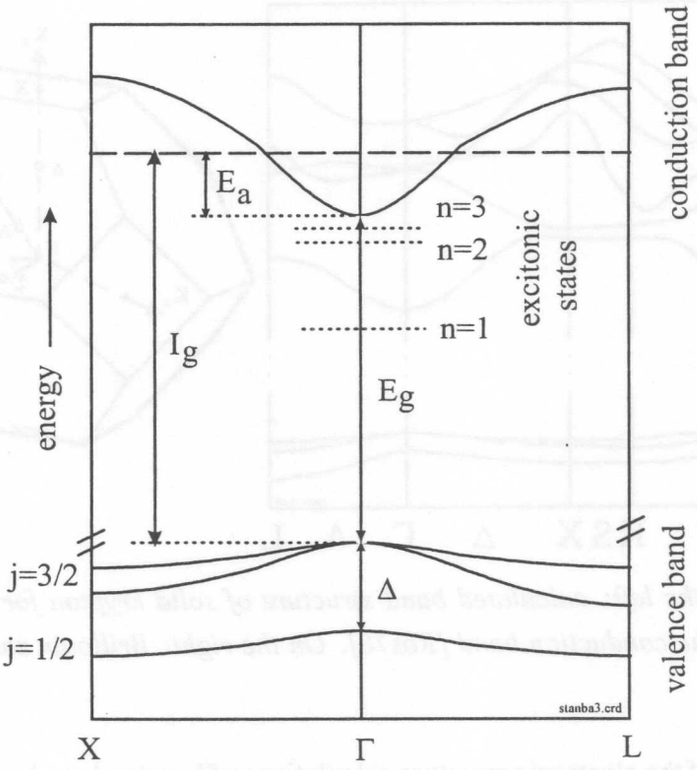

Figure 3.2: *Schematic band structure of solid krypton (E_g-band gap energy, Δ- spin-orbit splitting, E_a- electron affinity, I_g-ionization energy).*

3.2.4 Band structure

Fig. 3.2 shows a schematic band structure for solid krypton [KV76]. Several properties of the band structure are induced by the closed shell electronic configuration of the krypton atoms. So, the band gap between upper valence band and conduction band is extremely large. The valence band is splitted into two sub-bands due to the spin-orbit interaction of the p-symmetric hole. Both sub-bands have their maxima in the centre of the Brillouin zone (at the Γ point). The bands are ascribed to the total angular momentum of holes $j = \frac{3}{2}$ (upper valence band) and $j = \frac{1}{2}$ (lower valence band). The $j = \frac{3}{2}$ band is split in the crystal field except at the Γ point. In accordance with the narrow valence bands, the effective masses of the holes are relatively large.

The minimum of the conduction band is also situated in the centre of the Brillouin zone. The lowest part of the conduction band corresponds to the atomic $4p^5 5s$ configuration. Therefore, the unoccupied states near its minimum have s-symmetry. Consequently, optical transitions between states near the top of the valence band and the bottom of the conduction band are dipole allowed.

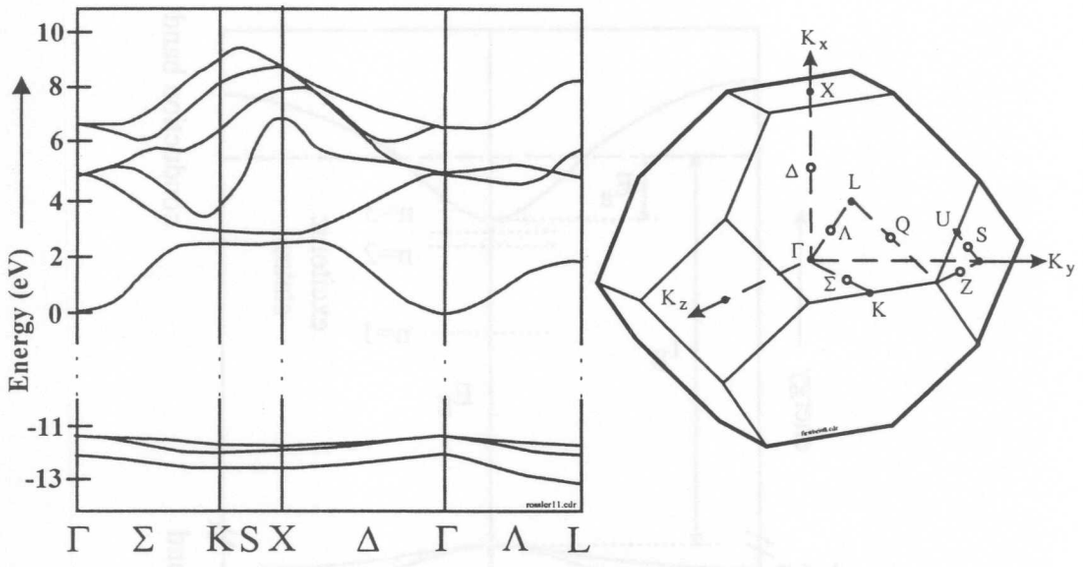

Figure 3.3: *On the left: calculated band structure of solid krypton for valence band and lower states of the conduction band [Rös70]. On the right: Brillouin zone of the fcc structure.*

A number of the electronic structure calculations of krypton have been performed in the past [Rös70, KM73, BPP88]. Fig. 3.3 (on the left) shows the band structure for solid krypton calculated by Rössler [Rös70], and on the right, the Brillouin zone for the fcc structure is depicted.

3.3 Excitons

In several pure dielectrics and semiconductors, reflection and absorption spectra show structures at photon energies just below the energy gap, where the crystal is expected to be transparent. Such structures are caused by the absorption of photons leading to the creation of bound electron-hole pairs. An electron and a hole are bound together by attractive Coulomb interaction. This kind of bound electron-hole pair is called **exciton**. An exciton can move through the crystal and carry energy, but it does not carry any charge, because it is electrically neutral. In Fig. 3.4, the first published VUV absorption measurement of solid krypton is shown [Bal62]. The absorption lines are caused by optical creation of excitons.

Similar to electronic states in a hydrogen atom, exciton states form also series. The energetic positions of such exciton states from the bottom of the conduction band are proportional to $1/n^2$ (n is the main quantum number). The band gap in RGS corresponds to the ionization limit of the hydrogen atom. Such kind of behaviour of excitonic states can be

explained in the framework of the Wannier model (see p. 41). Due to the spin-orbit splitting of the valence band, two exciton series exist, shifted by the Δ (Δ is energy difference of the lower and upper valence band at Γ point). Excitons consisting of an electron bound to the valence hole with $j = \frac{3}{2}$ or $j = \frac{1}{2}$ are often called $\Gamma\left(\frac{3}{2}\right)$ or $\Gamma\left(\frac{1}{2}\right)$ excitons, respectively. A collection of the energetic positions of excitons in solid Kr from various experiments are shown in table 3.2.

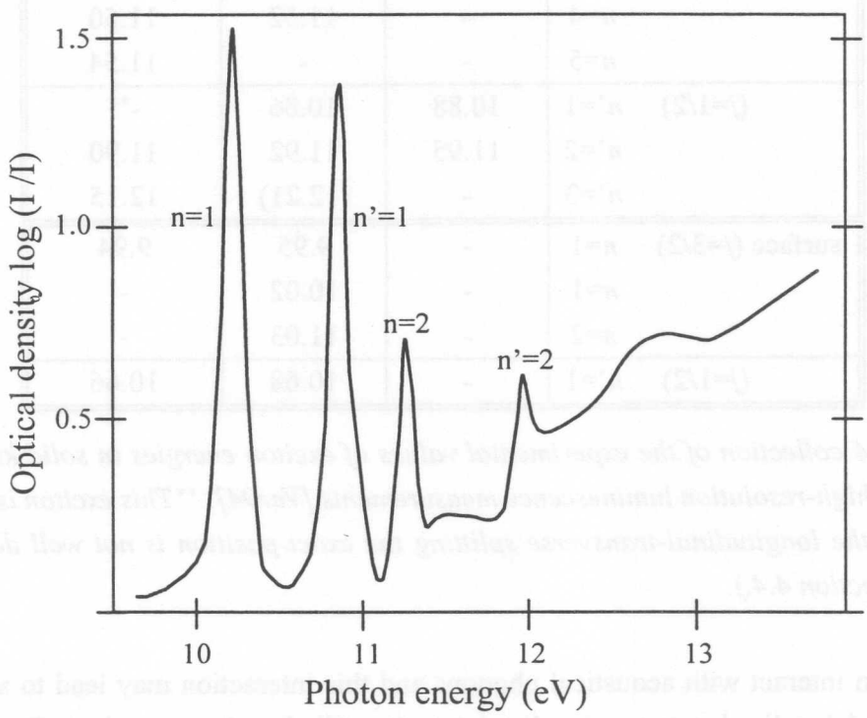

Figure 3.4: *The first published VUV measurement of the absorption of solid krypton (a thin Kr film at 20 K) [Bal62].*

Additionally, the longitudinal-transverse splitting of excitons exists. The energy of an exciton depends on the orientation of its electric-dipole moment $\vec{\mu}$ relative to its momentum $\vec{K}$ vector. In the case of cubic crystals, in the limit $\left|\vec{K}\right| \rightarrow 0$, only two possibilities have to be taken into account: (i) $\vec{\mu} \parallel \vec{K}$, this is called a longitudinal exciton with energy E_L, (ii) $\vec{\mu} \perp \vec{K}$, this is known as a transverse exciton with energy E_T. The energetic difference, E_L-E_T, is proportional to $|\mu|^2$. Observation of longitudinal excitons is usually restricted to electron energy loss spectroscopy. In optical ($\vec{K} \approx 0$) transmission experiments under normal incidence the longitudinal excitons normally do not couple to the incident transverse electromagnetic field. However, in reflection geometry and for rough surfaces optical excitation of longitudinal modes becomes possible [SKJ85].

Since an exciton can freely move through the crystal, it is called free exciton (FE). Free

Experimental method		[Bal62] absorption	[Sai76] absorption	Present work reflection
Temperature		20 K		6 K
volume (j=3/2)	n=1	10.19	10.17	10.14*
	n=2	11.24	11.23	11.23
	n=3	11.48	11.44	11.43
	n=4	-	11.52	11.50
	n=5	-	-	11.54
(j=1/2)	n'=1	10.88	10.86	-**
	n'=2	11.95	11.92	11.90
	n'=3	-	(12.21)	12.15
surface (j=3/2)	n=1	-	9.95	9.94
	n=1	-	10.02	-
	n=2	-	11.03	-
(j=1/2)	n'=1	-	10.68	10.66

Table 3.2: *A collection of the experimental values of exciton energies in solid krypton. *A value from high-resolution luminescence measurements [Var94]. **This exciton is observed, but due to the longitudinal-transverse splitting the exact position is not well defined (see details in section 4.4.).*

excitons can interact with acoustical phonons and this interaction may lead to a transition from a free delocalized state to a localized state (so called exciton trapping). Trapping may either take place in a perfect crystalline environment (process is called self-trapping and the corresponding exciton is called self-trapped exciton - STE) or at lattice defects like a vacancy. Therefore, the co-existence of free and self-trapped excitons leads to simultaneous observation of different luminescence bands, all being caused by excitons (see section 3.4, p. 45).

3.3.1 Wannier-Mott and Frenkel excitons

The 'correct' theoretical description of the properties of the excitons is a complicated problem and therefore several approximations were developed. The most important parameter determing the properties of an exciton, is the distance between the electron and the hole involved. There exist two limiting cases for excitons, namely the so-called Wannier-Mott excitons (large-radius exciton) and the Frenkel excitons (small-radius exciton).

Wannier-Mott exciton

In the Wannier-Mott model [Wan37, Mot38, Kno63, Zim87], the electron and the hole are spatially well separated. They interact via the Coulomb forces and the atomistic structure of the solid can be neglected. Under these assumptions, the energy of the exciton (using SI system) is [Zim87]:

$$E_n(\overrightarrow{K}) = E_g - B^* \frac{1}{n^2} + \frac{\hbar^2 \overrightarrow{K}^2}{2(m_e + m_h)} \quad \text{and} \quad B^* = \frac{\mu e^4}{8\varepsilon_r^2 \varepsilon_o^2 h^2}, \tag{3.5}$$

where the second term is the internal energy of the exciton and the third term is due to the exciton centre-of-mass motion. Here $\mu = m_e m_h/(m_e + m_h)$ is the reduced mass of the exciton, m_e and m_h are the effective masses of electron and hole, $\overrightarrow{K}$ is the wave vector of the centre-of-mass motion, ε_r is the dielectric constant of the medium, B^* is called the binding energy of the exciton series and n is the main quantum number. Analogously to the hydrogen atom, the so-called exciton radii are defined as

$$r_n = \frac{h^2 \varepsilon_r \varepsilon_o}{\pi \mu e^2} n^2. \tag{3.6}$$

The Wannier-Mott model is a good approximation for exciton radii $r_n \gg$ lattice constant. Due to the small momentum of the photons, only exciton states at $\left|\overrightarrow{K}\right| \simeq 0$ are probed in photoexcitation measurements. Therefore, the third term in Eq. 3.5 can be ignored in present work.

Frenkel exciton

In the Frenkel model [Fre31, Zim87], the excitonic excitation of an insulator is approximately an atomic-type excitation. The hole and the electron are localized at the same lattice site, but the excitation can hop from one atom to another by virtue of the dipole-dipole interaction between neighbours. The Frenkel exciton excitation energy E_f from the ground state to the excited state f can be represented as

$$E_f(\vec{K}) = \Delta\epsilon_f + D_f + B_f(\vec{K}), \tag{3.7}$$

where (i) $\Delta\epsilon_f$ is the excitation energy of the free atom, (ii) D_f is the environmental energy shift resulting from interaction of one excited atom with all surrounding atoms of the lattice, (iii) $B_f(\vec{K})$ is the energy of the excitation transfer from one atom to another in the crystal [Fug78].

Intermediate exciton

The relative distance between electron and hole determines the validity of the Wannier-Mott and the Frenkel model. The Frenkel model is good for exciton radii smaller than the lattice constant, whereas the Wannier-Mott model works for exciton radii significantly larger than the lattice constant. For $n \geqslant 2$, the energies of excitons in all RGS are well described with the Wannier model, but the n=1 excitons in solid Ne can be interpreted as Frenkel excitons [Zim87]. The situation is more complicated for n=1 excitons in solid Xe, Kr and Ar, where the Wannier radius of the n=1 exciton is close to the lattice constant. That kind of excitons are called intermediate excitons.

It is important to point out that all members of excitonic series observable in reflection/absorption spectra are free excitons which can transport energy through the crystal. Nevertheless, in the literature (including this work), 'free exciton' is used very often as a synonym for the emission of n=1 exciton, since luminescence only from the lowest excitonic state, *i.e.* from the n=1 exciton is observable in the experiment.

3.3.2 Exciton polariton

To describe the line shape and the width of the n=1 and n'=1 excitons in absorption and reflection spectra, it is necessary to use the exciton-polariton model. Generally, the polariton model is used, if the coupling of the radiation field to the oscillator is so strong that it can no longer be treated as a small perturbation. In that case, Maxwell's equations inside the solid have to be solved in the presence of an oscillator which gives rise to polarization of the solid. If this oscillator is an exciton, the polariton is called exciton polariton. The basic concept of the exciton polariton is published in the books of Knox and Dexter [DK65, Kno63]. Special aspects of the exciton polariton in RGS are discussed by Kink and Selg [KS79] and as well by Fugol *et al.* [FGS82, Fug88]. In the present work, $\overrightarrow{K}$ is generally wave vector of the excitons and $\overrightarrow{k}$ is wave vector of the photons. However, in the case of exciton-polariton $\overrightarrow{K}$ and $\overrightarrow{k}$ are indistinguishable and therefore only $\overrightarrow{k}$ is used in this section.

The **Lorentz model** describes the classical interaction between an electromagnetic wave and a medium. In this model, a dispersive and absorbing medium is characterized as a collection of harmonic oscillators with mass m, charge -e, and natural (undamped) frequency ω_0, in the presence of a damping force. An electric field $\vec{E}(\vec{r},t)$ is taken into account in the plane-wave form

$$\vec{E}(\vec{r},t) = \vec{E}_0 \exp\left[i(\vec{k}\vec{r} - \omega t)\right] . \tag{3.8}$$

The oscillators interact with the electromagnetic field and the equation for each oscillator's

motion is

$$m\left(\frac{d^2}{dt^2}\vec{u}(\vec{r},t)+\gamma\frac{d}{dt}\vec{u}(\vec{r},t)+\omega_0^2\vec{u}(\vec{r},t)\right)=\vec{F}(\vec{r},t)=e\vec{E}(\vec{r},t), \tag{3.9}$$

where $\vec{u}(\vec{r},t)$ measures oscillators displacement from the equilibrium position and $\vec{F}(\vec{r},t)$ is applied force, generally an electrostatic force $e\vec{E}(\vec{r},t)$. Here, the phenomenological damping constant γ is used. As a result, the Lorentz model gives the frequency dependence on the complex dielectric constant as

$$\varepsilon(\omega)=1+\frac{\omega_p^2}{\omega_0^2-\omega^2-i\gamma\omega} \quad \text{with } \omega_p^2=\frac{Ne^2}{\varepsilon_0 m}, \tag{3.10}$$

where N is the density of the oscillators and ε_0 is the dielectric constant. Details about the Lorentz model are discussed *e.g.* in [DK65].

Proceeding from the Maxwell's equations, two possible solutions (transverse and longitudinal) exist for the plane harmonic waves (Eq. 3.8) in the medium. The **transverse solutions** ($\vec{E}\perp\vec{k}$) of the Maxwell's equations are determined by the condition [DK65, Kli95]

$$\frac{c^2k^2}{\omega^2}=\varepsilon(\omega), \tag{3.11}$$

where c is velocity of the light. If applying dielectric constant from the Eq. 3.10, then we obtain

$$\frac{c^2k^2}{\omega^2}=1+\frac{\omega_p^2}{\omega_0^2-\omega^2-i\gamma\omega}. \tag{3.12}$$

The analogous condition for the **longitudinal solution** ($\vec{E}\parallel\vec{k}$) is given with equation $\varepsilon(\omega)=0$ [DK65, Kli95], which yields, using Eq. 3.10

$$1+\frac{\omega_p^2}{\omega_0^2-\omega^2-i\gamma\omega}=0. \tag{3.13}$$

Such a solution does not exist in the vacuum, since ε_{vac}=1. In the case of a medium, the longitudinal solution is obtained from Eq. 3.13, and using γ=0 (damping is neglected), it is

$$\omega_L=\sqrt{\omega_p^2+\omega_0^2}. \tag{3.14}$$

This longitudinal solution does not have any dispersion.

The dielectric function (Eq. 3.10) for the simple case has to be modified if spatial dispersion effects are taken into account. Kink and Selg [KS79] described the dielectric constant especially for RGS as follows

$$\varepsilon(\omega,k)=\varepsilon(0)+\frac{f^2}{\Omega^2(k)-\omega^2-i\omega\Gamma(k)}. \tag{3.15}$$

Here, $\varepsilon(0)$ is the part of the dielectric constant which is independent from frequency, f^2 is proportional to the transition oscillator strength F and $\Gamma(k)$ is the phenomenological damping coefficient. The characteristic exciton frequency $\Omega(k)$ is given by the formula

$$\Omega(k) = \Omega_T + \frac{\hbar k^2}{2(m_e + m_h)}. \tag{3.16}$$

The quantity f^2 can be expressed through the low frequency limits of longitudinal (Ω_L) and transverse (Ω_T) excitons:

$$f^2 = \varepsilon(0)(\Omega_L^2 - \Omega_T^2). \tag{3.17}$$

A relation between the quantity f^2 and the oscillator strength F is

$$F = f^2 \cdot \frac{m_0 V}{4\pi e^2}, \tag{3.18}$$

where V is the volume of the elementary cell, m_0 is the free electron mass and e is the elementary charge [Dav76]. The oscillator strength is proportional to $\sim 1/n^3$ [Kno63]. It also means that $(\Omega_L^2 - \Omega_T^2) \sim 1/n^3$ and therefore polariton effects are not observable in the case of excitons with the main quantum number n$\geq$2.

Fig. 3.5 shows the dispersion curves for the exciton-polariton in two different scales of the wave-vector for solid Kr (dielectric constant from Eq. 3.15, damping is neglected). The region, where *k*-vectors are close to the photon wave vector, is shown on the left. The region of the *k*-vectors, which are significantly larger than the photon wave vector is depicted on the right. In Fig 3.5, the dispersion curve for a photon (dash-dot line), a longitudinal (dotted line) and a transverse exciton (dashed line) are also shown for solid krypton. Transverse exciton-polariton branches are marked with T_1 and T_2. The branch T_2 behaves like a photon if the energy is significantly smaller than $E_T = \hbar\Omega_T$ (*e.g.* point F) and the branch T_1 behaves like a photon if the energy is significantly larger than $E_L = \hbar\Omega_L$. If the wave vector of exciton-polariton is significantly longer than the photon wave vector, the exciton-polariton behaves like an exciton (*e.g.* point G).

Polariton effects are well pronounced, if

$$\frac{\Gamma}{2}\hbar \leq \Delta_{LT} = E_L - E_T \quad \text{[NTA80, Fug88].} \tag{3.19}$$

In the case of solid Kr, E_T=10.13 eV [Var94] and E_L=10.29 eV [Sai80], *i.e.* Δ_{LT} is ~0.16 eV. In solid Kr, the damping constant Γ is not known, but it is expected to be comparable with the value for solid Xe ($\hbar\Gamma$ smaller than 0.01 eV [Fug88]). Hence, the exciton-polariton description is applicable for solid Kr.

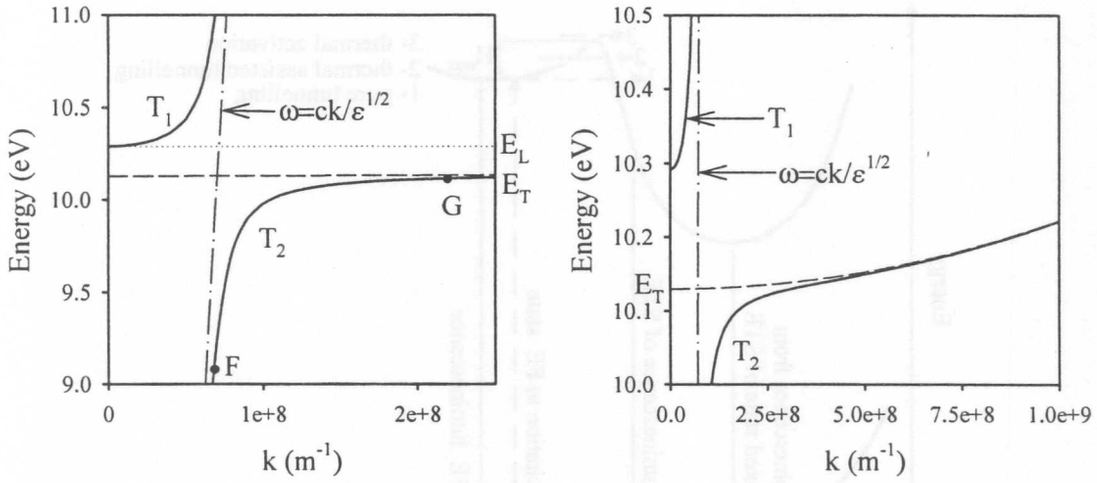

Figure 3.5: *Dispersion curves for the transverse branches (T_1, T_2 - solid lines) of an exciton-polariton in two different scales for solid Kr. The dielectric constant is taken from Eq. 3.15, damping is neglected. On the left: the length of k-vectors is comparable to the length of the photon wave vector. On the right: the k-vectors are significantly larger than the photon wave vector. Dispersion curves for a photon (dash-dot line), a transverse exciton (dashed line), and a longitudinal exciton (dotted line) are also shown. E_T and E_L mark the lowest energies of transverse and longitudinal excitons, respectively.*

3.4 Coexistence of free and self-trapped excitons

Free excitons (FE) and self-trapped excitons (STE) may coexist in crystals with broad exciton band, where FE and STE-states are energetically separated by a sufficiently high potential barrier. The heavy RGS (Kr and Xe) are of that kind, and the resonance emission of the FE and the Stokes-shifted emission of the STE are observable in the luminescence spectra. In a solid-state model two different approaches are used to describe FE and STE emissions. The FE emission is described in terms of delocalized state and effective-mass approximation, while for the emission of the trapped excitons (either self-trapped or trapped at lattice defects) a local-configuration coordinate model is applied [Zim87]. Using configuration coordinate, schematic potential curves for FE and STE state are shown in Fig. 3.6. Also different possibilities for the radiative decay of excitons are shown.

Two different kinds of STE exist in RGS: the molecular STE (m-STE) and the atomic STE (a-STE). The molecular STE can be treated as an excimer molecule in a RG matrix. The a-STE can be handled as an excited atom embedded in a matrix of the same kind of atoms. Since the a-STE is not observed in heavier RGS (Xe and Kr), in this work the abbreviation STE is always used for the molecular STE.

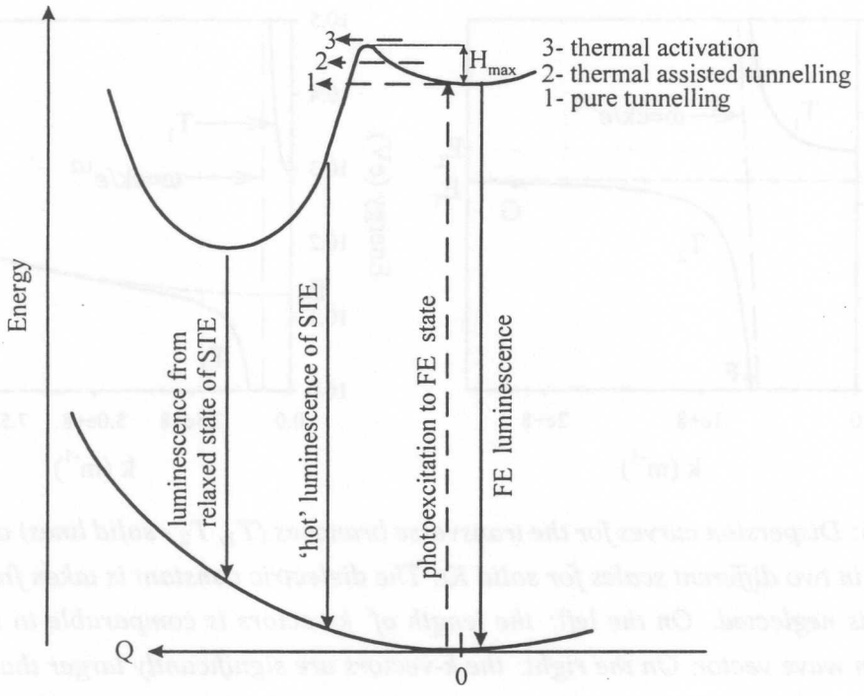

Figure 3.6: *Simplified potential curves for the FE and STE state. Q is the configuration coordinate and H_{max} is the barrier height between FE and STE state. Three different possibilities to pass the potential barrier are shown. Different possibilities for the radiative decay of the exciton are depicted as well.*

3.4.1 Trapping process

A transition from the metastable delocalized to the stable localized exciton state (overcoming the barrier) is called trapping. Trapping may either take place in a perfect crystalline environment (self-trapping) or at lattice defects like vacancies.

In first approximation, the total decay rate of FE is given by

$$\Gamma_{total} = \Gamma_{rad} + \Gamma_{ST} , \tag{3.20}$$

where Γ_{rad} is the radiative decay rate of FE and Γ_{ST} is the self-trapping rate for FE [Zim87]. In such a case, additional decay channels are neglected and the wavelength-integrated intensity ratio of FE and STE bands gives relation between Γ_{rad} and Γ_{ST}, which is

$$\frac{I_{FE}}{I_{STE}} = \frac{\Gamma_{rad}}{\Gamma_{ST}}. \tag{3.21}$$

This integral ratio has been measured for solid krypton by Roick (0.004 at 7 K) [Roi84] as well as by Varding (0.048 at 5 K) [Var94]. The best integral ratio of present work (0.04,

sample 13 at 6 K, excited by 10.42 eV photons) is comparable with Varding's result. Such a simple method gives a strongly overestimated value for Γ_{ST}, since significant non-radiative losses as well as exciton trapping near defects exist besides self-trapping. This estimation is supported by the data from experiments by Varding *et al.*, where the integral ratio of $I_{FE}/I_{STE} \approx 0.35$ was obtained in solid Xe [VRZ94]. In the past, Coletti and Debever were also able to grow Xe samples with extraordinarily strong FE luminescence (integral ratio of $I_{FE}/I_{STE} \approx 0.2 \ldots 0.1$) [Zim87].

The self-trapping rate Γ_{ST} of FE is determined by three fundamental processes [Ras81, Ras82]:

(i) quantum mechanical tunnelling,
(ii) thermal assisted tunnelling,
(iii) thermal activation.

All such processes are depicted in Fig. 3.6. Only quantum mechanical tunnelling occurs at absolute zero temperature. The possibility for processes (ii) and (iii) increases with rising temperature. Most probably, the thermal activation (iii) dominates at 'high' temperatures.

The self-trapping rate of the pure quantum mechanical tunnelling is independent from the temperature and may be roughly estimated as

$$\Gamma_{ST} \approx \omega D, \tag{3.22}$$

where D is the transparency of the barrier and ω is the characteristic phonon frequency [Ras82]. At sufficiently 'high' temperatures, the thermally activated self-trapping dominates and it is proportional to

$$\Gamma_{ST}(T) \propto exp\left(\frac{-H_{\max}}{k_B T}\right), \tag{3.23}$$

where H_{max} is the barrier height between FE and STE state and k_B is Boltzmann's constant. Most complicated temperature range is the one of thermal assisted tunnelling. Roick *et al.* [Roi84] fitted their experimental data with an analytical expression given by Rashba [Ras81]

$$\Gamma_{ST}(T) = \Gamma_{ST}(0) \cdot \frac{1}{(1 - T/\theta)^{\alpha}}, \tag{3.24}$$

where $\Gamma_{ST}(0)$ is the self-trapping rate for T$\rightarrow$0 (pure tunnelling), θ corresponds to the characteristic frequency of the phonon spectrum, and the coefficient α is connected with the density of the vibrational modes in initial states. From the fit, Roick *et al.* obtained for solid Kr $\Gamma(0)=1.3 \cdot 10^9$ 1/s and $\alpha=6.2$.

The simplest theory, which describes exciton-phonon interaction in RGS, is the continuum theory [Fug78]. In this theory, the interaction of the exciton with the lattice is characterized by a deformation potential. The continuum theory gives the barrier height between

Barrier heigth H_{max} (meV)	Comments and initial data	Reference
10	Continuum model, B = 0.45 eV, E_{LR}=1.38 eV	[Fug78]
4	Continuum model, B = 0.37 eV, E_{LR}=1.38 eV	present work
5	Green's function, B = 0.37 eV	present work
40	Tunnelling [NT81], Γ_0=1.3·10^{9}1/s, B=0.45 eV	[Roi84]
14	Tunnelling, Eq. 3.22 and 3.22, Γ_0=1.3·10^{9}1/s	[Roi84]
30	Corresponds to the maximal self trapping rate	[KS87]
15	Minimal barrier heigth	[KS87]

Table 3.3: *Estimated barrier heigths between FE and STE state in solid krypton.*

FE and STE state, described by

$$H_{max} = \frac{4}{27}\frac{B^3}{E_{LR}^2}. \tag{3.25}$$

Here, B denotes the exciton band half-width and E_{LR} is the lattice relaxation energy. On the basis of the continuum model, Fugol *et al.* estimated the barrier height for Kr equal to H_{max}=10 meV (B = 0.45 eV, E_{LR}=1.38 eV) [Fug78]. Applying a new exciton band half-width from present work (B=0.37 eV, see page 88) together with E_{LR} from [Fug78], the continuum model estimate for the barrier height is 4 meV. Unfortunately, the continuum model is oversimplified, especially in the case of heavier RGS (Kr and Xe) [Sel81].

Hizhnyakov and Sherman developed another theory [HS76], based on the exciton interaction with phonons at one lattice site in simple cubic crystals using the Green's function method. This theory is particularly applicable for the heavier RGS as Xe and Kr [Sel81] and predicts the following barrier height,

$$H_{\max} \approx \frac{4B^2}{9S^2}, \quad \text{where} \quad S^2 = \frac{8E_d^2}{\rho {v_l}^2 a^3}. \tag{3.26}$$

Here, a is the lattice constant, v_l is the longitudinal sound velocity, E_d is the deformation potential and ρ is the crystal density. Using the initial values from [Fug78] together with B = 0.37 eV from this work the equation 3.26 gives a barrier height of 5 meV.

Kmiecik and Schreiber made a detailed theoretical analysis and described the potential barrier between FE and STE state with the help of a potential surface, including distortion of the crystal [KS87]. They found that the smallest possible barrier height in solid Kr is 15 meV, but the highest and more realistic self-trapping rate is obtained for a 'narrow' barrier with a height of 30 meV.

Table 3.3 collects several estimations for the barrier height H_{max} in solid krypton. It demonstrates that the barrier height values have a large variation. Beside diverse theoretical approaches, rather poorly known initial parameters are the main reasons for such a discrepancy as well.

3.4.2 Radiative decay of the free exciton

The observed FE decay curves in solid Xe and Kr, excited in the excitonic region, show a non-exponential behaviour [VRZ94, Var94]. Such a temporal behaviour of the FE luminescence is described in a three-step model [VRZ94]. The model is sketched in Fig. 3.7. In the first step, it is assumed that the exciton-polaritons reach thermal quasi-equilibrium in the 'bottleneck' of the dispersion curve during the first 100 ps, which is an estimate for upper time-limit of this process determined by the experimental time-resolution (1 in Fig. 3.7a). The second step is the transport of the bottleneck exciton-polaritons (2 in Fig. 3.7b). The third step is due to the transmission of bottleneck exciton-polaritons into vacuum (3 in Fig. 3.7b).

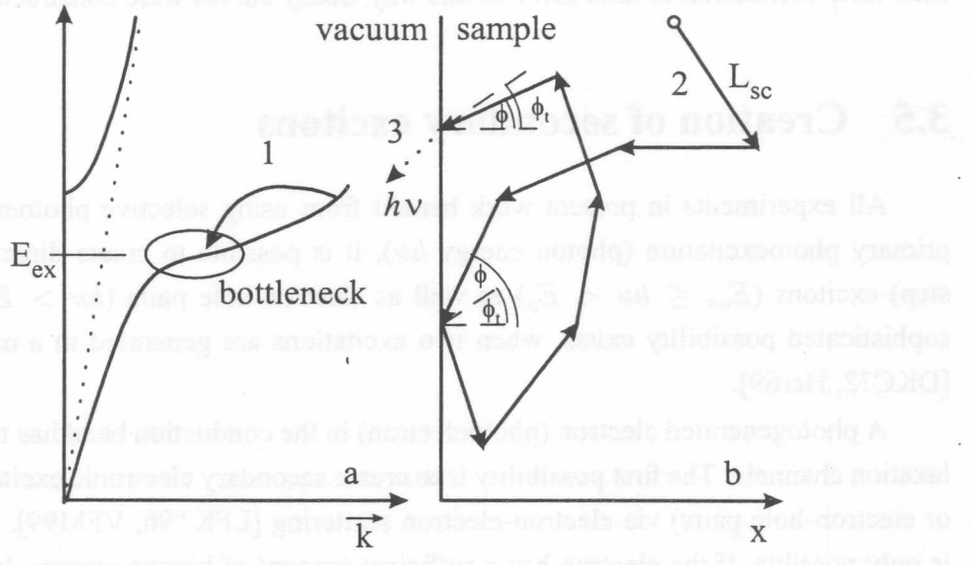

Figure 3.7: *a) Schematic dispersion curves and model of the population and the radiative decay of exciton-polaritons in RGS. b) Schematic model for the transport of exciton-polaritons to the sample/vacuum interface and transmission into the vacuum [VRZ94]. The following notations are used: φ_t: angle of total reflection, φ: angle of incidence, L_{sc}: scattering length, E_{ex}: energy of the FE.*

Varding *et al.* simulated the transport with Monte-Carlo method. At time zero, a bottleneck exciton-polariton was created at a certain depth, x, below the surface (Fig. 3.7b). The x-axis is perpendicular to the sample/vacuum interface. The particle starts moving with group velocity, v_g, into an arbitrary direction. As a rough estimate of the velocity, the average value $v_g=\sqrt{3k_BT/m_{ex}}$ with an effective mass of exciton $m_{ex}=m_e+m_h$ (sum of the effective masses of the electron and hole) was used. After a scattering length L_{sc}, the direction was changed arbitrarily. Trapping and non-radiative losses were taken into account in the following way: the probability for an exciton-polariton to exist after its motion along a scattering length was taken as $\exp(-\Gamma L_{sc}/v_g)$. Here, $\Gamma = \Gamma_{ST} + \Gamma_{nr}$ is the sum of the self-trapping rate Γ_{ST} and a rate describing other non-radiative processes Γ_{nr}. Concerning reflection at the sample-vacuum interface, total reflection was taken into account. The further motion of the reflected exciton-polaritons, including those which were totally reflected, was included in the simulations. The whole calculation has been repeated about 10^6 to 10^7 times for a semi-infinite sample. The damping of the exciting light along the x-axis according to the Beer's law was taken into account as a weight function for the individual events. All exciton-polaritons decaying in this way at the crystal surface were registered including their time-correlation to time zero. In this way, decay curves were constructed.

3.5 Creation of secondary excitons

All experiments in present work benefit from using selective photoexcitation. With primary photoexcitation (photon energy $h\nu$), it is possible to create directly (*i.e.* in one step) excitons ($E_{ex} \leq h\nu < E_g$) as well as electron-hole pairs ($h\nu > E_g$). Also more sophisticated possibility exists, when two excitations are generated in a one step process [DKC72, Her69].

A photogenerated electron (photoelectron) in the conduction band has two different relaxation channels. The first possibility is to create secondary electronic excitations (excitons or electron-hole pairs) via electron-electron scattering [LFK+96, VFM99]. Such a process is only possible, if the electron has a sufficient amount of kinetic energy. In that case, one photon finally creates two electronic excitations, but this happens in two steps as it will be discussed later in more detail. Such kind of creation of secondary electronic excitations is observable in excitation spectra as an increase of the quantum efficiency. In some semiconductors (*e.g.* ZnS) the width of the valence band exceeds the band-gap and a 'hot' photohole and electron both have energy enough to induce further ionization. But in RGS the width of the valence band (in Kr 2.3 eV) is much smaller than the band gap energy (in Kr E_g=11.59 eV) and therefore, 'hot' holes cannot create any secondary electronic excitations.

The second possibility concerns energy losses via scattering on acoustic phonons (thermalization). After thermalization to the bottom of the conduction band, an electron can interact with a hole resulting in FE formation through electron-hole recombination [RGK+99]. The probability for electron-electron scattering is significantly higher than for electron-phonon scattering, because only acoustic phonons are present in RGS. Therefore, electron-electron scattering takes place first. If the electrons do not have enough energy for the creation of secondary electronic excitations, relaxation proceeds through electron-phonon scattering.

In this thesis, an essential point is the creation of primary and secondary FE. Exciton production with direct photoexcitation in the energy interval ($E_{ex} \leq h\nu < E_g$) is classified here as the primary FE creation, because all Wannier excitons relax to n=1 FE state 'immediately' in the time scale of the SUPERLUMI set-up. Likewise, exciton formation via the 'electronic polaron complex' mechanism (simultaneous creation of the exciton and an electron-hole pair in a *one step process*) is treated as primary creation of FE. FE formation via electron-hole recombination and via electron-electron scattering are classified as the secondary FE creation. In order to avoid misunderstanding, it is important to point out that in some papers the formation of electronic polaron complex is classified as secondary creation of FE.

3.5.1 FE creation via electron-hole recombination

The observation of FE luminescence following creation of free electron-hole pairs in solid krypton clearly shows that free excitons are formed in electron-hole recombination. The same is observed for solid Xe as well [RGK+99]. For solid Kr, it is generally supposed that holes self-trap within a few picoseconds. It means that recombination of mobile electrons and self-trapped holes leads to the formation of delocalized FE. This is by far non-trivial because in the past it was assumed that trapped holes capture electrons forming STE. The latter mechanism is not ruled out by results of this work, but it is at least not only the recombination process. Whether the STE observed, following creation of free electron-hole pairs, originate exclusively from self-trapping of free excitons or also from the capture of electrons by self-trapped holes will be discussed in section 4.7.

The FE formation via electron-hole recombination is sketched in Fig. 3.8. The electron and hole created in photoexcitation (1) lose energy via scattering on acoustic phonons and relax (2) to the bottom of the conduction band or to the top of the valence band, respectively. Thereafter, formation of the FE occurs (3).

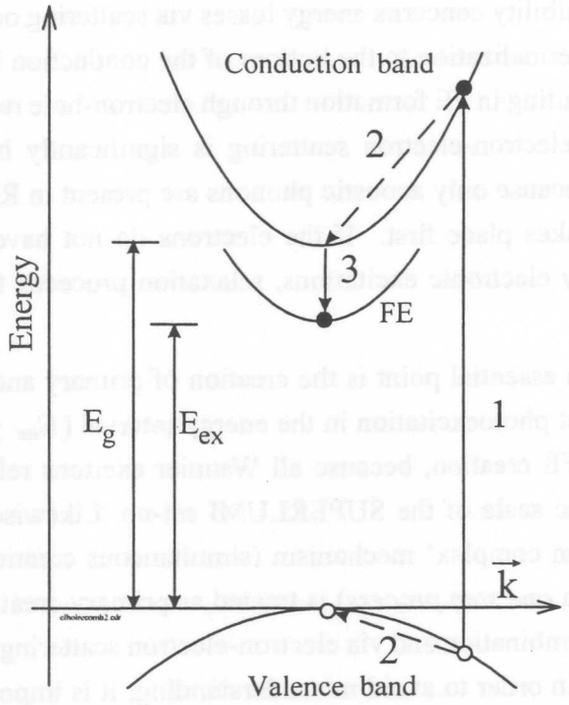

Figure 3.8: *A simplified model of FE creation via electron-hole recombination. A solid arrow (1) indicates a photoexcitation producing the primary electron-hole pair. Dashed arrows (2) depict relaxation of the electron and the hole. A short solid arrow (3) shows recombination of a relaxed electron-hole pair into the free exciton (FE) state. The band gap energy (E_g) and the FE energy (E_{ex}) are also shown.*

It is important to note, that the experimental decay curves of the FE, excited above the band gap energy, exhibit a 'prompt' (in time-scale of SUPERLUMI set-up) and a 'slow' component (see section 4.5.1). The model presented in this section describes the 'slow' component of measured FE decay curves. The origin of the 'prompt' component is not fully understood and will be discussed afterwards (section 4.5.1).

The description of the model requires a discussion of the initial conditions (kinetic energies and spatial density of the photocarriers immediately following the excitation pulse). The energy parameter, used in the calculations, is the excess energy E_{excess}. This is that part of the photon energy $h\nu$ exceeding the band gap energy E_g:

$$E_{excess} = h\nu - E_g \, . \tag{3.27}$$

According to energy and momentum conservation laws, at a given excess energy the electron and hole (effective masses m_e and m_h) gain an initial kinetic energy E_e and E_h

[LFK+96]:

$$E_{e,h} = \frac{m_{h,e}}{m_e + m_h} E_{excess} \,. \tag{3.28}$$

Using such an approximation in the case of RGS is rather restricted. The maximum hole energy is principally limited by the relatively narrow valence band. The total width of the valence bands (including both the j=3/2 and j=1/2 sub-bands) is about 2.3 eV in solid Kr [SHS+75]. Even stronger limitations are caused by the anisotropy of the hole mass, since the effective-mass tensor of the holes is strongly anisotropic [Rat96, KM73]. For example, the calculation by Bacalis *et al.* [BPP88] shows that the upper valence band in the Γ-L direction of the Brillouin zone has nearly no dispersion. This would give rise to a larger initial energy for the electrons than calculated from Eq. 3.28. Additionally, electron and hole effective masses are not exactly known. Therefore, the initial energy distribution between holes and electrons calculated from Eq. 3.28 is only a rough estimate.

The crucial point in this model is the created carrier density after photoabsorption. It can be estimated from the absorption coefficient α (penetration depth of the light is $\sim 1/\alpha$) at the respective photon energy of excitation, from the photon flux, and from the size of the illuminated area of the exciting radiation on the sample. In spite of several absorption measurements for solid Kr [Bal62, HHM78, SW71], the values of the absorption coefficient α are not exactly known. Notwithstanding of simple principles, absolute absorption measurements are complicated due to surface effects, perturbing luminescence signal, not exactly known sample thickness and reflection coefficient *etc.* In the present work, Baldini's absorption data were used, measured through roughly 100 Å thick Kr layer [Bal62]. Baldini estimated $\alpha \sim 3.5 \cdot 10^6$ 1/cm for the excitation at the maximum of the n=1 exciton reflection peak and $\alpha \sim 1.25 \cdot 10^6$ 1/cm at 12.0 eV [Bal62]. A similar value for the absorption coefficient of the n=1 exciton maximum is presented also by Scharber and Webber [SW71]. Despite the good agreement between two values for the n=1 exciton, the situation above the band gap is not so clear, since only Baldini's results are available in this region. The absolute value of reflectivity is uncertain as well. Several works about solid Kr reflectivity exist, but only little information about the absolute reflection coefficient is available. Scharber and Webber [SW71] as well as Steinberger *et al.* [SMW77] estimated the reflection coefficient at the maximum of n=1 exciton to be ~50 %. In the region above the band gap (E_g=11.59 eV) and below 12.5 eV, both groups agreed that the reflection coefficient is between 5 and 10 %. Since calculations in this work deal with the absorption above the band gap, reflection losses induce no significant error. Another experimental parameter, namely the width of the strongly asymmetric focal area (length ≈ 4 mm, width ≈ 0.2 to 0.4 mm) is not easily measurable. Also, data on the photon flux are based on old measurements from

1991 [Zim91]. The precise spectral distribution of the latter quantity depends on the used diffraction grating, which is replaced every few years. Taking into account all uncertainties, the created carrier density is estimated to be in the order of $\sim 10^{18}$ 1/m^3 (DORIS current $\sim$100 mA, *multi bunch mode*, primary monochromator resolution $\sim$2.5 Å). It is important to note that creation of 'hot' carriers takes place during synchrotron radiation pulses with duration of 130 ps (FWHM).

As was shown by experiments of 'hot' electron relaxation in semiconductors [SRLB92], on a short time scale (far below the time resolution of the present experiment) a redistribution of carriers, which is attributed to carrier-carrier interaction results in quasi-equilibrium electron and hole temperatures (T_e and T_h). For semiconductors, the time required to establish Maxwellian-like velocity distribution is estimated to be in the sub-picosecond regime [BKM+96]. The carrier density N_0, established during redistribution, is treated in the present model as an adjustable parameter.

Starting from this point, the energy relaxation of charge carriers is mainly due to scattering on longitudinal acoustic phonons, described by the deformation potential theory. In the deformation potential framework, electron scattering is possible only with longitudinal phonons [Con67, Zim62]. The electron mean free path (l_{free}), determined by scattering on acoustic longitudinal phonons, equals

$$l_{free} = \frac{\pi \hbar^4 \rho v_l^2}{m_e^2 E_d^2 k_B T_L}. \tag{3.29}$$

Here, E_d is the deformation potential, ρ is the crystal density, k_B is the Boltzmann's constant, T_L is the lattice temperature (*i.e.* crystal temperature), v_l is the longitudinal sound velocity, h is the Planck's constant and $\hbar$=$h/2\pi$. The average energy loss rate per electron (hole) in a Maxwellian distribution of temperature T_e (T_h) is given originally by Shockley [Con67]:

$$\left\langle \frac{dE_{e,h}(t)}{dt} \right\rangle_{ac} = -\frac{8\sqrt{2} E_d^2 m_{e,h}^{5/2}}{\pi^{3/2} \hbar^4 \rho} (k_B T_{e,h})^{3/2} \left(\frac{T_{e,h} - T_L}{T_{e,h}} \right). \tag{3.30}$$

The most important feature of the relaxation arises from the $m^{5/2}$ term. With m_e=0.42·m_0 (m_0 is the free electron mass) and m_h=3.6·m_0, it turns out that holes lose their kinetic energy at least two orders of magnitude faster than electrons. Therefore, in the following it will be assumed that T_h=T_L. The temperature dependence of density is published for solid Kr in [KV77] and its value is $\rho_{T=5K}$=3092.6 kg/m^3. Accurate data are available also for the longitudinal sound velocity being equal to $v_{l,T=5K}$=1370 m/s [BTB72].

Values for the deformation potential as well as for the electron effective mass are not exactly known. There are only several estimations available. Nevertheless, both parameters can be eliminated using a relation between E_d and m_e. Namely, it is possible to use the

phonon-limited low-field electron mobility μ_0 data. An equation for the low-field electron mobility is

$$\mu_0 = \frac{2}{3}\frac{\sqrt{2\pi}e\hbar^4\rho v_l^2}{E_d^2 m_e^{5/2}(k_B T_L)\sqrt{kT_e}}, \tag{3.31}$$

where T_L is the lattice temperature and T_e is the electron temperature [Con67, Zim62], e is the elementary charge, and v_l is the longitudinal velocity of sound. Another similar formula is also widely used with slightly different numerical coefficient, but coefficient $2\sqrt{2\pi}/3$ derived by Conwell is expected to be more 'precise' [FJ91]. In the case of low-field mobility experiments $T_L \approx T_e$ [MHS68].

Low-field mobility data for RGS were published by Miller *et al.* [MHS68]. In the case of solid Ar they measured the mobility at different temperatures and demonstrated experimentally that a $T^{-3/2}$ dependency exists. This shows clearly that thermalization is determined by scattering on acoustic phonons. They measured the mobility for solid Kr at T=113 K as well, *i.e.* slightly below the triplet point, and reported a value of 0.37 m^2/Vs.

For RGS, low-field mobility data to determine E_d and m_e were used for the first time by Druger [Dru71]. He used the mobility data by Miller *et al.* [MHS68]. More accurate values for density of solid Kr and longitudinal sound velocity ($\rho_{T=113K}$=2797 kg/m^3 [KV77], $v_{l,T=113K}$=1093 m/s [BTB72]) were published after Druger's work and therefore, an improved value is obtained for $E_d^2 m_e^{5/2}$:

$$E_d^2 m_e^{5/2} = \frac{2\sqrt{2\pi}e\hbar^4}{3k_B^{3/2}}\frac{\rho_{T=113K} v_{l,T=113K}^2}{\mu_{0,T=113K} T_{T=113K}^{3/2}}. \tag{3.32}$$

For solid krypton, the numerical value for this experimental coefficient C_{exp}, which will be used in further simulations, is:

$$C_{exp} = E_d^2 m_e^{5/2} = 4.83 \cdot 10^{-114}\ J^2 kg^{5/2} = 0.238\ eV^2 {m_o}^{5/2}. \tag{3.33}$$

For solid Ar, besides the results of Miller *et al.* [MHS68], two additional measurements are available, giving 1.7 and 3 times larger values for μ_0 [Asc89]. The reason for these differences is assumed to be a better sample quality compared to Miller *et al.* [Asc89]. Therefore, it is not excluded that the value of the experimental coefficient C_{exp}= $E_d^2 m_e^{5/2}$ in solid krypton is significantly overestimated.

The estimations for E_d, known from literature, are found also on the basis of mobility data using different electron masses, sound velocities and crystal densities. For example, Ratner estimates E_d=1.01 eV using electron effective mass m_e=0.71m_0 [Rat96] and Druger E_d=1.2 eV (m_e=0.62m_0) [Dru71]. The author of the present work obtained a value E_d=1.4 eV from C_{exp}=0.238 $eV^2 {m_o}^{5/2}$ using m_e=0.42 m_0.

Exciton formation from electrons and holes is treated with a simple set of Boltzmann kinetic equations. This is possible because the parameters involved have a clear physical sense, and because the processes can be described in the effective temperature approximation, including all temperature effects in the cross-section and in the relative velocity:

$$\frac{dn_e(t)}{dt} = G(t) - \sigma(T_e)n_e(t)n_h(t)v_{rel}(T_e) - \frac{n_e(t)}{\tau_{nr}} \tag{3.34}$$

$$\frac{dn_h(t)}{dt} = G(t) - \sigma(T_e)n_e(t)n_h(t)v_{rel}(T_e) \tag{3.35}$$

$$\frac{dn_{ex}(t)}{dt} = n_e(t)n_h(t)\sigma(T_e)v_{rel}(T_e) - \frac{n_{ex}(t)}{\tau_{rad}}. \tag{3.36}$$

Here, n_e, n_h and n_{ex} are the electron, hole, and exciton densities, respectively. $\sigma(T_e)$ is the recombination cross-section, $G(t)$ is the generation rate for electrons and holes and τ_{rad} is the decay time for FE luminescence excited in the excitonic region. Eq. 3.35 does not contain a non-radiative loss term for holes, since independently whether the holes are free or trapped, their recombination with mobile electrons takes place. Since FE decay curves have a non-exponential nature, an experimental FE decay curve, measured in the excitonic region slightly below the band-gap, is used instead of τ_{rad} in calculations. The non-radiative losses of electrons are characterized with τ_{nr}, what includes, *e.g.*, electron trapping. The existence of electron trapping is clearly shown by thermoluminescence measurements [KKK+97]. However, nature of electron traps is not exactly known. The average relative velocity between electrons and holes (v_{rel}) is described by

$$v_{rel} = \sqrt{\frac{8k_BT_e}{\pi\mu}}, \tag{3.37}$$

where μ is the reduced mass of the exciton [APY80]. The time-dependence of the electron temperature T_e is calculated from Eq. 3.30 via

$$\frac{dE_e(t)}{dt} = \frac{3k_B}{2}\frac{dT_e(t)}{dt} \tag{3.38}$$

and the formula for the average electron temperature loss is

$$\left\langle \frac{dT_e(t)}{dt} \right\rangle_{ac} = -A\sqrt{T_e}\,(T_e - T_L)\,, \tag{3.39}$$

where A is given as

$$A = \frac{16\sqrt{2}E_d^2 m_e^{5/2}\sqrt{k_B}}{3\pi^{3/2}\hbar^4\rho}. \tag{3.40}$$

An analytical mathematical solution for the electron temperature $T_e(t)$ (see details in Appendix A.) is

$$T_e(t) = T_L \left[\frac{1 + \exp\left(-At\sqrt{T_L} + \frac{1}{\sqrt{T_0}} \ln\left(\frac{\sqrt{T_0} - \sqrt{T_L}}{\sqrt{T_0} + \sqrt{T_L}} \right) \right)}{1 - \exp\left(-At\sqrt{T_L} + \frac{1}{\sqrt{T_0}} \ln\left(\frac{\sqrt{T_0} - \sqrt{T_L}}{\sqrt{T_0} + \sqrt{T_L}} \right) \right)} \right]^2 . \tag{3.41}$$

The calculation of the cross-section σ for electron-hole recombination is based on the theory of Abakumov *et al.* [APY80], in which the exciton formation is treated as a continuation of energy relaxation of charge carriers into the negative excess energy region, *i.e.* into bound states. Abakumov *et al.* assumed thermal equilibrium between holes and electrons ($T_e = T_h$) and the original cross-section (Eq.13 in [APY80]) is given by

$$\sigma(T_e)_{[APY80]} = \frac{16\sqrt{2}e^6 E_d^2}{3\sqrt{3\pi}\hbar^4 s\rho\varepsilon_0^3\varepsilon_r^3} \frac{m_e^3 \cdot m_h}{(m_h + m_e)^{1.5}} \frac{\sqrt{k_B T_e}}{(k_B T_e)^3}, \tag{3.42}$$

where ε_0 is the dielectric constant and ε_r=1.88 is the dielectric permittivity of solid Kr.

In the present case, electrons and holes are obviously not in equilibrium. In Abakumov's approach, the particle temperatures enter the final result only via the distribution functions and particle velocities. The parameter describing the magnitude of energy loss via scattering on longitudinal acoustic (LA) phonons (energy loss rate per propagation length) does not depend on the particle energy. Consequently, Eq. (11) from the paper by Abakumov *et al.* [APY80] describing the distribution of the electron-hole pairs can be modified by replacing T^3 by $T_e^{3/2} T_L^{3/2}$ [RGK+99]. Then it follows:

$$\sigma(T_e)_{[RGK+99]} = \frac{16\sqrt{2}e^6 E_d^2}{3\sqrt{3\pi}\hbar^4 s\rho\varepsilon_0^3\varepsilon_r^3} \frac{m_e^3 \cdot m_h}{(m_h + m_e)^{1.5}} \frac{1}{\sqrt{k_B T_L}\,(k_B T_e)^2} . \tag{3.43}$$

To avoid misunderstandings, it is important to point out that this equation is presented in a slightly different form in the original paper [RGK+99]

$$\sigma(T_e) = \frac{16\sqrt{2}e^6 E_d^2}{3\sqrt{3\pi}\hbar^4 s\rho\varepsilon_0^3\varepsilon_r^3} \frac{m_e^3}{\sqrt{m_h}} \frac{1}{\sqrt{k_B T_L}\,(k_B T_e)^2} , \tag{3.44}$$

where $m_h \gg m_e$ was assumed.

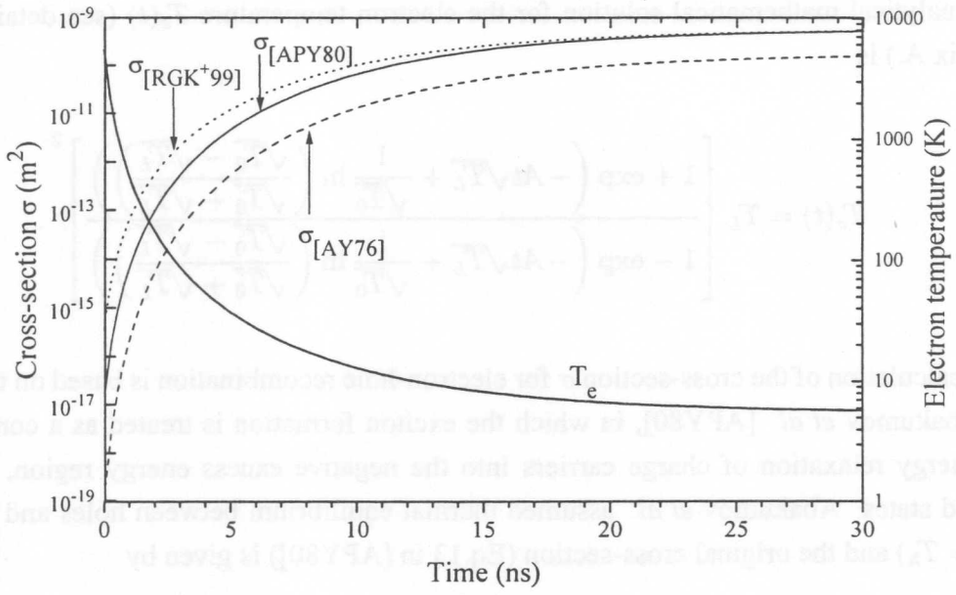

Figure 3.9: *Time-evolution of the electron temperature T_e and cross-section for electron-hole recombination using Abakumov's approach ($T_e = T_h$) [APY80], modified Abakumov's approach ($T_e \neq T_h = T_L$) [RGK+99] and the cross-section for capture of electrons at positively charged centers [AY76]. The temperature is given in K and the cross-sections are given in m^2.*

There are other theoretical approaches available in the literature. For solid Kr, it is generally supposed that the holes self-trap during a few picoseconds. Then the recombination of a self-trapped hole (STH) and an electron can be treated as that of an electron with a positively charged center. Abakumov and Yassievich [AY76] developed for this type of recombination in semiconductors the following equation,

$$\sigma(T_e)_{[AY76]} = \frac{64}{24} \frac{(e^2 Z)^3 m_e^3 E_d^2}{\rho \varepsilon_0^3 \varepsilon_r^3 \hbar^4} \frac{1}{(k_B T_e)^3}, \tag{3.45}$$

where eZ is the charge of the recombination centre (in the present case Z=1).

The presented recombination cross-sections include E_d and m_e. Again it is reasonable to use known physical relations and to replace $E_d^2 m_e^{5/2}$ with the experimentally obtained coefficient (see Eq. 3.33). Thereafter, the only uncertain parameter in the cross-sections is $\sqrt{m_e} \cdot m_h \cdot (m_h + m_e)^{-1.5} \approx \sqrt{m_e/m_h}$ (Eq. 3.42 and 3.43) or $\sqrt{m_e}$ (Eq. 3.45). However, such dependencies are relatively weak due to the square root.

Fig. 3.9 shows the time-evolution of the electron-temperature and of the three different cross-sections (*i.e.* for each theoretical approach). The numerical values of the used parameters are: E_{excess}=788 meV, N_0=2·10^{15} 1/m^3, T_L=5.5 K, $E_d^2 m_e^{5/2}$=4.83·10^{-114} J^{2}kg$^{5/2}$,

ρ=3092.6 kg/m^3, Γ_{nr}=5 · 10^7 1/s (τ_{nr}=20ns), v_l=1370 m/s. As Fig. 3.9 demonstrates, all cross-sections have a similar general behaviour, nevertheless, the absolute values are quite different.

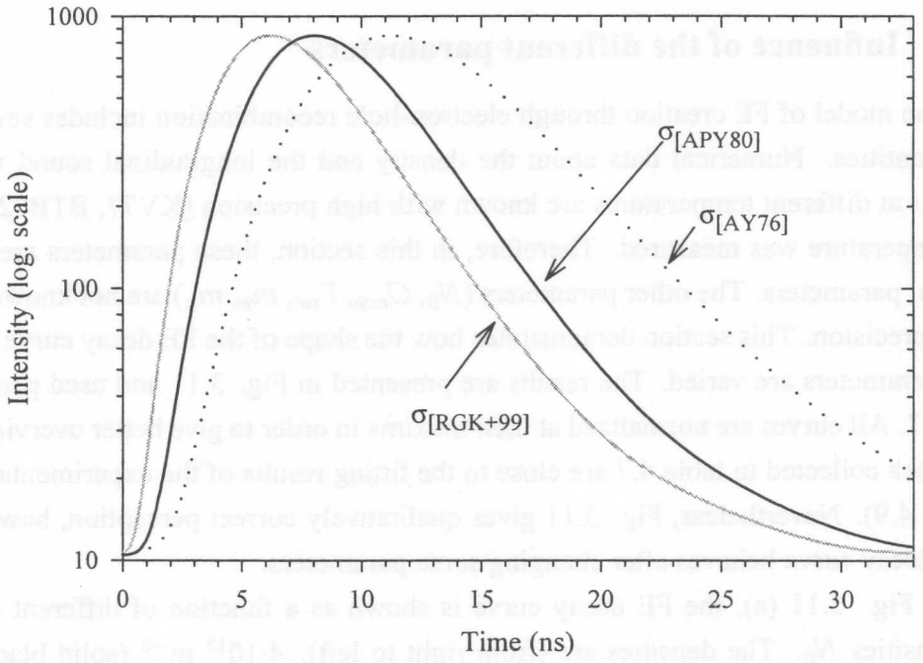

Figure 3.10: *Influence of the different cross-sections (i.e. various theoretical approaches) on the calculated FE decay curves: Abakumov's approach ($T_e = T_h$) [APY80], modified Abakumov's approach ($T_e \neq T_h = T_L$) [RGK$^+$99] and the cross-section for capture of electrons at positively charged centers [AY76]. All curves are normalized at their maxima.*

Fig. 3.10 shows how the different cross-sections influence the shape of the decay curve. All parameters are fixed and only different cross-section formulas are used. The following parameters were used: E_{excess} = 788 meV, N_0=4·10^{14} 1/m^3, T_L =5.5 K, ρ =3092.6 kg/m^3, $E_d^2 m_e^{5/2}$ =4.83·10^{-114} $J^2 kg^{5/2}$, Γ_{nr} = 1 · 10^8 (τ_{nr} = 10 ns), v_l =1370 m/s. The behaviour of the shape of decay curves is in accordance with the cross-section values, demonstrated in Fig. 3.9. The decrease of the cross-section in the sequence $\sigma_{[RGK+99]} \rightarrow \sigma_{[APY80]} \rightarrow \sigma_{[AY76]}$ causes the shift of the maximum of the decay curve to longer times. As shown in Fig. 3.10, the remarkable intensity increase of the decay curve seems to start with a delay of 0.5...1 ns. Of course, recombination starts at t=0, however, with an extremely small cross-section. The finite value of the intensity in Fig. 3.10 at t=0 is an artefact because an experimental decay curve used in the calculations. This experimental curve has a background signal (detector noise) which was not completely removed.

In this section, in most cases, an initial carrier density N_0 ~4·10^{14} 1/m^3 was used. This

is much smaller than the density of created electron-hole pairs, estimated on the basis of absorption coefficient and photon flux ($\sim 10^{18}$ 1/m^3). The reasons for that will be discussed in chapter 4.9.

3.5.2 Influence of the different parameters

The model of FE creation through electron-hole recombination includes several physical quantities. Numerical data about the density and the longitudinal sound velocity of solid Kr at different temperatures are known with high precision [KV77, BTB72]. The lattice temperature was measured. Therefore, in this section, these parameters are treated as 'known' parameters. The other parameters (N_0, C_{exp}, Γ_{nr}, m_e, m_h) are not known with sufficient precision. This section demonstrates how the shape of the FE decay curve changes if these parameters are varied. The results are presented in Fig. 3.11 and used parameters in table 4.7. All curves are normalized at their maxima in order to give better overview. Not all the values collected in table 4.7 are close to the fitting results of the experimental data (see chapter 4.9). Nevertheless, Fig. 3.11 gives qualitatively correct perception, how the shape of the decay curve behaves after changing some parameters.

In Fig. 3.11 (a), the FE decay curve is shown as a function of different initial carrier densities N_0. The densities are (from right to left): $4{\cdot}10^{13}$ m^{-3} (solid black), $4{\cdot}10^{14}$ m^{-3}(solid grey), $4{\cdot}10^{15}$ m^{-3} (dashed black), $4{\cdot}10^{16}$ m^{-3} (solid black), $4{\cdot}10^{17}$ m^{-3} (solid gray). As the figure demonstrates, 'larger' initial carrier density causes faster decay and narrowing of the shape of the curve. As mentioned before, the electron-hole recombination model includes also a convolution procedure using the experimental FE luminescence decay curve, excited in the excitonic region. At 'very high' densities the shape of the simulated curve is determined by this experimental FE decay curve and does not change any more with an additional increase of the initial carrier density. This happens, because relaxation of the electrons and the FE creation at 'very high' initial carrier densities are much faster than the FE decay itself. The peculiarities on the level of the back-ground intensity in the region 10 ... 30 ns are computing artefacts, caused by the detector noise in the experimental FE decay curve used. The decrease of the initial carrier density shifts the maximum of the decay curve to longer times and causes its broadening. Increase of the initial carrier density leads to an increase of the total intensity of the FE emission as well. Such effects are not visible in Fig. 3.11, but are demonstrated separately in Fig. 3.12 (a). Our recent experiments with varied excitation intensity (undulator source) demonstrated analogous behaviour as predicted by the model described above [Vie02].

Fig. 3.11 (b) shows, how the non-radiative losses influence the FE decay curves. The non-radiative losses can be characterized either with a decay rate Γ_{nr} or with a lifetime

	Symbol	Unit	Value
Effective electron mass	m_e	m_0	0.42
Effective hole mass	m_h	m_0	3.6
Initial carrier density	N_0	$1/m^3$	$4 \cdot 10^{14}$
$E_d^2 m_e^{5/2}$	C_{exp}	$J^2 kg^{5/2}$	$4.83 \cdot 10^{-114}$
Excess energy	E_{exc}	meV	788
Longitudinal sound velocity	v_l	m/s	1370
Crystal temperatur	T_L	K	5.5
Non-radiative losses	Γ_{nr}	1/s	$1.5 \cdot 10^8$
Non-radiative losses	τ_{nr}	ns	6.7
Density of solid Kr (at 5K)	ρ	kg/m^3	3092.6

Table 3.4: *Numerical values of the quantities used in simulations of the decay curves shown in Fig. 3.11 and 3.12 .*

$\tau_{nr}=1/\Gamma_{nr}$. The values used in the calculations are (from right to left): $\Gamma_{nr}=5 \cdot 10^7$ 1/s or $\tau_{nr}=20$ ns (solid black), $\Gamma_{nr}=1 \cdot 10^8$ 1/s or $\tau_{nr}=10$ ns (solid grey), $\Gamma_{nr}=2 \cdot 10^8$ 1/s or $\tau_{nr}=5$ ns (dashed black), $\Gamma_{nr}=3 \cdot 10^8$ 1/s or $\tau_{nr}=3.33$ ns (solid grey), $\Gamma_{nr}=5 \cdot 10^8$ 1/s or $\tau_{nr}=2$ ns (solid black). The higher non-radiative losses shift the decay to shorter times. In the case of extremely high non-radiative losses, the shape of FE decay again coincides with the experimental curve used for the convolution. Smaller non-radiative losses cause a shift of the maximum of the decay curve to longer times and an increase of the width of the decay curve. An increase of Γ_{nr} induces as well a decrease of the total intensity (see Fig. 3.12).

The changes arising from a variation of the experimentally determined coefficient $C_{exp} = E_d^2 m_e^{5/2}$ (see Eq. 3.33), are shown in Fig. 3.11 (c). The used values are (from right to left): $0.5 \cdot C_{exp}$ (solid black), $0.8 \cdot C_{exp}$ (solid grey), $1 \cdot C_{exp}$ (dashed black), $1.2 \cdot C_{exp}$ (solid grey), $1.5 \cdot C_{exp}$ (solid black). A small change of this value causes remarkable changes in the shape of FE decay curve. It is natural, since this coefficient is included in the electron temperature (Eq. 3.30) as well as in the equations of the cross-sections (Eq. 3.42, 3.43, 3.45). Moreover, the cross-section includes once again the electron temperature, thus amplifying the influence of $C_{exp} = E_d^2 m_e^{5/2}$.

Fig. 3.11 (d) depicts the dependency of the decay curve on the value of the effective electron mass m_e. The following effective masses were used in the simulations (from right to left): $m_e=2.1 \cdot m_0$ (solid black), $m_e=0.84 \cdot m_0$ (solid grey), $m_e=0.084 \cdot m_0$ (dashed black). In principle, the presented model is very sensitive to the electron effective mass, but since the experimentally determined coefficient $C_{exp} = E_d^2 m_e^{5/2}$ contains already $m_e^{5/2}$,

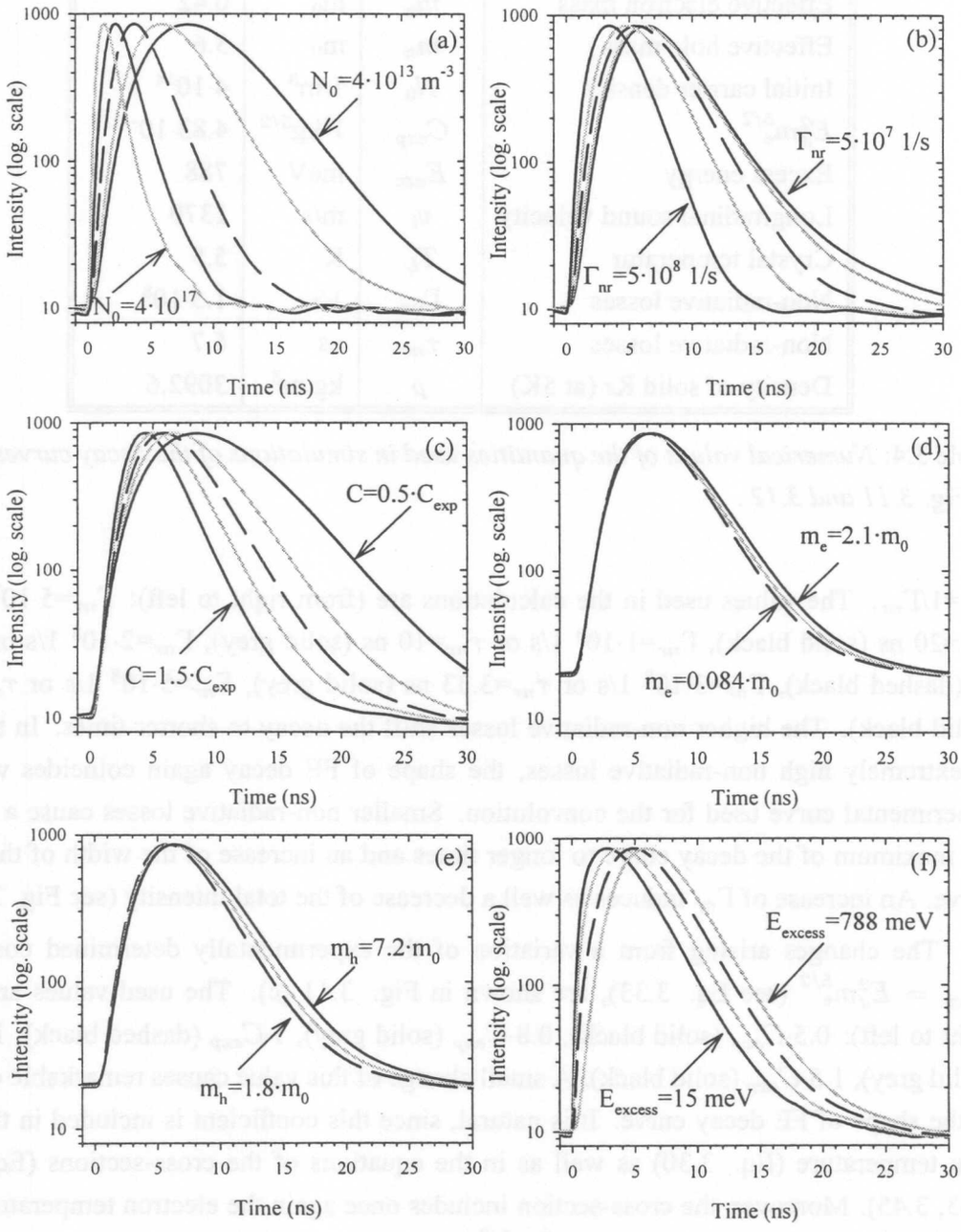

Figure 3.11: *Influence of the variation of the different parameters on the calculated shape of the FE decay curve: (a) initial carrier density N_0, (b) non-radiative losses Γ_{nr}, (c) experimental coefficient $C_{exp}=E_d^2 m_e^{5/2}$, (d) effective electron mass m_e, (e) effective hole mass m_h, (f) excess energy E_{excess}. All curves are normalized at their maxima.*

the remaining influence of the electron mass is rather weak (C_{exp} is not varied). Cross-sections $\sigma(T_e)_{[RGK+99]}$ and $\sigma(T_e)_{[APY80]}$ include (beside $E_d^2 m_e^{5/2}$) a dependency of the form $\sqrt{m_e} \cdot m_h \cdot (m_h + m_e)^{-1.5} \approx \sqrt{m_e/m_h}$ and $\sigma(T_e)_{[AY76]}$ is a function of $\sqrt{m_e}$. Moreover, the relative velocity (Eq. 3.37) contains a term $\sqrt{1/\mu}$. It means that a dependency either of the form $\sqrt{m_h}/(m_h + m_e)$ (for $\sigma(T_e)_{[RGK+99]}$ and $\sigma(T_e)_{[APY80]}$) or $\sqrt{(m_e + m_h)/m_h}$ (for $\sigma(T_e)_{[AY76]}$) is present in the kinetic equations (3.34, 3.35 and 3.36). Since m_e is significantly smaller than m_h, its influence is much weaker than the influence of m_h.

Fig. 3.11 (e) demonstrates the shape of the FE decay curve in the case of different effective hole masses m_h (C_{exp} was kept fixed again). An increase of m_h causes a broadening of the decay curve. The used m_h values are: m_h=7.2·m_0 (solid black), m_e=3.6·m_0 (solid grey),m_h=1.8·m_0 (dashed black).

In Fig. 3.11 (f), the shape of the FE curve is shown as a function of the excess energy E_{excess}. The used excess energies are (from right to left): 788 meV (solid gray), 87 meV (dashed black), 30 meV (solid grey), 15 meV (solid black). In the case of the simulations of experimental data, the change of the excess energy E_{excess} influences also the initial carrier densities. This happens, because the initial charge carrier density depends on the excitation intensity, on the absorption coefficient and both of them depend on the excess energy. The curves shown in Fig.3.11 (f), are calculated with fixed N_0.

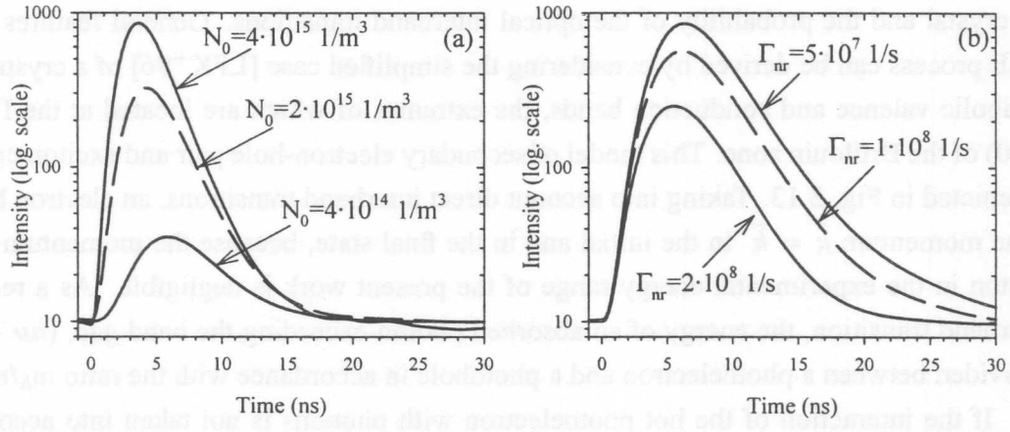

Figure 3.12: *Influence of the variation of the different parameters on the intensity of calculated FE decay curve: (a) initial carrier density N_0, (b) non-radiative losses Γ_{nr}. Intensities are not normalized.*

Fig. 3.12 shows, how the total intensity and the shape of the FE decay curve changes if initial carrier density and non-radiative losses are varied. Decay curves in Fig. 3.12 are not normalized and therefore intensity effects, discussed before, are directly visible. Varied values of parameters are shown in the figure and the fixed parameters are given in table 4.7.

This chapter revealed that the parameters N_0, $C_{exp} = E_d^2 m_e^{5/2}$ and Γ_{nr} most strongly affect the simulations. Therefore, only the influence of these parameters will considered while fitting the experimental data (see section 4.9). All other parameters were fixed during fitting of the experimental data. The effective electron and hole mass are not exactly known, but as it was shown in this chapter, limited knowledge about m_e and m_h does not influence significantly the shape of the decay curve.

3.6 Single-parabolic-branch band (SPBB) model of electron-electron scattering

Multiplication of electronic excitations (MEE) is a process where a primary electronic excitation (photoelectron and/or photohole) creates a secondary electronic excitation after an inelastic scattering event. This phenomenon has been observed as the creation of secondary electron-hole pairs in semiconductors by photoelectric methods [Sho61]. The luminescent analogue of this effect has been discovered in wide band-gap alkali halides where the doubling of the quantum yield of recombination and also excitonic luminescence has been observed at photon energies exceeding a certain threshold value [ILL65].

The distributions of photoelectrons and holes are determined by the band structure of the crystal and the probability of the optical interband transitions. General features of the MEE process can be derived by considering the simplified case [LFK+96] of a crystal with parabolic valence and conduction bands, the extremes of which are located at the Γ point ($\vec{k}$=0) of the Brillouin zone. This model of secondary electron-hole pair and exciton creation is depicted in Fig. 3.13. Taking into account direct interband transitions, an electron has the same momentum $\vec{k} = \vec{k}'$ in the initial and in the final state, because the momentum of the photon in the experimental energy range of the present work is negligible. As a result of interband transition, the energy of an absorbed photon exceeding the band gap, $(h\nu - E_g)$, is divided between a photoelectron and a photohole in accordance with the ratio m_h/m_e.

If the interaction of the hot photoelectron with phonons is not taken into account (it means that the process has to satisfy both the momentum and the energy conservation laws), then the threshold energy of the photon for the secondary electron-hole pair creation is given

$$h\nu_{th}^{e-h} = E_g + E_g \cdot \left(1 + 2\frac{m_e}{m_h}\right) \tag{3.46}$$

and the threshold for secondary exciton creation

$$h\nu_{th}^{ex} = E_g + E_{ex} \cdot \left(1 + 2\frac{m_e}{m_h}\right). \tag{3.47}$$

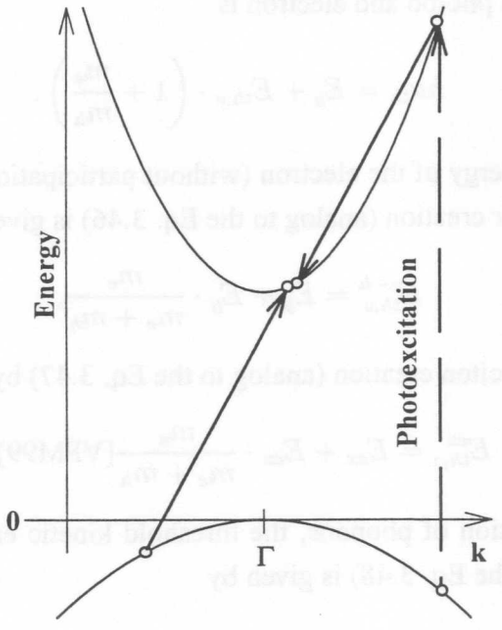

Figure 3.13: *A simplified model of the formation of secondary electron-hole pair via electron-electron scattering without participation of phonons. A dashed arrow shows the photoexcitation. The solid arrows depict electron-electron scattering.*

A simplified model of the formation of secondary electron-hole pairs without participation of phonons is shown in Fig. 3.13.

If the interaction of the hot photoelectron with phonons is taken into account (*i.e.* the threshold energy must satisfy only energy conservation but not any more momentum conservation, since phonons take over momentum), the threshold energy for the photon for secondary electron-hole creation is

$$h\nu_{th}^{e-h} = E_g + E_g \cdot \left(1 + \frac{m_e}{m_h}\right) \tag{3.48}$$

and for secondary exciton creation

$$h\nu_{th}^{ex} = E_g + E_{ex} \cdot \left(1 + \frac{m_e}{m_h}\right). \tag{3.49}$$

In the literature (for example [VFM99]), the threshold kinetic energy of the electron for secondary excitation creation ($E_{th,e}$) is often used. The zero-value of the kinetic energy of the electron is the bottom of the conduction band. Of course, the threshold kinetic energy of the electron is significantly smaller than the respective photon energy. The relation between

threshold energies of the photon and electron is

$$h\nu_{th} = E_g + E_{th,e} \cdot \left(1 + \frac{m_e}{m_h}\right). \tag{3.50}$$

The threshold kinetic energy of the electron (without participation of phonons) for the secondary electron-hole pair creation (analog to the Eq. 3.46) is given by

$$E_{th,e}^{e-h} = E_g + E_g \cdot \frac{m_e}{m_e + m_h}, \tag{3.51}$$

and for the secondary exciton creation (analog to the Eq. 3.47) by

$$E_{th,e}^{ex} = E_{ex} + E_{ex} \cdot \frac{m_e}{m_e + m_h} \text{[VFM99]}. \tag{3.52}$$

Including participation of phonons, the threshold kinetic energy of the electron-hole pair creation (analog to the Eq. 3.48) is given by

$$E_{th,e}^{e-h} = E_g, \tag{3.53}$$

and for the secondary exciton creation (analog to the Eq. 3.49) by

$$E_{th,e}^{ex} = E_{ex}. \tag{3.54}$$

Such small values are only possible because phonons take over the electron momentum.

The creation rates of secondary electron-hole pairs, $W_{e-h}(E_{kin})$, and of secondary excitons, $W_{ex}(E_{kin})$, depend on the kinetic energy of the electron in the following way [VFM99]:

$$W_{e-h}(E_{kin}) \sim \left(E_{kin} - E_{th,e}^{e-h}\right)^2, \tag{3.55}$$

$$W_{ex}(E_{kin}) \sim \sqrt{E_{kin} - E_{th,e}^{ex}}. \tag{3.56}$$

Hereby, the participation of phonons is neglected.

3.7 Multiple-parabolic-branch band (MPBB) model of electron-electron scattering

The 'classical' single-parabolic-branch band (SPBB) model describes transitions only within one parabolic band, while the multiple-parabolic-branch band (MPPB) model takes

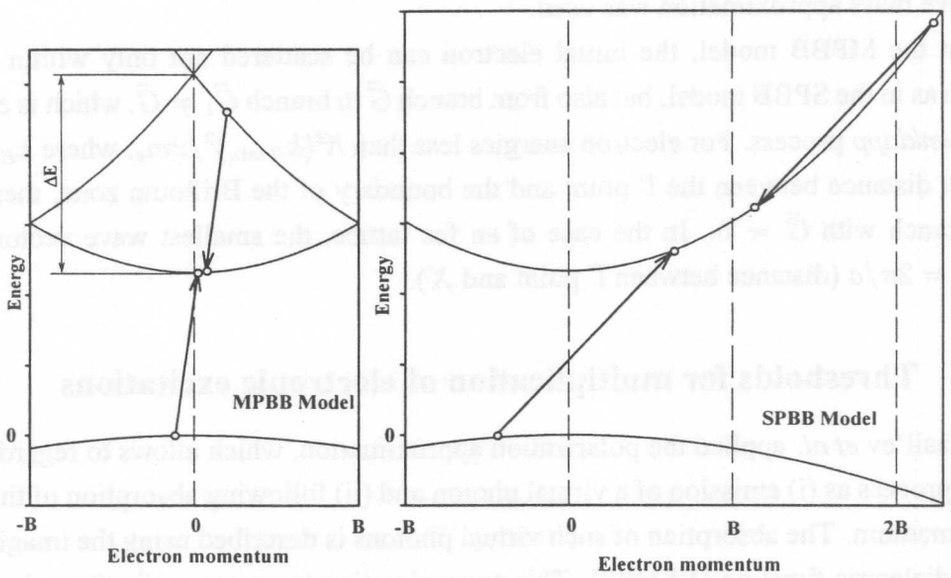

Figure 3.14: *Schematical presentation of the electron-electron scattering process in the multiple-parabolic-branch band model (the MPBB model, on the left) and in the single-parabolic-branch band model (the SPBB model, on the right). B marks a border of the first Brillouin zone.*

into account transitions between the different branches. Both models are schematically presented in Fig. 3.14. It turns out that the threshold energy for MEE is significantly lower in the case of MPBB than that of given by the SPBB model. Vasil'ev *et al.* recently presented analytic expressions for the threshold energies and the production rates of electron-hole pairs and excitons by electron impact in wide-gap insulators [VFM99]. Here, a short overview of the results by Vasil'ev *et al.* is given.

Vasil'ev *et al.* described the conduction band at energies about 10 eV above its bottom in first approximation as a set of free-electron parabolic bands with the effective mass (m_e) equal to the free electron mass (m_0). These bands are shifted in wave-vector space by vectors $\vec{G}$ which are a superposition of the primitive reciprocal lattice vectors $\vec{b}_i$ with integer coefficients:

$$\vec{G} = n_1\vec{b}_1 + n_2\vec{b}_2 + n_3\vec{b}_3. \tag{3.57}$$

The general form for the dispersion law of a conduction electron is then

$$E_e(\vec{k}) = \frac{\hbar^2\vec{k}^2}{2m_e}, \quad \vec{k} \in \Omega_\infty \quad \text{or} \quad E_e^{\vec{G}}(\vec{k}) = \frac{\hbar^2(\vec{k}-\vec{G})^2}{2m_e}, \quad \vec{k} \in \Omega_B, \tag{3.58}$$

where the energy origin is at the bottom of the conduction band, Ω_∞ means extended Brillouin zone and Ω_B the first Brillouin zone. For the holes in the valence band, the usual

effective mass approximation was used.

In the MPBB model, the initial electron can be scattered not only within the same branch as in the SPBB model, but also from branch $\vec{G}$ to branch $\vec{G}_1 \neq \vec{G}$, which is equivalent to an *umklapp* process. For electron energies less than $\hbar^2(k_{B\,\mathrm{min}})^2/2m_e$, where $k_{B\,\mathrm{min}}$ is the nearest distance between the Γ point and the boundary of the Brillouin zone, there is only one branch with $\vec{G} = 0$. In the case of an fcc lattice, the smallest wave vector value is $k_{B\,\mathrm{min}} = 2\pi/a$ (distance between Γ point and X).

3.7.1 Thresholds for multiplication of electronic excitations

Vasil'ev *et al.* applied the polarization approximation, which allows to regard the scattering process as (i) emission of a virtual photon and (ii) following absorption of this photon in the medium. The absorption of such virtual photons is described using the imaginary part of the dielectric function [VFM99]. This approximation is necessary for the calculation of production rates. Threshold energies are calculated from energy and momentum conservation laws.

The threshold for Q=0 (this corresponds to the threshold of the SPBB model, see Eq. 3.51 and Eq. 3.52) is

$$E_{th}^{0} = (1 + \Lambda)\, E_d\,, \tag{3.59}$$

where E_d=E_{ex} (for a secondary exciton creation) or E_d=E_g (for a secondary e-h pair creation), and $\Lambda = m_e/(m_e + m_h)$. Q=$\left|\vec{Q}\right|$=$\left|\vec{G}_1\text{-}\vec{G}\right|$ is the shift between the parabolic branches in reciprocal space. The free electron mass m_0 was used for electron effective mass m_e by Vasil'ev *et al.*

Differently from the SPBB model, the theory predicts two threshold values in the case of MPBB model (due to the transitions to the other branch of the band): the upper threshold is always larger than E_{th}^{0}, while the lower threshold can be significantly lower than E_{th}^{0}. The thresholds are given by

$$E_{th,Q}^{\pm} = E_{th}^{0} \pm 2\Lambda\sqrt{E_Q}\sqrt{(1 + \Lambda)\,(E_d + \Lambda E_Q)} + \Lambda\,(1 + 2\Lambda)\,E_Q\,, \tag{3.60}$$

where $E_Q = \hbar^2 Q^2/2m_e$.

For solid Kr, the lower thresholds (E_{th}^{-}) for different Q, calculated by Eq. 3.60 for FE and electron-hole productions are plotted in Fig. 3.15. The following parameters were used: lattice constant a=0.564601 nm, E_{ex}=10.13 eV, E_g=11.61 eV, $m_e = m_0$ and $m_h = 3.8 \cdot m_0$. The numbers in Fig. 3.15 and table 3.5 indicate the transitions taking place in different directions of wave-vector space. The calculated thresholds and other relevant parameters are

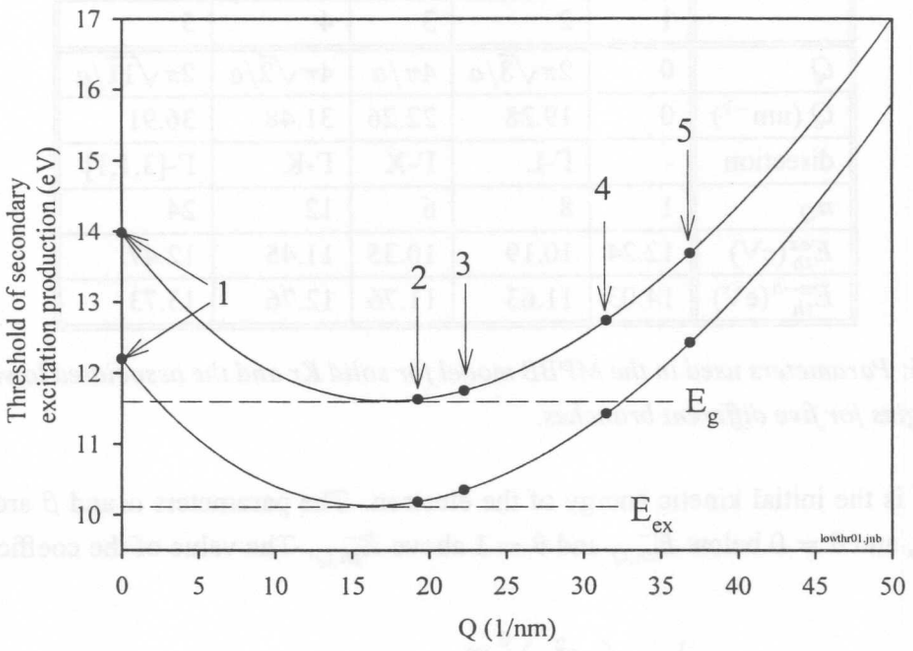

Figure 3.15: *The lower thresholds (E_{th}^{-}) for the electron kinetic energy in the case of impact production of a FE and an electron-hole pair as a function of Q for solid Kr. The solid lines show the mathematical solution for continous Q, the points show 'real' physically possible values for the discrete values of Q. Points marked with 1 correspond to the threshold values of the SPBB model.*

collected in table 3.5. The lowest kinetic energy for the exciton production is E_{th}^{ex} =10.19 eV in this approximation (Fig. 3.15, marked with 2).

The lowest threshold $E_{th,Q}^{-} = E_d$ can be achieved, if $\hbar Q = \sqrt{2m_e E_d}$. It would mean that E_d and ΔE (see Fig. 3.14) coincide. This would be an accidental coincidence because Q has only discrete values. Therefore, the minimal threshold value (point 2 in Fig. 3.15 and table 3.5) is slightly higher than E_d.

3.7.2 Production rates near thresholds

Vasil'ev's theory permits to estimate the production rates of secondary excitations. For $\vec{Q} \neq 0$, two thresholds (E_{th}^{-} and E_{th}^{+}) are well separated, and only E_{th}^{-} should be taken into account. In the case $\vec{Q} \neq 0$, the value of the production rate $W_Q(E)$ is given by

$$W_Q(E) = \frac{\beta}{\tau_0} \frac{(E_g - E_{ex})^{3-\alpha}}{|\varepsilon|^2 E_g E_{th,Q}^{-} \sqrt{E_Q E_{th,Q}^{-}}} \left[1 + \Lambda \sqrt{\frac{E_Q}{E_{th,Q}^{-}}}\right] \left(E - E_{th,Q}^{-}\right)^{\alpha} \theta\left(E - E_{th,Q}^{-}\right), \tag{3.61}$$

	1	2	3	4	5
Q	0	$2\pi\sqrt{3}/a$	$4\pi/a$	$4\pi\sqrt{2}/a$	$2\pi\sqrt{11}/a$
Q (nm^{-1})	0	19.28	22.26	31.48	36.91
direction	-	Γ-L	Γ-X	Γ-K	Γ-[3,1,1]
n_Q	1	8	6	12	24
E_{th}^{ex}(eV)	12.24	10.19	10.35	11.45	12.47
E_{th}^{e-h}(eV)	14.03	11.63	11.76	12.76	13.73

Table 3.5: *Parameters used in the MPBB model for solid Kr and the associated lower threshold energies for five different branches.*

where E is the initial kinetic energy of the electron. The parameters α and β are given in table 3.6, and $\theta = 0$ below $E_{th,Q}^{-}$ and $\theta = 1$ above $E_{th,Q}^{-}$. The value of the coefficient τ_0 is given by

$$\frac{1}{\tau_0} = \left(\frac{e^2}{4\pi\varepsilon_0}\right)^2 \frac{m_e}{\hbar^3} = 4.14 \cdot 10^{16}\ 1/s. \tag{3.62}$$

The formula for the impact production rate of secondary excitations for $\vec{Q} = 0$ (this is equivalent with the SPBB model) is

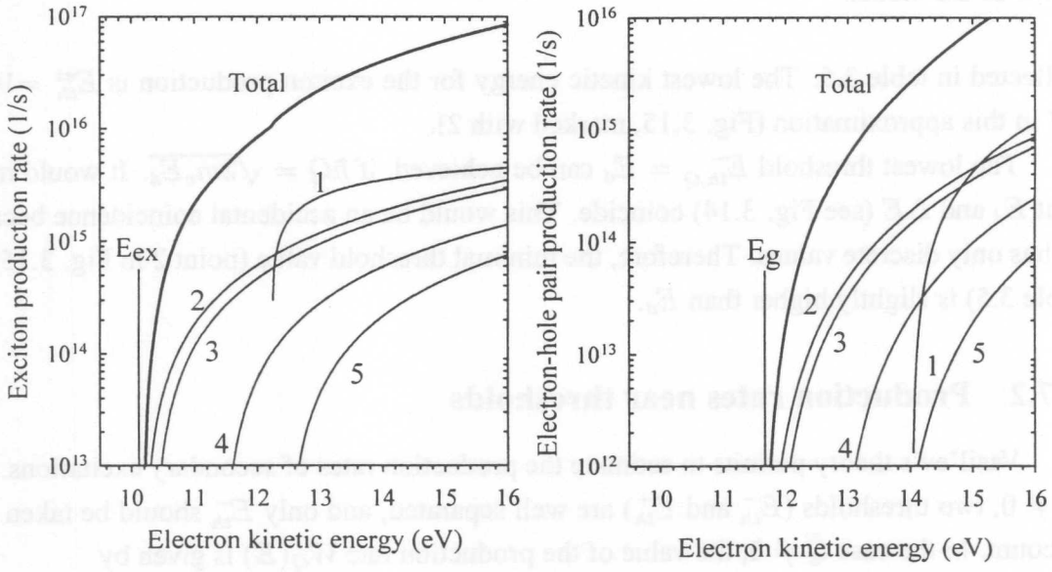

Figure 3.16: *The rates for impact production of FE and electron-hole pairs in solid krypton. Thin lines are the partial rates with the numbers indicating different branches. Total rates are depicted with thick lines.*

$$W_0(E) = \frac{\beta_0}{\tau_0} \frac{(E_g - E_{ex})^{2-\alpha_0}}{|\varepsilon|^2 E_g E} \left(E - E_{th}^0\right)^{\alpha_0}, \tag{3.63}$$

where E_{th}^0 is defined by Eq. 3.59 and the parameters α_0 and β_0 are given in table 3.6.

The experimental results can be compared with the total production rate, given by

$$W_e(E) = \sum_Q W_Q(E) = \sum_{|Q|} n_Q W_{|Q|}(E), \tag{3.64}$$

where n_Q is the number of nodes with the same $\left|\vec{Q}\right|$ in reciprocal space (given in table 3.5). The FE and electron-hole impact production rates at different $\left|\vec{Q}\right|$, as well as total rates, are plotted in Fig. 3.16. The rates, denoted by 1, correspond to the production rates of the SPBB model.

All calculations were made in the terms of electron kinetic energy and therefore are not directly comparable with photoexcitation experimental data. In the case of photoexcitation the situation is rather complicated due to the influence of the valence band. Therefore, the thresholds for photoexcitation are shifted to the higher energy side (see Eq. 3.50) and the rates are softer (it means values of α in Tab. 3.6 are smaller) [Vas00].

The SPBB model works well in the case of small wave vectors, *e.g.* for semiconductors. The wave vector of the electron, capable to create MEE in semiconductors, is significantly smaller than the distance between the Γ point and the boundary of the first Brillouin zone. If the initial kinetic energy of the electron is larger than $\hbar^2(k_{B,\min})^2/2m_e$, where $k_{B,\min}$ is the nearest distance between the Γ point and the boundary of the Brillouin zone, it is necessary to use the MPBB model, which includes also transitions between different branches. Nevertheless, in the case of wide-band dielectrics as solid Kr, the situation is even more complicated. It is well-known that at the boundary of the Brillouin zone parabolic bands are strongly deformed due to the periodic potential [Kit86]. It means that the SPBB and the MPBB model are applicable only as first approximations. For more accurate results, it is necessary to include the 'real' conduction band structure.

	α	β	α_0	β_0
n=1 exciton	1.5	$\frac{16(1-\Lambda)^{3/2}}{3\Lambda}$	0.5	$32(1-\Lambda)^{3/2}$
electron-hole pair	2.5	$\frac{16(1-\Lambda)^{3/2}}{15\Lambda(1+\Lambda)}$	1.5	$\frac{32(1-\Lambda)^{3/2}}{3(1+\Lambda)}$

Table 3.6: *Parameters in equations for production rate of secondary excitations.*

3.8 Electronic polaron complex

Besides direct photoexcitation and electron-electron scattering, one more possibility to create 'prompt' secondary excitons exists. This is a simultaneous creation of an exciton and an electron-hole pair (or two excitons) in an *one step process*. Such a concept was developed by Hermanson [Her69] and Devreese *et al.* [DKC72]. Hermanson discussed the possibility of the simultaneous production of two excitons by a single photon [Her69]. Devreese *et al.* analyzed the creation of the *electronic polaron complex* [DKC72]. In a simplified picture, this complex consists of an electron-hole pair created across the band gap and an exciton interacting with the electron-hole pair.

The interaction of a conduction band electron with the electronic polarization field of the crystal has been treated in various ways. An approach, developed by Toyozawa, replaces the many electron field of valence charges by a single dispersionless boson field consisting of excitons. As a result, a new quasiparticle was predicted - *an electronic polaron* - an electron surrounded with a cloud of virtual excitons [Her69]. The electronic polaron can be characterized with the electron-exciton coupling constant α and the semiclassical 'radius' of the electronic polaron R_{pol}. The formulas for α and R_{pol} have the form

$$\alpha = \frac{1}{8\pi\varepsilon_0}\left(1-\frac{1}{\varepsilon_\infty}\right)\frac{e^2}{R_{pol}}\frac{1}{E_{ex}} \text{ and} \tag{3.65}$$

$$R_{pol} = \sqrt{\frac{\hbar^2}{2m_e E_{ex}}} \text{ [Her69].} \tag{3.66}$$

Here, m_e is an effective electron mass in the conduction band, E_{ex} is the exciton energy, e is elementary charge, ε_0 is the dielectric constant, ε_∞ is the high-frequency dielectric constant of the medium, h is Planck's constant and $\hbar = h/2\pi$. Numerical values for α and R_{pol} are shown in table 3.7.

On the basis of electronic polaron theory, Hermanson's calculations [Her69] provide the ratio of transition probabilities for two and one exciton production by one photon

$$\frac{f^{(2)}}{f^{(1)}} = \frac{4\alpha R_{pol}}{a}\sigma. \tag{3.67}$$

Here, $f^{(2)}$ and $f^{(1)}$ are the probabilities for two- and one-exciton creation, a is the lattice constant, σ is the electronic factor. The electronic factor depends mainly on the exciton radius and the average 'radius' $2\pi/a$ of the Brillouin zone. Its value is presented by a complicated formula [Her69]. The quantitative values on the basis Eq. 3.67 are collected for solid Ne, Ar [Gmi00], Xe [Ste99] and Kr in table 3.7. As table 3.7 shows, the probability for

	E_{ex} (eV)	α	R_{pol} (Å)	$\frac{f^{(2)}}{f^{(1)}}$ (%)	Reference
Ne	17.36	0.16	0.51		[Gmi00]
Ar	12.06	0.29	0.81	3.2	[Gmi00]
Kr	10.13	0.35	0.95	4.9	present work
Xe	8.36	0.41	1.1	10.2	[Ste99]

Table 3.7: *The n=1 exciton energy, the electron-exciton coupling constant α, the semiclassical 'radius' of the electronic polaron R_{pol} and the ratio of transition probabilities for the two and one exciton production by one photon in RGS.*

the simultaneous production of two excitons by one photon is surprisingly high. However, it is important to note that Hermanson's approach overestimate the production rate of the double excitation [Her69].

Differently from the *electronic polaron* (*i.e.*, an electron dressed by a cloud of virtual excitons), *an electronic polaron complex* consists of an electron-hole pair plus an exciton interacting with each other. The electronic polaron complex is either 'free' or 'bound' to the hole in the valence band. For the 'free' electronic polaron complex with relatively small α ($\alpha < 1$), a threshold for optical excitation was predicted to be

$$h\nu_{th}^{free} = E_g + E_{ex}. \tag{3.68}$$

The probability for the creation of the 'free' electronic polaron complex has a maximum at certain energy and thereafter it slowly decreases. The location of the maximum for the 'free' electronic polaron complex depends on the experimental technique in use and it is expected at

$$h\nu_{\max}^{free} = E_g + 1.20 \cdot E_{ex} \text{ in absorption and} \tag{3.69}$$

$$E_{\max}^{free} = E_g + 1.25 \cdot E_{ex} \text{ in energy loss spectroscopy.} \tag{3.70}$$

For the 'bound' electronic polaron complex, a threshold for optical excitation is predicted at

$$\hbar\nu_{th}^{bound} = 2 \cdot E_{ex}. \tag{3.71}$$

Chapter 4

Experimental results and discussion

The experimental results of this work are presented in 'historical' sequence as RGS have been studied in the past. First of all, some new aspects of luminescence spectra and reflection spectra of solid krypton will be discussed. The most important and original results of the present work, decay curves and time-resolved excitation spectra for FE and STE of solid Kr, will be presented afterwards. The author of this thesis hopes, that such a sequence permits also better understanding for the reader, who is not very familiar with luminescence of RGS.

4.1 Luminescence of solid krypton

Kr crystals, like solid Xe, exhibit simultaneously strong broad-band self-trapped exciton (STE) luminescence as well as considerable narrow-band luminescence of free excitons (FE). The first observation of FE luminescence in solid Kr was reported by Bonnot *et al.* [BBC+74]. Since FE luminescence is observed only in samples with very good 'quality' (*i.e.* homogeneous sample with relatively big crystallites, very small amount of impurity and as grown defects), it makes spectroscopic investigations of FE luminescence experimentally rather complicated. Nevertheless, several papers are available about FE luminescence in solid Xe [KS79, VBF+93, Fug88, Ste99]. Less information is published about FE luminescence in solid Kr [VBF+93, Var94, Klo89]. Lack of data about FE luminescence in solid Kr is partially caused by the purity of Kr gas used. Namely, commercially available Kr gas is always unintentionally doped with a certain amount of the isoelectronic Xe impurity, and Xe atoms in a Kr matrix are extremely good luminescence centers. Some tens of ppm Xe in Kr cause strong Xe luminescence, suppressing significantly the FE luminescence of solid Kr. The intensity of the FE line in a luminescence spectrum is very sensitive to the 'quality' of the sample, since FE emission exists only in samples with good crystal structure and

small amount of defects. Therefore the ratio of FE and STE intensity is used as a measure of sample 'quality' [VBF+93].

Figure 4.1 (a) shows a typical luminescence spectrum of 'good quality' krypton sample. This sample is grown from Kr gas with the highest purity commercially available (*Spectra Gases*, 99.999 % Kr, Xe less than 5.0 ppm). Broad-band luminescence in the region of 8.6 eV is assigned to the STE emission and a narrow peak at E_{ex}=10.14 eV is due to the FE luminescence. At the low energy side of FE, a phonon-caused satellite is located. A small peculiarity at the higher energy side of FE is most probably an experimental artefact caused by the VUV-2 monochromator.

Figure 4.1 (b) demonstrates a typical luminescence spectrum of solid krypton with some Xe impurity. The spectrum is more complicated due to the Xe impurity which causes clearly observable emission bands at 9.65 and 9.69 eV. The additional bands in the region 6.7 ... 8.4 eV, which overlap with the STE band of Kr, originate as well from $(KrXe)^*$ and Xe_2^* molecular centres [VBF+93, SOGG94].

4.2 STE luminescence of solid krypton

The STE luminescence of solid Kr is well known and has been studied several times by many groups [Var94, KKK+97, SOGG94]. Nevertheless, the maximum and width of the STE emission band reported in the literature vary significantly. A collection of experimental data (the peak maxima and widths) for STE band is shown in table 4.1. Experiments of the present work clarified that mainly two factors induce such big variations - the amount of Xe impurity and the 'quality' of the sample (*i.e.* existence of a macroscopic crystal structure). The Xe impurity causes the appearance of new Xe-connected emission bands and some of these overlap with STE luminescence band, complicating the analysis. As a result, the experimentally detected luminescence band shifts to the high-energy side and its shape also changes (see Fig. 4.1). In contrary, the crystal defects induce a red shift of the STE luminescence band. The characteristics of the STE band obtained from experiments in present work and earlier studies [FBYS86, KKK+97] are collected in table 4.1. Varding *et al.* [Var94] had Kr samples with a noticeable amount of Xe impurity. Therefore they decomposed the experimentally observed broad luminescence band using mathematical methods into the different sub-bands. However, such a method is sensitive to the initial parameters and depends also on the exact fitting procedure. The Kharkov group also used decomposition into sub-bands [SOGG94]. They investigated the red shift of the luminescence band during irradiation of the sample assuming that the STE band is a sum of two gaussian sub-bands: STE at a 'perfect crystal site' and STE associated with a defect [SOGG94, FSOG93]. In their inter-

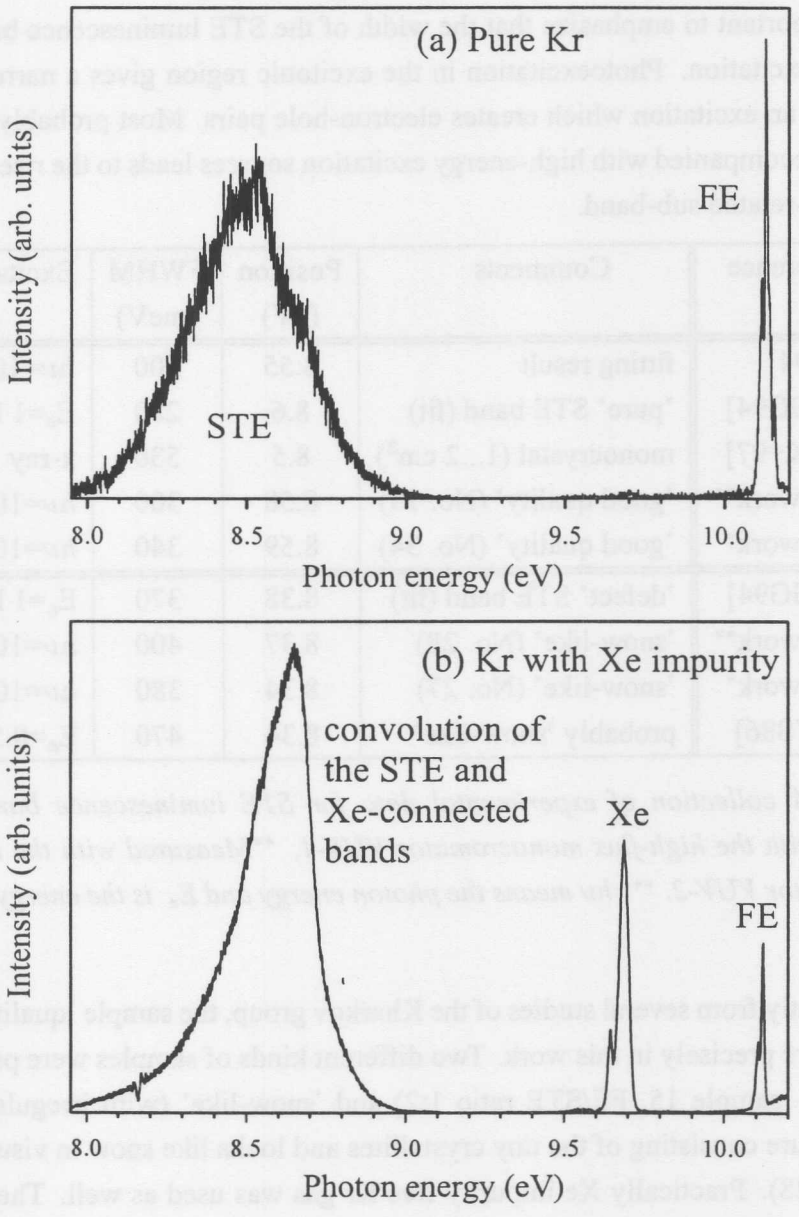

Figure 4.1: *(a) Luminescence spectrum of 'good quality' Kr sample (sample16, purity of the gas 99.999 %, less than 5 ppm Xe). (b) Luminescence spectrum of solid Kr with Xe impurity (sample 12). Both spectra were excited by 10.42 eV photons at 6 K and measured with the high-resolution VUV-2 monochromator (resolution $\Delta\lambda$=1.1 Å).*

pretation, the red shift is due to the increase of the intensity of the STE luminescence band near crystal defects. The Kharkov group considered only effects of the sample structure, but ignored the role of Xe-impurity at the high energy side of the STE.

It is important to emphasize that the width of the STE luminescence band depends on the type of excitation. Photoexcitation in the excitonic region gives a narrower STE band compared to an excitation which creates electron-hole pairs. Most probably, an increase of the defects accompanied with high-energy excitation sources leads to the rise of the intensity of the defect-related sub-band.

Reference	Comments	Position (eV)	FWHM (meV)	Excitation***
[Var94]	fitting result	8.55	200	$h\nu$=10.42 eV
[SOGG94]	'pure' STE band (fit)	8.6	280	E_e=1 keV
[KKK+97]	monocrystal (1...2 cm^3)	8.5	530	x-ray
This work**	'good quality' (No. 15)	8.58	300	$h\nu$=10.42 eV
This work*	'good quality' (No. 34)	8.59	340	$h\nu$=10.60 eV
[SOGG94]	'defect' STE band (fit)	8.38	370	E_e=1 keV
This work**	'snow-like' (No. 28)	8.37	400	$h\nu$=10.42 eV
This work*	'snow-like' (No. 27)	8.34	380	$h\nu$=10.42 eV
[FBYS86]	probably 'snow-like'	8.34	470	E_e=0.5 keV

Table 4.1: *A collection of experimental data for STE luminescence band of solid Kr. *Measured with the high-flux monocromator VUV-1. **Measured with the high-resolution monochromator VUV-2. *** $h\nu$ means the photon energy and E_e is the energy of the electron beam.*

Differently from several studies of the Kharkov group, the sample 'quality' effects were observed more precisely in this work. Two different kinds of samples were prepared - 'good quality' (*e.g.* sample 15, FE/STE ratio 1:2) and 'snow-like' (with irregular macroscopic crystal structure consisting of the tiny crystallites and looks like snow in visual observation, *e.g.* sample 28). Practically Xe impurity free Kr gas was used as well. The STE luminescence for both kinds of samples was measured under similar conditions. The STE emission bands of these samples are depicted in figure 4.2. In the 'snow-like' sample the STE luminescence band can be represented with only one, but rather broad gaussian. Perturbed STE in a 'snow-like' sample can occupy several sites with different microscopic neighbourhood. The distribution of these sites with different local geometry for the perturbed STE can be responsible for the broad gaussian-shape luminescence band. However, the situation with a 'good quality' sample is also not perfect, because the structure of a real crystal is

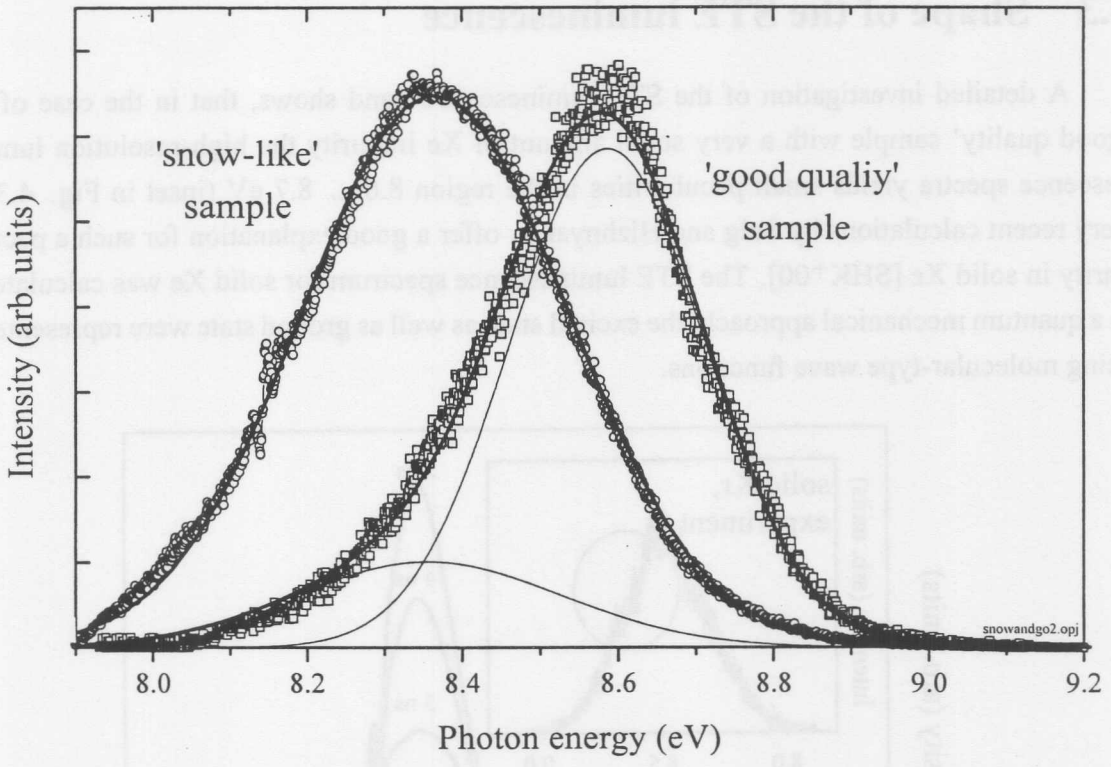

Figure 4.2: *Time-integrated STE luminescence spectra for a 'snow-like' sample (sample 28) and a 'good quality' sample (sample 15, FE:STE peak-to-peak ratio 1:2), excited by 10.42 eV photons. A decomposition into two gaussians is also shown for 'good quality' sample.*

never defect free. The luminescence band of a 'good quality' sample includes beside the STE luminescence at perfect surrounding also some contribution from the STE near defects. Taking into account the maximum and the width of the 'defect' luminescence band from a 'snow-like' sample, it is possible to separate this small 'defect' part ($\sim$10 per cent from the integral band intensity in sample 28, see Fig. 4.2). As a result, the position of the maximum and width of the STE band in a 'good quality' sample was determined with higher precision.

Numerical values for the location of the maximum and width of the luminescence band obtained in this work are given in table 4.1. For the first time, it is clearly demonstrated, that the STE luminescence band near defects is shifted $\sim$0.25 eV to the lower energy side and it is also broader than the emission band of STE in the perfect lattice. Results of the present work are practically free from an uncertainty caused by the two gaussian fit of the broad luminescence band with not well defined initial parameters. Due to the especially purchased high-purity Kr, the present work is not suffering from the disturbances induced by Xe impurity.

4.3 Shape of the STE luminescence

A detailed investigation of the STE luminescence band shows, that in the case of a 'good quality' sample with a very small amount of Xe impurity the high-resolution luminescence spectra yields small peculiarities in the region 8.6 ... 8.7 eV (inset in Fig. 4.3). Very recent calculations by Selg and Hizhnyakov offer a good explanation for such a peculiarity in solid Xe [SHK+00]. The STE luminescence spectrum for solid Xe was calculated in a quantum mechanical approach, the excited state as well as ground state were represented using molecular-type wave functions.

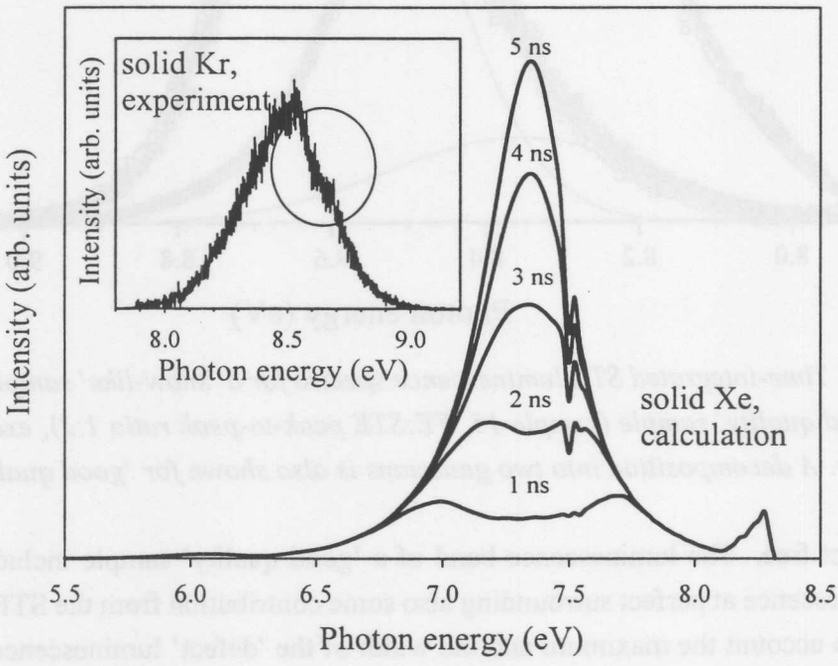

Figure 4.3: *Calculated time-evolution of the spectral shape of the singlet component of the STE luminescence in solid xenon [SHK+00]. Different curves show the evolution of luminescence between excitation at t=0 ns and time t, indicated by a number above the respective curve. Inset: A high-resolution time-integrated luminescence spectrum of the STE in solid Kr, excited by 10.42 eV photons.*

Fig. 4.3 depicts calculated luminescence spectra for the singlet component of the STE luminescence in solid xenon at various time-moments after excitation. A delta-function like excitation at time zero to the highest vibration levels of Xe_2^* center just below FE energy was assumed. Different curves in Fig. 4.3 represent the successive evolution of luminescence after each ns. As it is clearly demonstrated in Fig. 4.3, a peculiarity at 7.5 eV exists in the emission spectrum. Detailed calculations assigned this peculiarity to transitions from the lowest vibrational levels n=0,1,2... of the excited state to the ground state [SHK+00].

Such effects can occur also in solid Kr, but with slightly different shape, due to the different potential curves. Therefore, the observed peculiarity in solid Kr (inset in Fig. 4.3) has most likely the same origin as shown by calculation for solid Xe. The peculiarity in the emission spectra of solid Kr is less pronounced than in calculated emission spectra, since time-integrated luminescence spectra include besides the STE singlet component also emission from the long-living triplet state. The peculiarity at 8.6 ... 8.7 eV is also to a certain extent sample-sensitive and not well-pronounced in all samples.

Another possibility has to be considered as well. Namely, the peculiarity at 8.6 ... 8.7 eV can be connected with sensitivity variation of the VUV sensitive PSD at different wavelengths. Therefore, the problem needs additional high-resolution time-resolved investigations.

4.4 Reflection spectra

Reflection spectra of solid Kr have been measured several times by different groups in the past, for example: Haensel *et al.* [HKK$^+$70] and Saile [Sai76, Sai80]. Most problems in reflectivity measurements of RGS are connected with sample 'quality'. The structure of the sample and particularly of its surface, the thickness and the temperature of the sample, surface contamination, *etc.* can seriously influence reflectivity. The 'quality' of the samples prepared in this work is significantly improved as compared with earlier studies. Also vacuum conditions, especially important for reflection measurements, were considerably better. Therefore, beside luminescence measurements, also new high-resolution reflection measurements were performed during this work. These data permit to determine more accurate several values of exciton characteristics in solid krypton. Also some new aspects of the exciton-polariton nature of the n=1 and n'=1 excitons will be discussed on the basis of new high-resolution reflection data in this section.

Fig. 4.4 depicts a typical reflection spectrum of solid krypton. This spectrum was measured from sample 25 using the Pt grating with a resolution $\Delta\lambda$=2.2 Å. In this figure, both exciton series and the position of the band gap are denoted by arrows. The members of the $\Gamma(\frac{3}{2})$ exciton series are marked with n=1,2,3,4 and the members of the spin-orbit splited $\Gamma(\frac{1}{2})$ series with n'=1,2,3. It is important to note, that n=1 and n'=1 mark transversal excitons and L and L' respective longitudinal excitons. Surface exciton is designated with s. The same notation is used also henceforth. The position of the n=1 exciton is taken from the high-resolution luminescence measurements [Var94]. Detection of the exact position of n'=1 exciton, as well as longitudinal excitons L and L' is not trivial. Therefore, the energetic positions of the n'=1, L and L' in Fig. 4.4 are estimates.

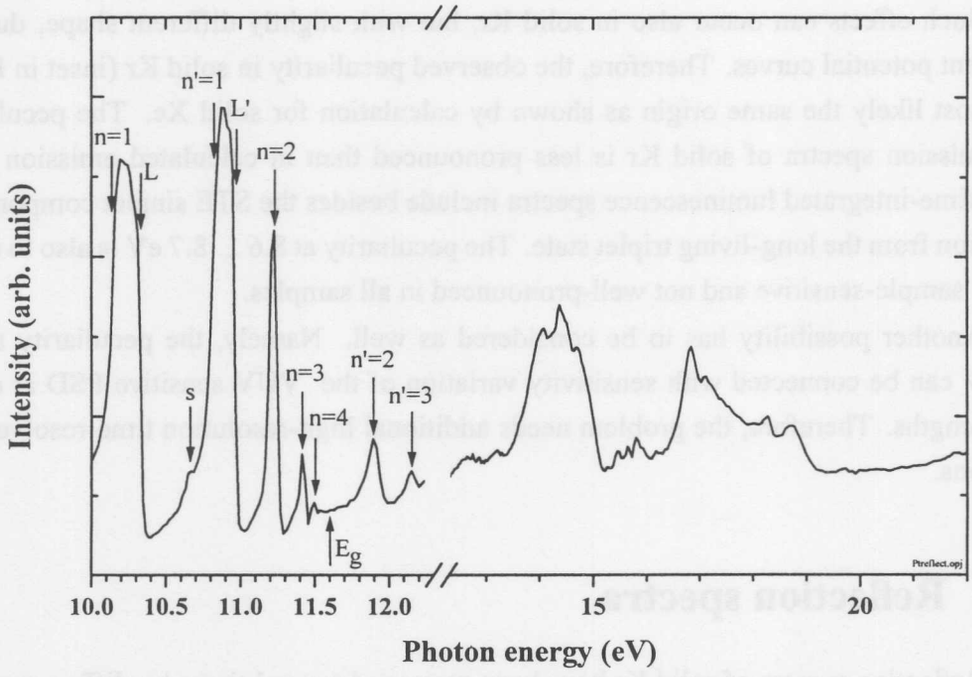

Figure 4.4: *Reflection spectrum of solid Kr (sample 25, T=6 K), measured with the Pt grating ($\Delta\lambda$=2.2 Å). The position of the n=1 exciton is taken from the high-resolution luminescence measurements [Var94], positions of the n'=1, L and L' are estimates.*

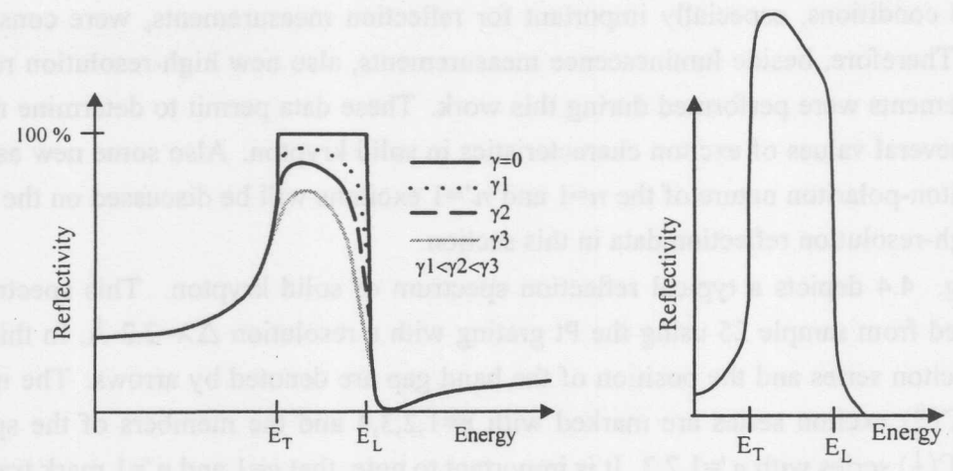

Figure 4.5: *Calculated reflectivity curves for the exciton-polariton. On the left: the simplest exciton-polariton model neglecting the dispersion of the exciton [Kli95]. On the right: a model calculation including exciton dispersion for the special case of the n=1 exciton in solid Xe [KS79]. E_L means energy of the longitudinal exciton and E_T is energy of the transversal exciton.*

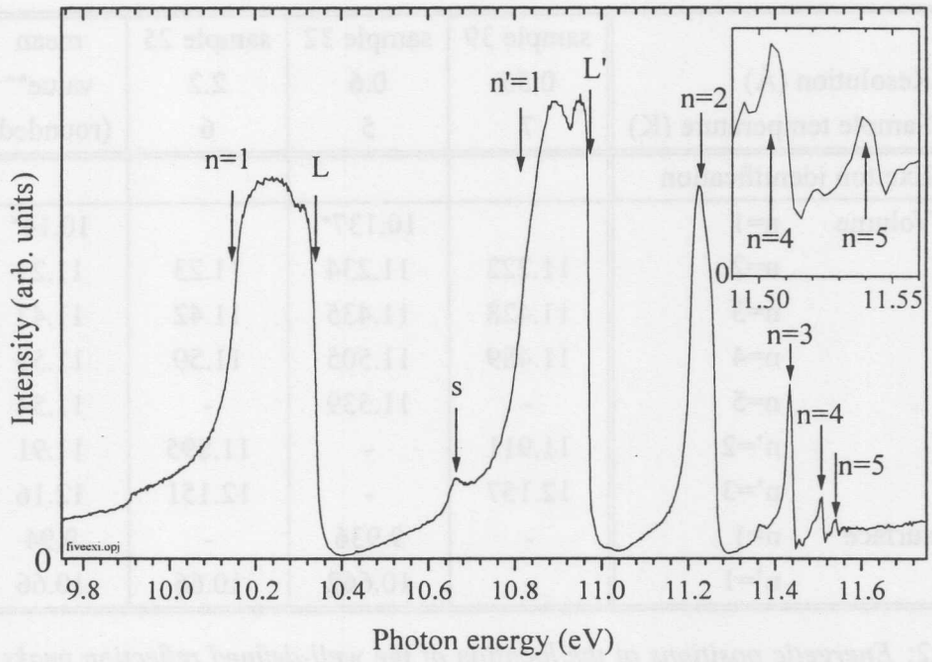

Figure 4.6: *High-resolution reflection spectrum of solid Kr (sample 32, T=6 K), measured with Al grating ($\Delta\lambda$=0.6 Å). The inset shows n=4 and n=5 excitons in large scale. For the first time, the n=5 exciton was observed.*

Differently from the sharp maxima of $n\geq 2$ and $n'\geq 2$ excitons, the reflection peaks of the $n=1$ and $n'=1$ excitons are significantly broadened. This happens due to the well-known transversal-longitudinal splitting, discussed in earlier papers [KS79, FGS82, Zim87]. Fig. 4.5 shows the results from two model calculations for the line-shape of reflection peak of exciton-polariton. The reflectivity, shown on the left, is calculated for the simplest exciton-polariton model neglecting the dispersion of the exciton. The situations without damping (γ=0) and with 3 different damping coefficients ($\gamma_1<\gamma_2<\gamma_3$) [Kli95] are shown. A result of a model calculation by Kink and Selg for the solid Xe n=1 exciton (including exciton dispersion) is demonstrated on the right [KS79]. As Fig. 4.5 demonstrates, it is difficult to find exact energetic positions of the transversal (n=1, n'=1) and longitudinal excitons (L and L') directly from the reflection spectra. In principle, more accurate values from the rather complicated model calculations can be obtained [KS79].

Reflection spectra with both, aluminium and platinum grating were measured during this work. The aluminium grating offers higher intensity of incident light in the spectral region below ~15 eV and has practically no usable intensity above ~20 eV (see Fig. 2.2). Therefore, for solid Kr the aluminium grating offers unique possibility to work almost without higher diffraction orders of exciting light. Fig. 4.6 presents a high-resolution reflection spectrum of the exciton region. This spectrum was recorded with the aluminium grating

		sample 39	sample 32	sample 25	mean
Resolution (Å)		0.55	0.6	2.2	value**
Sample temperature (K)		7	5	6	(rounded)
Exciton identification					
Volume	n=1		10.137*		10.14*
	n=2	11.222	11.234	11.23	11.23
	n=3	11.428	11.435	11.42	11.43
	n=4	11.489	11.505	11.50	11.50
	n=5	-	11.539	-	11.54
	n'=2	11.911	-	11.895	11.91
	n'=3	12.157	-	12.151	12.16
surface	n=1	-	9.936	-	9.94
	n'=1	-	10.662	10.66	10.66

Table 4.2: *Energetic positions of the location of the well-defined reflection peaks for three different sample and mean values. Due to the longitudinal-transverse splitting, 'exact' positions of the n'=1, L and L' can not be directly determined from the experiment and are therefore missing here. *Energy of the n=1 exciton stems from the luminescence measurements [Var94]. **Error of the mean values is predicted to be 10 meV or smaller.*

(sample 32, resolution $\Delta\lambda$=0.6 Å). The well pronounced n=5 member of the Wannier series is observed for the first time. The observation of a new member of the exciton series was possible due to the high sample 'quality' and very good vacuum conditions at the SUPERLUMI set-up.

The positions of well-defined reflection peaks from three different samples and mean values are collected in table 4.2. As stated above, it is not possible to find the particular values for the n'=1, L and L' directly from the reflection spectra and therefore their positions are excluded from table 4.2. The estimated error of mean values is not more than 10 meV.

According to theory, the excitons with main quantum number $n\geq 2$ are Wannier-type excitons (energy given with Eq. 3.5). The n=1 exciton is classified as 'intermediate exciton' [Zim87]. One reason is that the n=1 exciton energy, determined from the reflection spectrum, can not represented as a member of the Wannier series.

But energy of the n=1 exciton can be taken from the luminescence measurement and $n\geq 2$ exciton energies from the reflectivity measurement. In such a case, plotting these energetic positions as a function of $1/n^2$, it is shown, that all members of the series can be described by the Wannier formula (Eq. 3.5). An analogous result is also valid for solid Xe

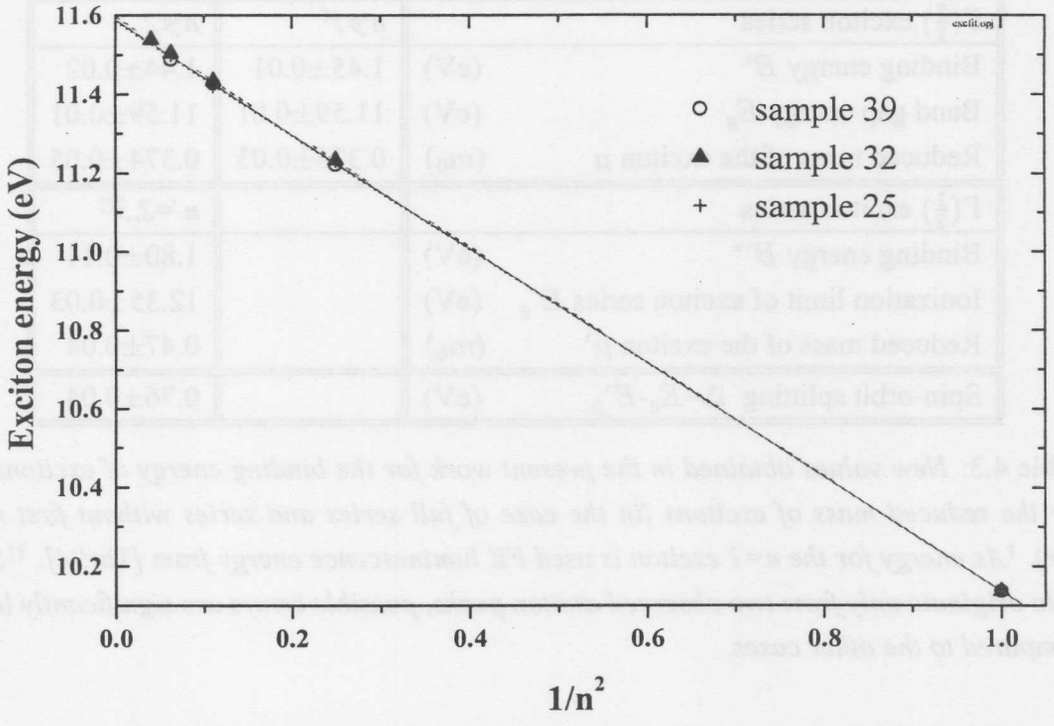

Figure 4.7: *Exciton energies of the* $\Gamma(\frac{3}{2})$ *series as a function of* $1/n^2$ *for data from three different samples. A linear regression is shown as well.*

[Ste99]. At first sight, the new result excludes a need for (at least for the heavy RGS like Xe and Kr) all theories developed to explain the deviation of the energetic position of the n=1 exciton from the Wannier model. Nevertheless, the Wannier radius of n=1 excitons is smaller than the distance between nearest neighbours in all RGS (in solid Kr, Wannier radius is 2.65 Å and n.n. distance is 3.98 Å, respectively) and therefore the exclusion of the 'intermediate exciton' model has to be taken with care.

A graphical presentation of the exciton energies versus $1/n^2$ permits to find the binding energy B^* of the Wannier exciton and the band gap energy E_g using a simple linear regression. Such a linear regression for data from 3 different samples is shown in Fig. 4.7. In this figure, the energy of the n=1 exciton is taken from luminescence experiment [Var94] and energies of the $n\geq 2$ excitons from reflection measurements. The numerical results of the linear regression are presented in table 4.3. There are also results of the linear fit without and including the n=1 exciton. Results are very similar in both cases. The reduced mass of the exciton μ can be calculated from the exciton binding energy B^*. The reduced mass is given by (SI system)

$$\mu = B^* \frac{8\varepsilon_r^2 \varepsilon_o^2 h^2}{e^4}, \tag{4.1}$$

$\Gamma(\frac{3}{2})$ exciton series		$n\geqslant 1^{\dagger}$	$n\geqslant 2$
Binding energy B^*	(eV)	1.45±0.01	1.44±0.02
Band gap energy E_g	(eV)	11.59±0.01	11.59±0.01
Reduced mass of the exciton μ	(m_0)	0.376±0.03	0.374±0.05
$\Gamma(\frac{1}{2})$ exciton series			$n'=2,3^{\dagger\dagger}$
Binding energy B'^*	(eV)		1.80±0.14
Ionization limit of exciton series E'_g	(eV)		12.35±0.03
Reduced mass of the exciton μ'	(m_0)		0.47±0.04
Spin-orbit splitting $\Delta=E_g-E'_g$	(eV)		0.76±0.04

Table 4.3: *New values obtained in the present work for the binding energy of excitons and for the reduced mass of excitons (in the case of full series and series without first member).* †*As energy for the n=1 exciton is used FE luminescence energy from [Var94].* ††*Since data originate only from two observed exciton peaks, possible errors are significantly larger compared to the other cases.*

where h is the Planck's constant, e is the elementary charge, ε_0 is the dielectric constant and ε_r is the dielectric permittivity of the medium. After inserting the physical constants, the expression for the value of the reduced mass μ is

$$\mu[m_0] = B^*[eV] \cdot \varepsilon_r^2 \cdot 0.0734, \tag{4.2}$$

where B^* is expressed in eV, μ in free electron mass and ε_r=1.88 for solid krypton. Since the ε_r is not a fundamental constant and the different values are used for ε_r in the literature, it is not included into the numerical constant in Eq. 4.2. From the reduced mass μ of exciton it is also possible to estimate the exciton radii (see Eq. 3.6). A reduced mass value μ=(0.376±0.03)·m_0 gives a radius for the n=1 exciton 2.65±0.03 Å, which is smaller than the distance between nearest neighbours in Kr lattice (3.98 Å). The calculated radius for the n=2 exciton is 10.6±0.1 Å. However, the error bars for the radii of excitons (especially for the n=1 exciton) are probably underestimated due to the restrictions of the Wannier model.

The binding energy B^*' and reduced mass μ' for $\Gamma(\frac{1}{2})$ excitons were analogously calculated from the reflection data of $\Gamma(\frac{1}{2})$ exciton series. The difference between E_g and E'_g gives a value for spin-orbit splitting Δ (see table 4.3). In the case of the free Kr atom, the spin-orbit splitting is 0.67 eV [SKJ85].

Some values of the binding energy and reduced mass of the excitons for solid krypton from literature as well results of this work are presented in table 4.4. The data of this work, measured with very good spectral resolution, are a good basis for obtaining high precision

Reference		[Bal62]	[Rös70]	[Sai76]	Present work
Method		absorption	theory	absorption	reflection
Temperature	(K)	40			6
B^*	(eV)	1.73		1.53	1.44±0.02
E_g	(eV)	11.67	11.67	11.61	11.59±0.01
μ	m_0	0.41*	0.42	0.40	0.376±0.05
B'^*	(eV)	1.52**		2.09***	1.80±0.14***
E'_g	(eV)	12.33**	12.37	12.44***	12.35±0.03***
μ'	m_0	0.36*		0.54	0.47±0.04
$\Delta=E'_g-E_g$	(eV)	0.66	0.70	0.83	0.76±0.04

Table 4.4: *A collection of the parameters for exciton series in solid Kr from literature. Results of the present work are also shown. *Baldini used value ε_r=1.80. **On the basis of n'=1 and n'=2 excitons. ***On the basis of n'=2 and n'=3 excitons.*

values of exciton parameters. Therefore, it is reasonable to assume that these values are more reliable compared to the earlier studies, known from the literature.

The uncertainty of the peak positions due to the primary monochromator is a sum of two components: (i) the resolution of the monochromator (ii) the nonlinearity of the monochromator. The best resolution of the primary monochromator was 0.6 Å, *i.e.* ~6 meV at 11 eV (in the middle of the excitonic region). The nonlinearity of the monochromator was estimated to be 0.2 Å [Run97], *i.e.* ~2 meV at 11 eV. Therefore, for high-resolution reflection measurements, the error due to the primary monochromator is less than 10 meV. Additionally, exciton peaks in the reflection spectra have also a natural shape obstructing a precise determination of the peak positions. Errors for the calculated quantities (B^*, E_g, μ) were estimated on the basis of the least square method.

It is possible to calculate effective masses for the electron and hole (m_e and m_h) from the reduced exciton mass μ, determined experimentally. This is by far not trivial, since the reduced mass μ gives only one relation between the electron and the hole effective mass. Hence, either the m_e or m_h is necessary to be known. Two additional complications also exist. Firstly, it is expected that the hole effective mass m_h^* is anisotropic leading to the anisotropic reduced mass of the exciton μ [Rat96, KM73]. Secondly, it is predicted that there are two different kinds of holes: light (m_h=1.21·m_0, in the direction $\Gamma \longrightarrow \Delta \longrightarrow X$ of Brillouin zone) and heavy (m_h^*=7.66·m_0, also $\Gamma \longrightarrow \Delta \longrightarrow X$) holes [KM73]. However, notwithstanding theoretical considerations such a effects are not observable neither in the reflection nor in the luminescence spectra. Therefore, the anisotropy can be ignored and the

Author(s)	Reference	m_e (m_0)
Fowler	[Fow63]	0.60
Rössler	[Rös70]	0.42
Kunz and Mickish	[KM73]	0.418
Ratner	[Rat96]	0.71
Plenkewicz *et al.* (in liquid)[1]	[PFPJ91]	0.45
Bader *et al.* (experimental)[2]	[BPCS84]	1.1

Table 4.5: *A collection of theoretically estimated effective electron masses for solid Kr.* [1]*Near triple point.* [2]*This experimental value is applicable for higher conduction band states, not for the bottom of the conduction band.*

mean isotropic values for the m_h and μ are used.

No experimental value for the effective electron mass near the bottom of the conduction band has been determined. Only several theoretical estimates are available, collected in table 4.5. Bader *et al.* reported the experimental value m_e^*=1.1·m_0 (m_0 is free electron mass)[BPCS84], found on the basis of low-energy electron transmission data. Unfortunately this method gives a value for the higher conduction band states. Since the value of effective electron mass is more reliable than the estimates for effective hole mass m_h, the effective electron mass m_e=0.42·m_0 is used as a known quantity in this work. Such a value of m_e was introduced by Rössler [Rös70] and it is also in good agreement with calculations by Kunz and Mickish (m_e=0.418±0.001) [KM73]. Taking m_e=0.42·m_0 and μ=0.376·m_0 (table 4.3), then the calculated value for the effective hole mass is m_h=3.59·m_0.

The width of the exciton band can be estimated on the basis of the effective masses of electrons and holes. In the simple parabolic band approximation, the width of the exciton band equals to

$$2B = \frac{\hbar^2 k_{\max}^2}{2m_{ex}^*}, \tag{4.3}$$

where B is the half-width of the exciton band, $k_{\max}$ the maximal value of the wave vector in the first Brillouin zone and m_{ex} the effective mass of an exciton. For solid Kr, $m_{ex} = m_e + m_h$=(0.42+3.59)·m_0=4.01·m_0. The maximal value for the wave vector $k_{\max}$ for fcc lattice is $\frac{\pi}{a}\sqrt{5}$, *i.e.* distance between Γ(0,0,0) and W($\frac{\pi}{a}$, 0, $\frac{2\pi}{a}$) points in the first Brillouin zone. On the basis of such data, the half-width of exciton band equals to B=0.37 eV, which seems to be more reliable than the widely used literature value B=0.45 eV estimated with a similar method [Fug78].

Temperature dependence

Reflection spectra measured at different temperatures (from 7 to 37 K) are shown in Fig. 4.8 (sample 39, $\Delta\lambda$=0.55 Å). The peak positions for well-defined sharp exciton maxima are listed in table 4.6. As discussed before, positions of the n'=1, L and L' can not directly be determined from the reflection spectra and therefore are missing here. Values for the n=1 exciton are taken from high-resolution luminescence measurements [Var94]. The data of Fig. 4.8 and table 4.6 demonstrate that excitonic peaks shift with increasing temperature to the low energy side. Such a shift is linear in first approximation (Fig. 4.9). However, high-resolution luminescence experiments revealed that the linear temperature dependence of the FE luminescence starts only above 15 K in solid krypton [Var94].

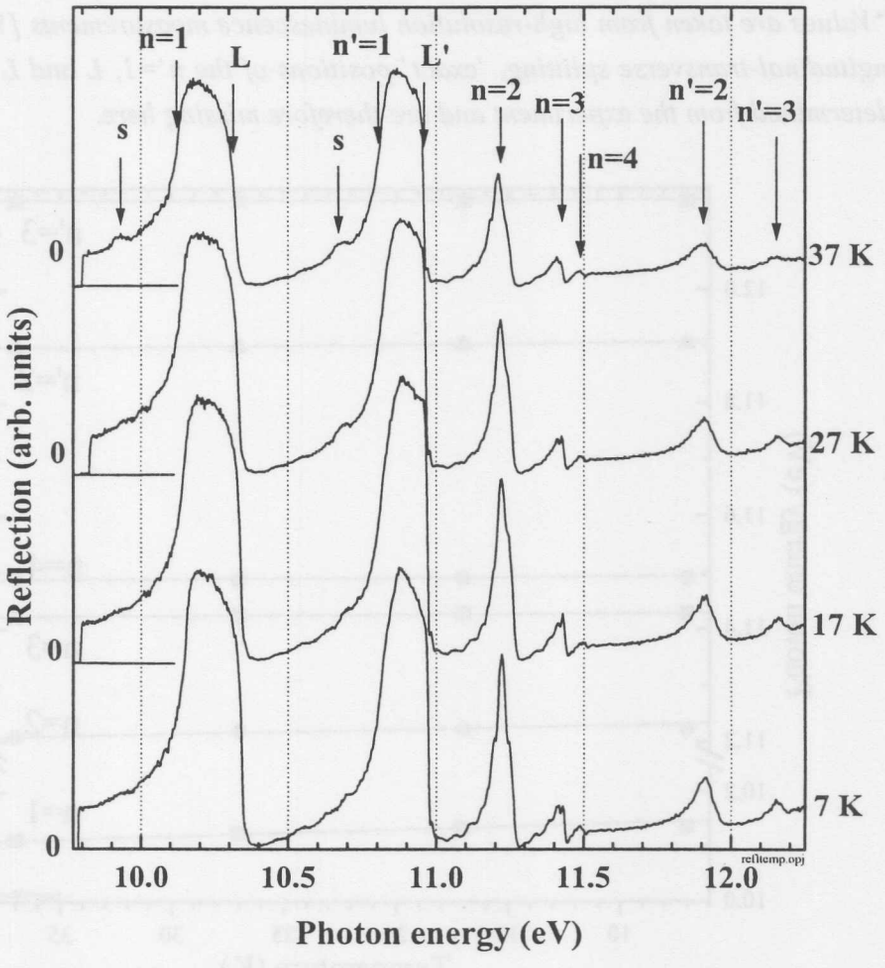

Figure 4.8: *High-resolution reflection spectra of solid Kr (sample 39, $\Delta\lambda$=0.55 Å) measured at various temperatures. The position of the n=1 exciton is taken from the high-resolution luminescence measurements [Var94], positions of the n'=1, L and L' are estimates.*

Exciton		7 K	17 K	27 K	37 K	mean shift meV/K
volume	n=1	10.137*	10.135*	10.124*	10.113*	0.8
	n=2	11.222	11.222	11.218	11.209	0.4
	n=3	11.428	11.429	11.424	11.420	0.3
	n=4	11.489	11.490	11.486	11.488	-
	n'=2	11.911	11.904	11.900	11.898	0.4
	n'=3	12.157	12.158	12.158	12.156	-
surface	n=1	-	-	-	9.931	-
	n'=1	-	-	10.684	10.679	-

Table 4.6: *Temperature dependence of the well-defined exciton peaks of solid krypton (sample 39). *Values are taken from high-resolution luminescence measurements [Var94]. Due to the longitudinal-transverse splitting, 'exact' positions of the n'=1, L and L' can not be directly determined from the experiment and are therefore missing here.*

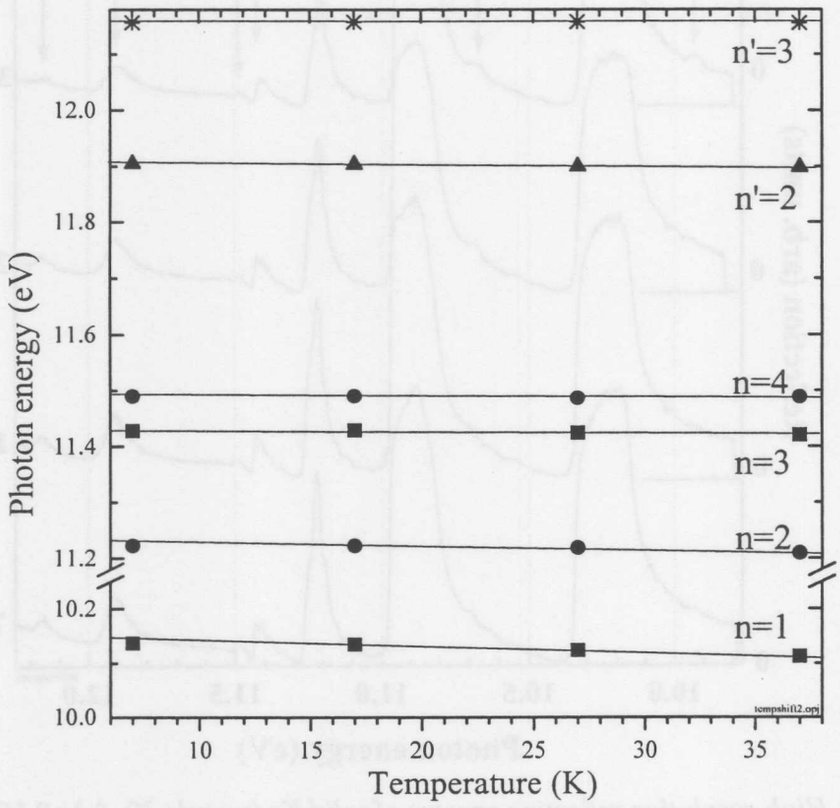

Figure 4.9: *Temperature dependence of exciton peak positions in the reflection spectra of solid krypton (sample 39). Symbols present experimental data and linear regressions are shown as solid lines. For the n=1 exciton high-resolution luminescence data is plotted [Var94].*

Such a phenomenon is known and was studied several times for solid xenon [SA73, Ste99]. In order to explain a linear temperature shift, two possibilities exist: (i) a red shift due to the decrease of the crystal density or (ii) a red shift due to the broadening of energy bands by phonons [SA73]. If the red shift is mainly due to broadening of the energy bands by phonons, the shift of the exciton peaks is supposed to be negligible below Debye temperature Θ_D (Θ_D=64.0 K for solid xenon and Θ_D=71.7 K for solid krypton). Since the observed red shift of the excitonic peaks was linear also below the Debye temperature, Steinberger and Asaf concluded [SA73] that the shift of the exciton bands with the temperature is due to the increase of the lattice constant with increasing temperature in solid Xe. The energies of the conduction and valence bands edges change with the lattice constant, and this change is quantitatively expressed by means of the deformation potential. Most probably, the shift in solid Kr has the same origin as in solid Xe.

4.5 Time-resolved measurement of FE luminescence

Time-resolved measurements permit to distinguish between different processes of FE creation and also to investigate such processes. For the first time, time-resolved excitation spectra of FE luminescence in solid Kr were measured using excitation up to ~35 eV during present work. Moreover, FE luminescence decay curves were systematically investigated in the energy range up to ~35 eV as well. Previous studies of the FE luminescence of solid Kr were mainly restricted to the excitonic energy region [Var94, Klo89].

4.5.1 FE decay curves

FE decay curves at different excitation energies are presented for a typical 'good quality' sample in Fig. 4.10 and Fig. 4.11 (sample 14, FE/STE ratio 0.84). The Al grating was used for excitation energies below 18 eV ($\Delta\lambda$=3.5 Å), and the Pt grating ($\Delta\lambda$=2.5 Å) was applied at higher energies. The spectral resolution of the secondary monochromator VUV-2 was set to $\Delta\lambda$=8 Å. The time-resolution of the MSP detector (320 ps, FWHM) was determined using the time-structure of straylight, shown at the bottom in both figures. Such a time-resolution is a convolution of the width of the synchrotron radiation pulse (130 ps, FWHM) and of the time-response of the detector and electronics. In the time-structure of the straylight, side-bunches are visible, delayed by 2 ns periodicity from the main-bunch. Since the maximal intensity of the side bunches was more than 200 times smaller compared to that of the main-bunch (t=0 ns), they did not affect significantly the shape of decay curves.

As experiments demonstrate, the variation of excitation energy causes considerable

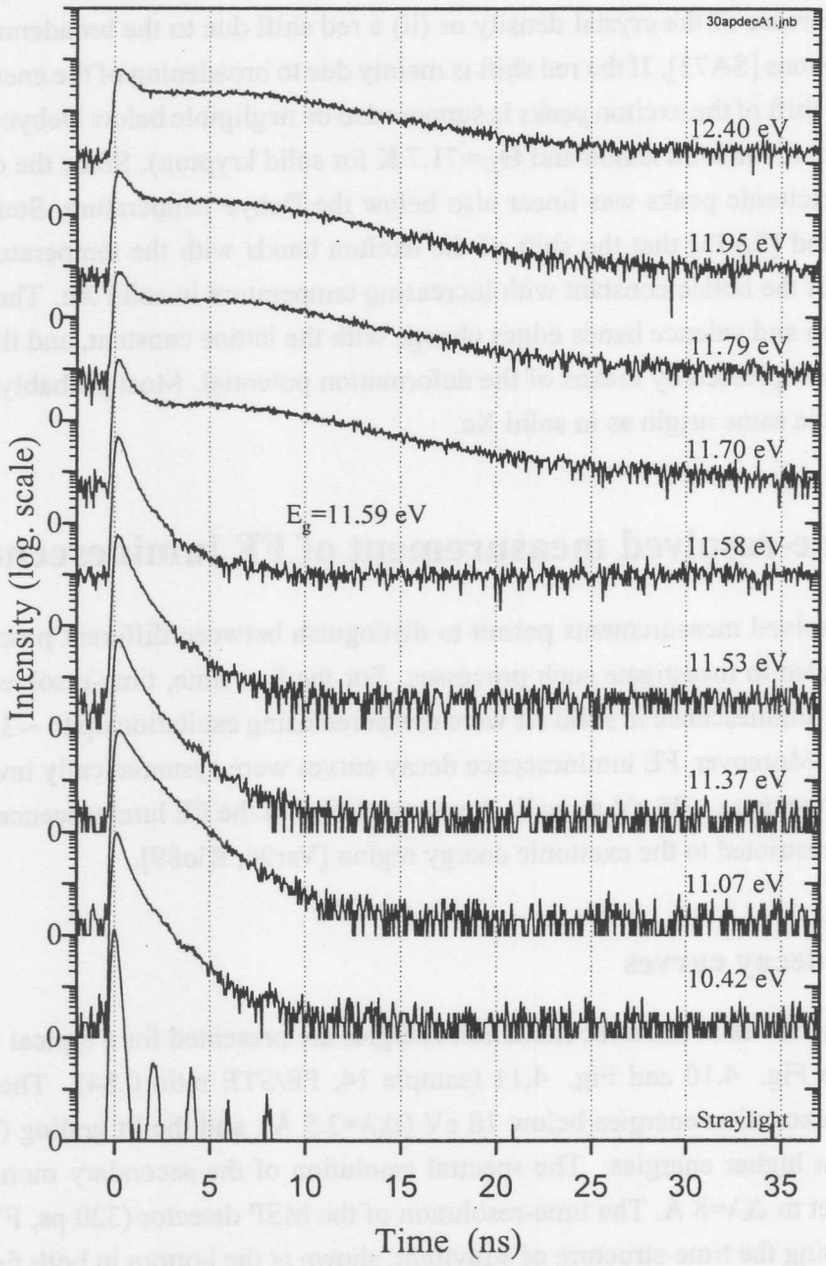

Figure 4.10: *Decay curves of FE luminescence (E_{ex}=10.14 eV) in solid Kr at 5 K (sample 14) at lower excitation energies. The shape of the excitation pulse is shown on the bottom. Time t=0 corresponds to the maximum signal intensity of the excitation pulse. Excitation energies are shown in the figure above respective curves.*

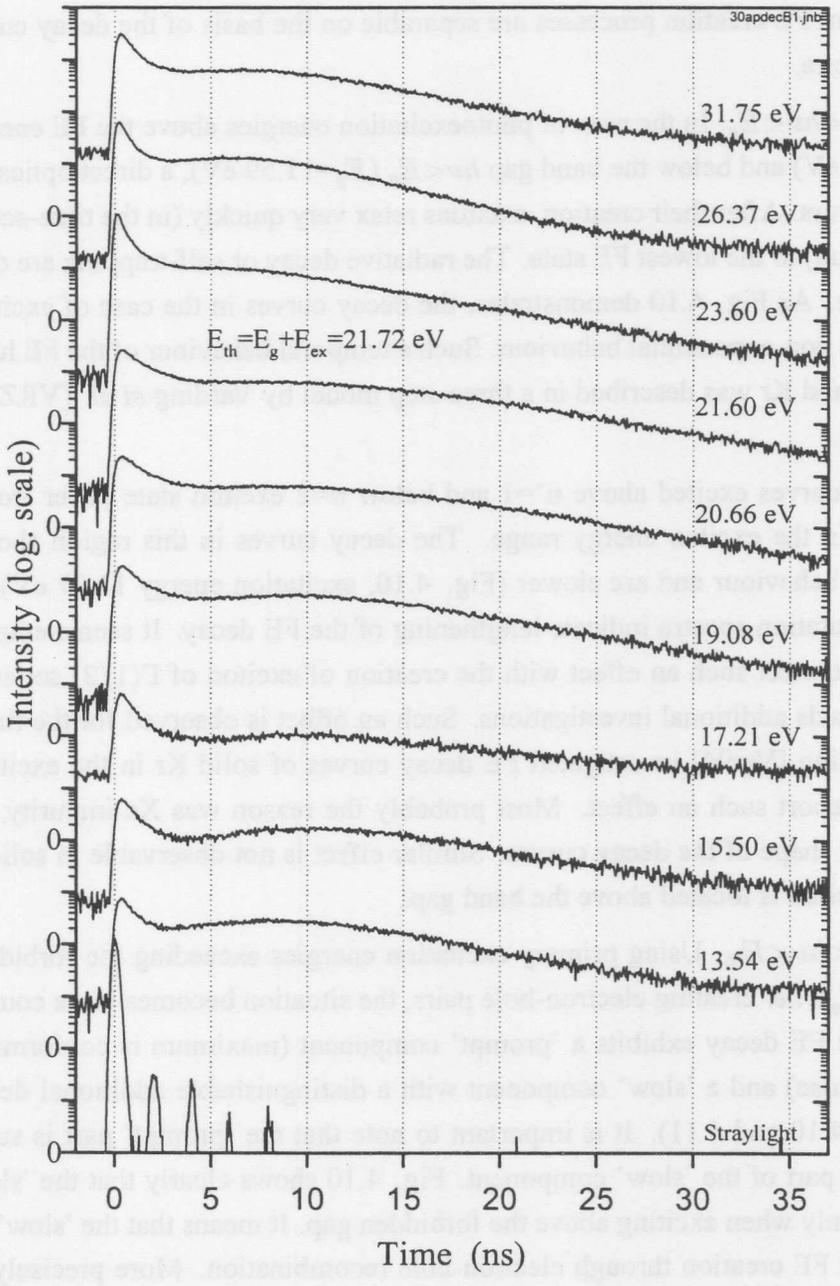

Figure 4.11: *Decay curves of FE luminescence (E_{ex}=10.14 eV) in solid Kr at 5 K (sample 14) at higher excitation energies. The shape of the excitation pulse is shown on the bottom. Time t=0 corresponds to the maximum signal intensity of the excitation pulse. Excitation energies are shown in the figure above respective curves.*

changes in the shape of FE decay curves. Different processes of FE creation lead to characteristic shapes of the FE decay curves. In the spectral-range of SUPERLUMI, three regions with different FE creation processes are separable on the basis of the decay curves and excitation spectra.

(i) $E_{ex}<h\nu<E_g$. In the case of photoexcitation energies above the FE energy $h\nu>E_{ex}$ (E_{ex}=10.13 eV) and below the band gap $h\nu<E_g$ (E_g=11.59 eV), a direct optical creation of excitons occurs. After their creation, excitons relax very quickly (in the time-scale of experimental set-up) to the lowest FE state. The radiative decay or self-trapping are depopulating this FE state. As Fig. 4.10 demonstrates, the decay curves in the case of excitonic excitations show a non-exponential behaviour. Such a temporal behaviour of the FE luminescence in solid Xe and Kr was described in a three-step model by Varding *et al.* [VRZ94] (chapter 3.4.2, p. 49).

Decay curves excited above n'=1 and below n=2 exciton state differ from other decay curves in the exciton energy range. The decay curves in this region show less non-exponential behaviour and are slower (Fig. 4.10, excitation energy 11.07 eV). Also time-resolved excitation spectra indicate lengthening of the FE decay. It seems empirically reasonable to connect such an effect with the creation of exciton of $\Gamma(1/2)$ series. However, this point needs additional investigations. Such an effect is observed for the first time. Although Varding [Var94] investigated FE decay curves of solid Kr in the excitonic region, he did not report such an effect. Most probably the reason was Xe impurity, influencing significantly shape of the decay curves. Similar effect is not observable in solid Xe, where the n'=1 exciton is located above the band gap.

(ii) $E_g<h\nu<E_{th}$. Using primary excitation energies exceeding the forbidden gap energy ($h\nu>E_g$), *i.e.* creating electron-hole pairs, the situation becomes more complicated. In that case the FE decay exhibits a 'prompt' component (maximum is conforming with the excitation pulse) and a 'slow' component with a distinguishable additional delayed maximum (Fig. 4.10 and 4.11). It is important to note that the 'prompt' part is superimposed to the rising part of the 'slow' component. Fig. 4.10 shows clearly that the 'slow' component exists only when exciting above the forbidden gap. It means that the 'slow' component is caused by FE creation through electron-hole recombination. More precisely, the 'slow' component is a convolution of the temporal evolution of electron-hole recombination into an excitonic state and the decay of the free excitons. It is quite natural to expect that by increasing the excitation energy, electrons with higher kinetic energy need more time to relax down to the bottom of the conduction band and the maximum of the 'slow' component is more delayed. As discussed before (section 3.5.1, p. 51), it is possible to simulate experimental decay curves of the 'slow' component with model calculations in the excitation

region $E_g < h\nu \lesssim E_g$+1.5 eV. A comparison between experimental results and calculations will be presented afterwards (section 4.9, p. 115).

The origin of the 'prompt' component in this energy-region is not well understood. This component has a decay time, much longer than the straylight (Fig. 4.10 and 4.11). Consequently, it is without any doubt a FE luminescence signal and is not due to scattered light. To explain the origin of 'prompt' component, two possibilities exist. (i) It could be an experimental artefact originating from a FE luminescence signal excited by scattered light of the primary monochromator. To exclude such an excitation possibility, it is necessary to use a monochromator with an extremely small scattered light background, *e.g.* a double monochromator. Another challenge is to use a monochromatic light-source. In VUV spectral range, such a light source can be a free-electron laser. (ii) It cannot be excluded, that the 'prompt' component has an yet unknown physical origin. Unfortunately, up to our knowledge no suitable theory describing the phenomenon has been developed. Only very speculatively, the formation of the 'prompt' component may be connected with the 'geminate recombination' model, where the created electron stays in close spatial proximity of its counterpart hole and their fast mutual recombination leads to the FE formation [Mik87]. Consequently, the origin of the 'prompt' component needs additional investigations. An analogous effect has been detected in solid Xe in the case of excitation above the band gap. Nevertheless, there is a different situation, because the 'prompt' component in solid Xe has a shape, characteristic for straylight [Ste99]. Therefore, the 'prompt' component of the FE decay in solid Xe is most probably an experimental artefact, which has to be proved as well.

(iii) $h\nu > E_{th}$. The shape of the decay curves changes significantly above an experimental threshold energy $h\nu$=E_{th} $\approx$21.7 $\pm$ 0.2 eV. The energy value of this threshold is determined from the time-resolved excitation spectra and will be discussed in the next section. This experimental threshold value is nearly equal to the sum of the band gap energy and the exciton energy (E_{th}=E_g+E_{ex}). As Fig. 4.11 shows, the intensity of the 'prompt' part of the FE decay curves increases essentially above this threshold. This happens, since for excitation energies above the threshold at E_{th} $\approx$21.7, two excitations per one absorbed photon can be created. The threshold at $\sim$21.7 eV can be explained (i) by secondary exciton creation via inelastic scattering of 'hot' photo-electron in a two step process, (see section 3.7) [VFM99], or (ii) by simultaneous creation of an exciton and a electron-hole pair in a one-step process (electronic polaron complex, see section 3.8) [DKC72]. Although the threshold itself arises from creation of an exciton and an electron-hole pair, at higher photoexcitation energies the creation of two electron-hole pairs occurs as well. After creation of two excitations above E_{th}, the electrons are again close to the bottom of the conduction band having 'small' kinetic energy and the maximum of the 'slow' component shifts back

to shorter times. However, the shape of the 'slow' component above E_{th} is not so well defined, compared to that of directly excited above E_g, since the energy of electrons in the conduction band can be differently distributed at similar exciting photon energy.

4.5.2 Excitation spectra of FE luminescence

In the case of time-resolved excitation spectra, two time-connected parameters can be varied: the length of the time-window (Δt) and the delay of the time-window from the excitation pulse (δt; in this work, it is calculated starting from the *maximum* of the straylight peak). Time-resolved excitation spectra of FE luminescence for a typical 'good quality' sample (sample 25) are presented in Fig. 4.12. This figure shows FE excitation spectra measured in several time-windows: 'hot' (Δt=0.94 ns, δt=0 ns), 'short' (Δt=1.57 ns, δt=0.59 ns), 'long' (Δt=5.04 ns, δt=2.57 ns) and 'very long' (Δt=32.5 ns, δt=7.2 ns) time-window. These 'names' of the time-windows will be used in the following discussions. For comparison, the time-integrated FE excitation spectrum and the reflection spectrum are also shown. The resolution of the primary monochromator was 2.2 Å (in excitation) and of the secondary monochromator was set to 11 Å (in emission). A sharp straylight peak above 20 eV is caused by the second order of the monochromator, directly demonstrating the good spectral resolution of the secondary monochromator.

Depending on the delay time and the length of the time-window, different relaxation processes are observed. As Fig. 4.12 shows, it is possible to observe a straylight peak above 20 eV in the 'hot' time-window, but not any more in the 'short' time-window (δt >0.59 ns). This does not mean, that the 'prompt' processes (in the meaning of the time-resolution of SUPERLUMI set-up) can be detected only in the 'hot' time-window. The 'prompt' processes give also some contribution to the time-windows with longer delay, because the decay of the 'prompt' excitons extends to longer times.

Immediate creation of FE ('hot' window, Δt=0.94 ns and δt=0 ns) is predominant in two regions: in the excitonic region ($h\nu<E_g$) and in the region above the threshold ($h\nu>E_{th}$ ≈21.7 eV). A precise energetic location of the experimental threshold will be discussed in details afterwards. In the excitonic region, direct creation of excitons and their fast phonon-assisted relaxation to the lowest FE state occurs. As mentioned before, the threshold at ~21.7 eV can be explained (i) by the so-called process of multiplication of electronic excitations in the framework of multiple-parabolic-branch band model [VFM99], or (ii) by simultaneous creation of a FE and an electron-hole pair in a one-step process (electronic polaron complex) [DKC72]. Both models predict a theoretical threshold at $E_{th}^{theo}=E_g+E_{ex}$ ≈21.72 eV, which is in very good agreement with the experimental value $E_{th}=E_g+E_{ex}$ ≈21.7 ±0.2 eV. A remarkable change of the shape of the FE decay curves

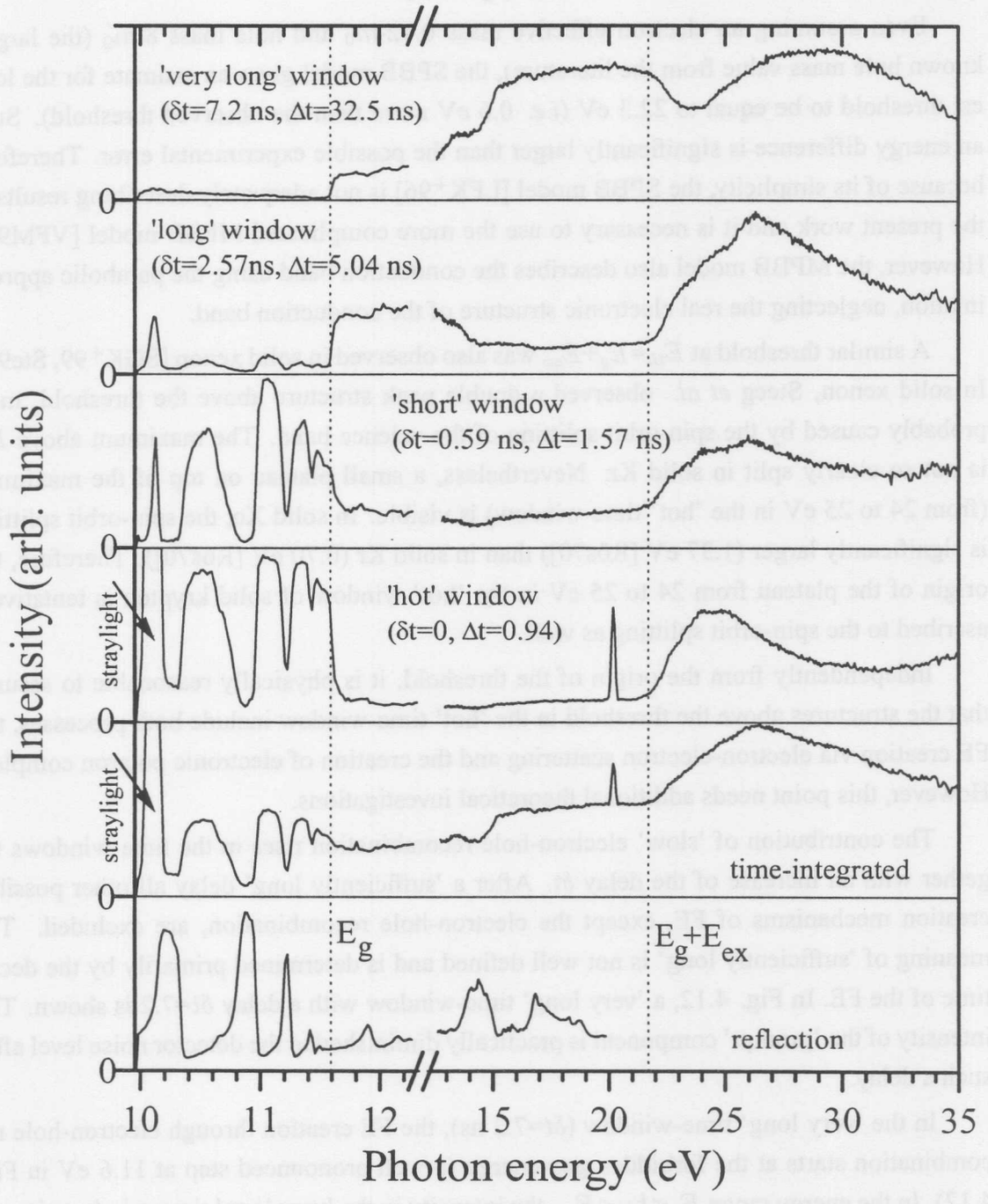

Figure 4.12: *Time-integrated and time-resolved excitation spectra of FE luminescence at 10.1 eV (sample 25, T=6 K, $\Delta\lambda_{exc}$=2.2 Å, $\Delta\lambda_{lum}$=11 Å). For a comparison, the reflection spectrum is also shown. The sharp peaks slightly above 20 eV, pronounced in the 'hot' time-window and time-integrated spectra, are caused by the second order of the secondary monochromator. The parameters of the time-windows are denoted in the figure.*

correlates with this threshold as well (see Fig. 4.11).

Even assuming an electron effective mass $0.42 \cdot m_0$ and hole mass $8 \cdot m_0$ (the largest known hole mass value from the literature), the SPBB model gives an estimate for the lowest threshold to be equal to 22.3 eV (*i.e.* 0.6 eV more than the observed threshold). Such an energy difference is significantly larger than the possible experimental error. Therefore, because of its simplicity, the SPBB model [LFK+96] is not adequately describing results of the present work and it is necessary to use the more complicated MPBB model [VFM99]. However, the MPBB model also describes the conduction band using the parabolic approximation, neglecting the real electronic structure of the conduction band.

A similar threshold at $E_{th}=E_g+E_{ex}$ was also observed in solid xenon [SGK+99, Ste99]. In solid xenon, Steeg *et al.* observed a double peak structure above the threshold, most probably caused by the spin-orbit splitting of the valence band. The maximum above E_{th} is not so clearly split in solid Kr. Nevertheless, a small plateau on top of the maximum (from 24 to 25 eV in the 'hot' time-window) is visible. In solid Xe, the spin-orbit splitting is significantly larger (1.37 eV [Rös70]) than in solid Kr (0.70 eV [Rös70]). Therefore, the origin of the plateau from 24 to 25 eV in the 'hot' window of solid krypton is tentatively ascribed to the spin-orbit splitting as well.

Independently from the origin of the threshold, it is physically reasonable to assume that the structures above the threshold in the 'hot' time-window include both processes, the FE creation via electron-electron scattering and the creation of electronic polaron complex. However, this point needs additional theoretical investigations.

The contribution of 'slow' electron-hole recombination rises in the time-windows together with an increase of the delay δt. After a 'sufficiently long' delay all other possible creation mechanisms of FE, except the electron-hole recombination, are excluded. The meaning of 'sufficiently long' is not well defined and is determined primarily by the decay time of the FE. In Fig. 4.12, a 'very long' time-window with a delay δt=7.2 is shown. The intensity of the 'prompt' component is practically diminished to the detector noise level after such a delay.

In the 'very long' time-window (δt=7.2 ns), the FE creation through electron-hole recombination starts at the forbidden gap energy (a well pronounced step at 11.6 eV in Fig. 4.12). In the energy range $E_g<h\nu<E_{th}$, the intensity in the 'very long' time-window rises as well. This is due to the retardation of electron-hole recombination, which shifts the intensity maximum of the 'slow' component of FE decay curves to longer times, *i.e.* more intensity is detected within 'very long' time-window.

Above the threshold E_{th}, the creation of two electronic excitations takes place introducing changes in the excitation spectra. The intensity increase takes place in all time-windows,

except the 'very long' time-window. A decrease of the intensity within the 'very long' time-window above E_{th} does not mean a decrease of the number of created electron-hole pairs, but rather the decrease of the kinetic energy of the created electrons. The amount of the created electron-hole pairs slightly above E_{th} is the same as before, since the photon energy is sufficient to create an electron-hole pair plus an exciton, but not yet two electron-hole pairs. Intensity growth in the 'very long' time-window at ~24 eV is caused by the following reasons: (i) photons have now enough energy to create two electron-hole pairs, (ii) the initial kinetic energy of the electrons in the conduction band increases as well and the maximum of the 'slow' component of the decay curve shifts again to longer times, *i.e.* the amount of the emitted photons in the 'very long' time-window increases.

It is important to note, that the 'slow' component of the FE decay curve is very sensitive regarding the excitation density. In the case of a 'small' excitation density (*i.e.* a light-spot which is not well focused on the sample), the 'slow' component of FE decay curve is rather weak. At first sight, such an experimental result seems to be contradictory to the theoretical results (section 3.5.2), where a decrease of the excitation density (Fig. 3.11) shifts the maximum of the 'slow' component to longer times. But most important is that a higher excitation density shifts the maximum of the 'slow' component to shorter times with simultaneous drastic increase of its intensity. Such an effect is shown in Fig. 3.12, where the decay curves are not normalized. Hence, the experimental and theoretical results are consequently in good agreement. The behaviour of spectra in the 'very long' time-window is also in some degree sample sensitive due to the amount of as-grown and radiation induced defects.

The spectra measured in two intermediate time-windows ('short' and 'long') in Fig. 4.12 reflect the 'prompt' FE creation processes as well as the 'slow' FE creation through electron-hole recombination. The 'prompt' FE creation dominates in the 'short' time-window (Δt=1.57 ns, δt=0.59 ns) and the electron-hole recombination in the 'long' time-window (Δt=5.04 ns, δt=2.57 ns). As Fig. 4.12 demonstrates, the maxima in the excitation spectra above the threshold shift slightly to the higher energy side with an increase of the delay δt.

Excitation spectra of the FE luminescence were measured on several samples during this work. Fig. 4.13 displays the threshold region of 'hot' and 'short' time-window in excitation spectra for two typical samples of 'good quality' in an enlarged scale. The general behaviour of both spectra is similar. The observed thresholds are well-distinguishable and reproducible. The accuracy of the experimental threshold value is determined by the spectral resolution of the monochromator and by differences in the 'quality' of samples. Moreover, there are some difficulties involved concerning the analysis of data (*e.g.* treatment of the

back-ground at the low energy side of the threshold, *etc.*). Therefore, including all these factors, the value of the threshold is most probably determined with an accuracy of ± 0.2 eV. The threshold in the 'short' time-window is somewhat less pronounced and shifted roughly 0.2 eV to the higher energy side compared to that of in the 'hot' time-window. There are also some differences in the shape of the spectra near threshold. In the case of sample 16 (Fig. 4.13, on top) the threshold is well defined. Sample 25 (Fig. 4.13, at the bottom) shows also a small transition region at the threshold.

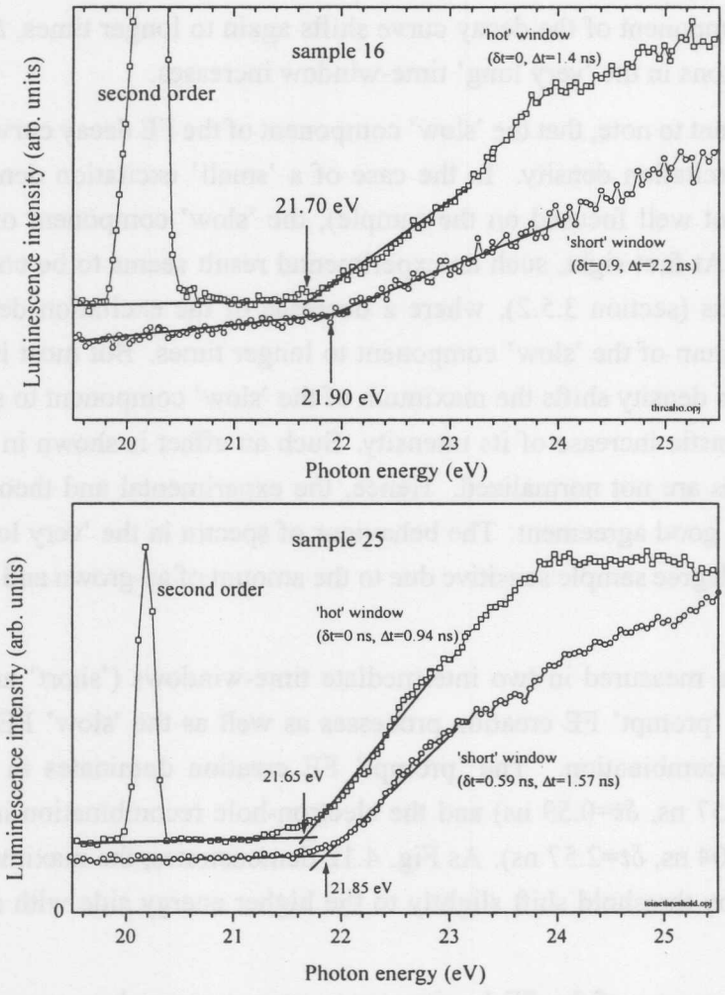

Figure 4.13: *The threshold region of the FE excitation spectra in solid Kr for two 'good quality' samples. On the top: sample 16 at 6 K (FE:STE ratio 1.35, spectral resolution $\Delta\lambda$=2.6 Å). At the bottom: sample 25 at 6 K (spectral resolution $\Delta\lambda$=2.2 Å).*

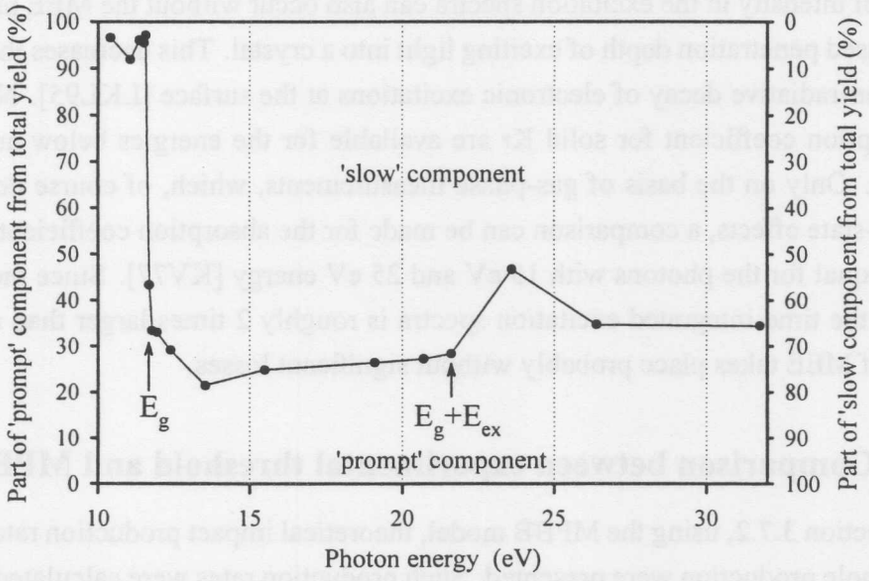

Figure 4.14: *Ratio of the 'prompt' and 'slow' component in the FE luminescence as a function of photon energy. This figure is constructed on the basis of the FE decay curves of sample 25. The intensity before t=2.5 ns is defined as 'prompt' and after t=2.5 ns as 'slow'.*

The time-resolved excitation spectra cannot give a full understanding, how the intensity is divided between the 'prompt' and the 'slow' component. This happens, since the maximum position of the 'slow' component on a time-scale depends on the exciting photon energy, but the preselected time-windows are fixed on the time-scale. Fig. 4.14 gives a more adequate information about the intensity ratio of the 'prompt' and the 'slow' component. This figure is constructed on the basis of the FE decay curves of sample 25. The intensity before t=2.5 ns is defined as 'prompt' component and after t=2.5 ns as 'slow' component. Of course such an approximation includes some error, since the signal before t=2.5 ns includes a small amount of the 'slow' component and vice versa. Assuming that these errors compensate each other, the total error cannot be too big ($\sim$5%).

As Fig. 4.14 shows, in the case of an excitation above the forbidden gap, the 'slow' component dominates, giving 70...80 per cent from the total FE luminescence intensity. In accordance with the 'hot' time-window in time-resolved excitation spectra, the contribution of the 'prompt' component rises above the threshold E_{th} to a maximal value of $\sim$45 % and then decreases again. So, the results of decay curve measurements are in good agreement with those obtained from the time-resolved excitation spectra.

To analyze the multiplication of electronic excitations (MEE) correctly, it is necessary to eliminate the effects caused by significant changes of the absorption coefficient. The

increase of intensity in the excitation spectra can also occur without the MEE process due to the increased penetration depth of exciting light into a crystal. This decreases the probability for the non-radiative decay of electronic excitations at the surface [LKL95]. No data about the absorption coefficient for solid Kr are available for the energies below and above the threshold. Only on the basis of gas-phase measurements, which, of course do not include any solid-state effects, a comparison can be made for the absorption coefficient in Kr, being roughly equal for the photons with 15 eV and 25 eV energy [KV77]. Since the intensity at 25 eV in the time-integrated excitation spectra is roughly 2 times larger than at 15 eV, the process of MEE takes place probably without significant losses.

4.5.3 Comparison between experimental threshold and MPBB model

In section 3.7.2, using the MPBB model, theoretical impact production rates for FE and electron-hole production were presented. Such production rates were calculated on the basis of the theory, developed by Vasil'ev *et al.* [VFM99]. Fig. 4.15 shows a comparison between the experimental FE excitation spectrum and theoretical calculations. It is important to note that such a comparison is only approximate due to the following reasons:

- Vasil'ev *et al.* made theory in terms of the electron kinetic energy and therefore, those calculations are not exactly comparable with the experimental photoexcitation data. In Fig. 4.15, a forbidden gap energy is added to the results on the basis of Vasil'evs theory, ignoring effects caused by the structure of the valence band. New theory of production rates under photoexcitation will be published soon and a more accurate comparison between theoretical and experimental results becomes possible [Vas00].
- The MPBB model is applicable only near the threshold energy and slightly above, since this approach uses the perturbation theory of the lowest order [Vas00]. Therefore, only an energy region $\sim$1 eV above threshold energy is shown in Fig. 4.15.
- The numerical values of the production rate can be overestimated due to the chosen scaling factor [Vas00].
- Vasil'ev *et al.* used in their calculations an effective electron mass equal to the free electron mass, because generally the free electron approximation is used for describing 'higher' conduction band states. This is in accordance with experimental results as well ($m_e \approx 1.1 \cdot m_0$ for 'higher' states in the conduction band) [BPCS84]. Nevertheless, the effective mass near the band bottom is assumed to be significantly smaller than the free electron mass ($m_e \approx 0.42 \cdot m_0$). Also a strong perturbation of parabolic bands occurs at the border of the first Brillouin zone. Only calculations on the basis of a 'real' band-structure can take into account such effects .

Notwithstanding all those problems, the 'hot' time-window of FE excitation spectra

and calculated FE production rate are depicted in Fig. 4.15. This figure demonstrates the principal possibility to create secondary excitons in a two step process (*i.e.* via electron-electron scattering) using the MPBB framework. The agreement is rather good in the energy range of validity of the MPBB model as discussed above. However, the 'good' agreement partly arises from the fact that arbitrary scales are used. Outside of the energy range plotted in the figure, the theoretical rate for exciton production increases more rapidly, while the measured curve reaches its maximum at ~24 eV.

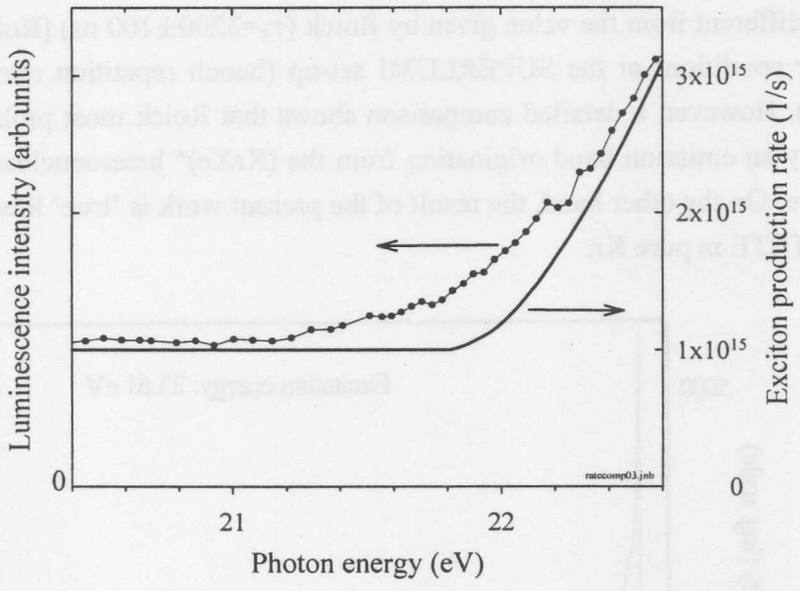

Figure 4.15: *Comparison between the 'hot' time-window (Δt=0.94 ns, δt=0 ns) in FE excitation spectrum (sample 25, T=6 K, the spectral resolution $\Delta\lambda$=2.2 Å) and the calculated FE production rate in the threshold region. A constant back-ground is added to the calculated production rate of FE.*

4.6 Time-resolved measurements of STE luminescence

The STE luminescence is a superposition of the luminescence arising from two different states of the STE: the singlet (τ_s=1.1 ns [Roi84]) and the triplet state (τ_t=830±100 ns, this work). Fig. 4.16 depicts a typical decay curve of the STE luminescence of a 'good quality' sample measured in the *two bunch mode* of DORIS. A strong background appears, since a lifetime of the triplet component is comparable with the repetition rate of DORIS (480 ns in *two bunch mode*). In the case of the decay curve, shown in Fig. 4.16, the singlet component contributes only ~3 % to the total luminescence intensity. The lifetime of the triplet component should be practically independent from the photoexcitation energy, since

relaxation processes into the triplet state are much faster than the decay of the respective state. DORIS does not offer optimal conditions for a measurement of the triplet component lifetime and its value τ_t=830±100 ns is obtained from a measurement, in which the luminescence intensity decreases only by factor of two. Such a decrease is much smaller than that for the FE decay curves, in which the dynamic range of the intensity covers a few orders of magnitude. Error ±100 ns is not the statistical error of the fit, but is pointing to the fact that the lifetime obtained under different excitation energies show some scatter. At first sight it is surprising that the lifetime of the triplet state from this work (τ_t=830±100 ns) is significantly different from the value given by Roick (τ_t=3200±100 ns) [Roi84], measured under similar conditions at the SUPERLUMI set-up (bunch repetition rate 960 ns, temperature 6 K). However, a detailed comparison shows that Roick most probably observed predominantly an emission band originating from the (KrXe)* heteronuclear centre with a 'long' lifetime. On the other hand, the result of the present work is 'true' lifetime for triplet component of STE in pure Kr.

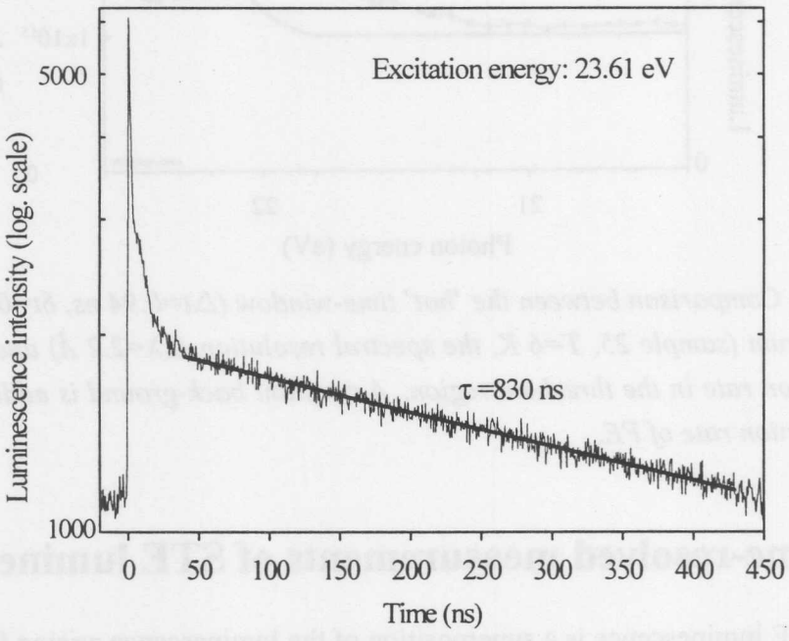

Figure 4.16: *The STE decay curve in solid krypton (luminescence detected at 8.55 eV, 'good quality' sample 29, T=6 K). For the determination of the lifetime of the triplet component (τ_t= 830 ns) the time-range from 50 to 430 ns was used. The measured curve is depicted by a solid line. The one-exponential fit is shown as a bold line. Luminescence from the triplet state dominates and only ~3 % of the total intensity arises from the singlet state.*

Differently from the triplet component, the shape of the decay curve for the singlet

component of STE luminescence depends strongly on the excitation energy. This happens, since the relaxation to the STE state takes place, if not completely then to a considerable degree through the FE state. Therefore, a 'real' lifetime of the singlet state can be measured only exciting below the FE state. Such a measurement gave a value τ_s=1.1 ns [Roi84]. Fig. 4.17 shows the singlet component of STE luminescence in solid Kr, excited in the excitonic region, as well as an instrumental time-response of experimental set-up (*i.e.* a straylight signal). In this case the decay time is a superposition of the lifetime of singlet component and that of the FE.

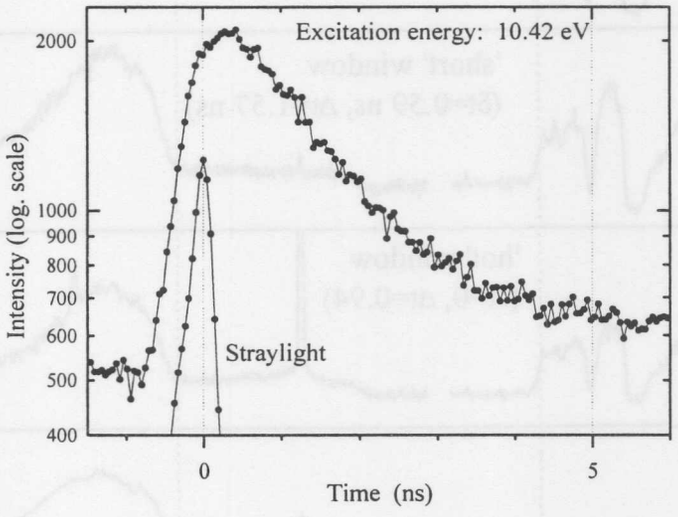

Figure 4.17: *The decay of singlet component of the STE luminescence in solid krypton measured at 8.55 eV in the case of excitonic excitation (sample 24, FE:STE ratio 0.54, T=6 K, excitation energy 10.42 eV). For a comparison, the instrumental time-response of the experimental set-up is shown.*

Fig. 4.18 shows the time-resolved excitation spectra of the STE luminescence in solid krypton. The spectra were measured for 'good quality' sample 25 and accordingly are comparable with the FE excitation spectra, measured for sample 25 as well (Fig. 4.12). Also, the same time-windows were applied in measurements plotted in Fig. 4.18 and Fig. 4.12. The time-integrated excitation spectrum of STE is mainly due to the long-living triplet component of STE. This is a reasonable assumption, since the singlet component contributes to the integral luminescence only ~3 %. The excitation spectrum of pure triplet component of STE is shown in the 'very long' (Δt=32.5 ns, δt=7.2 ns) time-window. On the other hand, the singlet component of the STE prevails in the 'hot' time-window (Δt=0.94 ns, δt=0 ns), but the 'hot' time-window includes also a significant triplet-background. As Fig. 4.18 shows, all spectra measured in different time-windows of STE luminescence behave in the

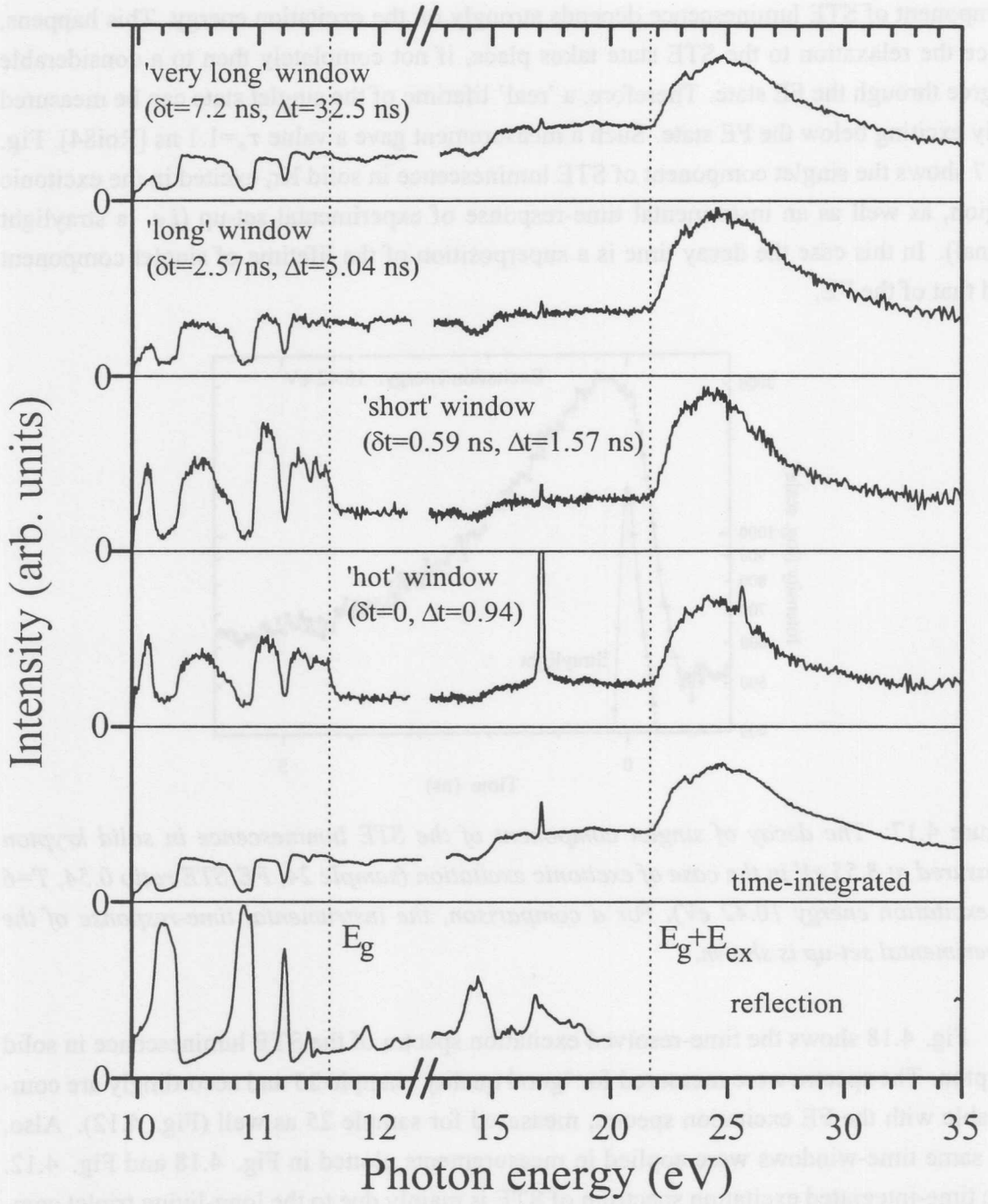

Figure 4.18: *Time-integrated and time-resolved excitation spectra of STE luminescence detected at 8.55 eV in different time-windows (sample 25, T=6 K, $\Delta\lambda_{excit}$=2.2 Å, $\Delta\lambda_{lum}$=11 Å). For a comparison, the reflection spectrum is also shown. The sharp peaks above 17 eV pronounced in the 'hot' time-window and in the integral spectra are caused by the second order of the secondary monochromator. The parameters of the time-windows are denoted in the figure.*

same way, except in the excitonic region. The luminescence intensity in the excitonic region is significantly stronger within the 'hot' and 'short' time-windows. In time-windows with a longer delay, the intensity maxima in the excitonic region do not exceed the intensity in the band to band excitation region.

The spectrum in the 'hot' time-window (Δt=0.94 ns, δt=0 ns) of the STE luminescence behaves analogously to the 'hot' time-window spectrum of the FE luminescence. In both cases, the luminescence is efficiently excited in the excitonic region and above the threshold E_{th}=E_g+E_{ex}. The experimental value of the threshold from STE spectra (~21.7 eV) coincides with the one obtained from FE measurements (~21.7 eV). If not all, then at least a large amount of STE are created through the FE state. Since the singlet component of the STE luminescence has a very short lifetime, the 'hot' time-window of the STE luminescence repeats the structure of the 'hot' time-window of FE luminescence excitation spectra. The main difference in the spectra measured in the 'hot' time-windows shows up between E_g and E_{th}, the STE signal being relatively stronger than the FE signal. This seems to be caused by the background contribution of luminescence from the triplet state in the 'hot' time-window of the STE luminescence.

FE and STE luminescence behave extremely differently in the windows with the longer delay ('long' and 'very long' window in Fig. 4.12 and 4.18). In the case of such time-windows, the excitation spectra of FE luminescence are controlled by 'slow' electron-hole recombination. In the case of STE luminescence, excitation spectra are controlled by the long-living triplet state of the STE.

Recently published data for solid Xe [Ste99] allow to compare time-resolved STE excitation spectra with respective spectra of solid Kr. Spectra in the time-windows, where the singlet component is dominant, behave analogously in both cases. The most significant difference between Kr and Xe results concerns the behaviour of time-integrated excitation spectra and also spectra in the 'very long' time-window. In solid Kr, the intensity in the region $E_g < h\nu < E_{th}$ is rather stable and an increase above the threshold E_{th}=E_g+E_{ex} is quite strong. On the contrary, in solid Xe the intensity rises steadily above the band gap and the threshold at E_{th} is less pronounced.

4.7 Ratio of FE and STE luminescence excitation spectra

The ratio of the time-integrated FE and STE excitation spectra (ratio spectra) offer additional information about creation and relaxation of electronic excitations. At the same time, all kinds of the possible FE and STE creation processes contribute to the ratio spectra and therefore, an interpretation of such spectra is by far not trivial. Fig. 4.19 depicts

such FE/STE ratio spectra. Two measurements were carried out using the platinum grating (sample 16 and 25) and one (sample 23) with the aluminum grating. For a comparison, the reflection spectrum (sample 25) is also shown. The sharp narrow minima at ~17 eV and maxima at ~20 eV are caused by the second order of the secondary monochromator. Measurements with the aluminum grating permit to monitor processes in the low-energy range (roughly below 15 eV) without a disturbing contribution of higher order excitation due to the primary monochromator. The use of the ratio spectra precludes also an experimental inaccuracy, caused by the normalization of the recorded spectra. This method offers as well an important opportunity to remove the disturbing influence of the reflection coefficient, since reflection losses are included in both excitation spectra canceling with each other in the ratio spectra.

Above the band-gap, the FE/STE ratio spectra are nearly independent from photon energy of excitation. A shallow minimum is located above threshold E_{th}. As explained before, the modulations in the excitonic region are not connected with the variation of the reflection coefficient. In principle, between measurements of FE and STE excitation spectra the reflection coefficient of the sample can be slightly changed due to the condensation of the residual gases onto the sample. Analyses of the reflection spectra, recorded simultaneously with the FE and STE excitation spectra, show that both reflection spectra are practically identical. Therefore, a possible effect of reflectivity alteration can be excluded.

In the excitonic region, the modulations in the ratio spectra phenomenologically mean that the FE creation is more probable (or the STE creation is less probable), if the penetration depth of the exciting light is deeper (*i.e.* the absorption coefficient is smaller). The modulations in this range being systematically correlated to the penetration depth of the exciting light, might be caused by variations of the balance between radiative FE decay and self-trapping. It is entirely reasonable that self-trapping is more favourable near the surface than in the bulk.

In the region of $E_g < h\nu < E_{th}$, the creation of the STE is clearly proportional to the creation of the FE. The smooth behaviour of the FE/STE ratio spectra above the band gap strongly supports the idea that the STE originating from electron-hole recombination has FE states as precursors. In other words, recombination leads to the creation of free excitons which then either radiate or get localized into the STE state.

Above E_{th}, there is a small region, where the probability for STE creation increases (or the probability for the FE creation decreases). The peculiarity (minimum) above E_{th} is always present and the depth of this minimum is similar to the one at the n'=1 exciton. The ratio indicates, that some peculiarities in relaxation processes play a role in the region where electron-hole pair and exciton are created compared to the band to band transition region.

The variation of the ratio spectra above ~27 eV in different samples needs additional investigations before providing any interpretation.

FE/STE ratio spectrum was also presented for solid Xe [Ste99]. This shows similar modulations in the excitonic region. Above the band gap E_g, the ratio spectrum is quite smooth, with some weak structures extending roughly up to ±15 % from its average value. Above E_{th} a noticeable decrease is absent in the FE/STE ratio spectra in solid Xe.

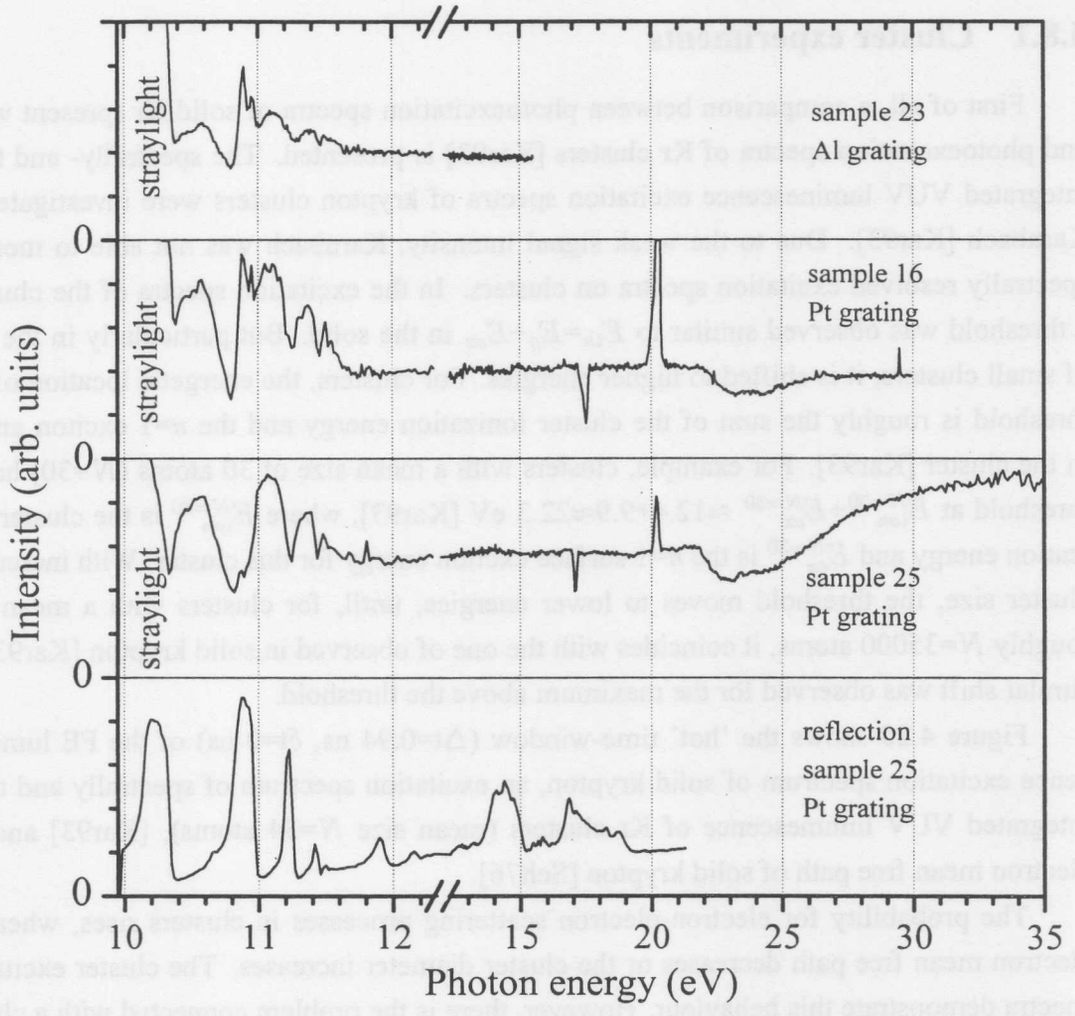

Figure 4.19: *Ratio spectra of the time-integrated FE and STE emissions as a function of photon energy of excitation. Two spectra were measured with the platinum grating (sample 16: T=6 K, $\Delta\lambda_{excit}$=2.6 Å, $\Delta\lambda_{lum}$=7 Å and sample 25: T=6 K, $\Delta\lambda_{excit}$=2.2 Å, $\Delta\lambda_{lum}$=11 Å) and one (sample 23: T=6 K, $\Delta\lambda_{excit}$=3.0 Å, $\Delta\lambda_{lum}$=10 Å) with the aluminum grating. The reflection spectrum (sample 25) is also shown at the bottom. The sharp narrow minima and maxima at ~17 eV and at ~20 eV arise from second order of the secondary monochromator.*

4.8 Comparison with other experiments

In the following section, the photoluminescence data of the present work and data of other experiments known from the literature will be compared. Such a comparison gives additional information about the origin of the threshold at $E_{th}=E_g+E_{ex}$ and the subsequent maximum in the photoexcitation spectra of FE and STE in solid Kr.

4.8.1 Cluster experiments

First of all, a comparison between photoexcitation spectra of solid Kr (present work) and photoexcitation spectra of Kr clusters [Kar93] is presented. The spectrally- and time-integrated VUV luminescence excitation spectra of krypton clusters were investigated by Karnbach [Kar93]. Due to the weak signal intensity, Karnbach was not able to measure spectrally resolved excitation spectra on clusters. In the excitation spectra of the clusters, a threshold was observed similar to $E_{th}=E_g+E_{ex}$ in the solid. But particularly in the case of small clusters, it is shifted to higher energies. For clusters, the energetic location of this threshold is roughly the sum of the cluster ionization energy and the n=1 exciton energy in the cluster [Kar93]. For example, clusters with a mean size of 30 atoms (N=30) have a threshold at $E_{ion}^{N=30}+E_{ex}^{N=30} \approx 12.4+9.9 \approx 22.3$ eV [Kar93], where $E_{ion}^{N=30}$ is the cluster ionization energy and $E_{ex}^{N=30}$ is the n=1 surface exciton energy for this cluster. With increasing cluster size, the threshold moves to lower energies, until, for clusters with a mean size roughly N=35000 atoms, it coincides with the one of observed in solid krypton [Kar93]. A similar shift was observed for the maximum above the threshold.

Figure 4.20 shows the 'hot' time-window (Δt=0.94 ns, δt=0 ns) of the FE luminescence excitation spectrum of solid krypton, an excitation spectrum of spectrally and time-integrated VUV luminescence of Kr clusters (mean size N=34 atoms), [Kar93] and the electron mean free path of solid krypton [Sch76].

The probability for electron-electron scattering processes in clusters rises, when the electron mean free path decreases or the cluster diameter increases. The cluster excitation spectra demonstrate this behaviour. However, there is the problem connected with a cluster radius. For example, the radius of Kr clusters ($\sim N^{-1/3}$) is about of 10 Å in the case of N=30 atoms. At the same time, the electron mean free path in solid Kr, corresponding to the energy $E_{ion}^{N=30}+E_{ex}^{N=30} \approx 22.3$ eV, is roughly 20 Å, *i.e.* the mean free path is larger than the cluster radius. This is not ruling out the electron-electron scattering process, since the electron-electron scattering can also occur with some probability at smaller distances than the mean distance for scattering.

At first sight, the creation probability of the electronic polaron complex seems to be in-

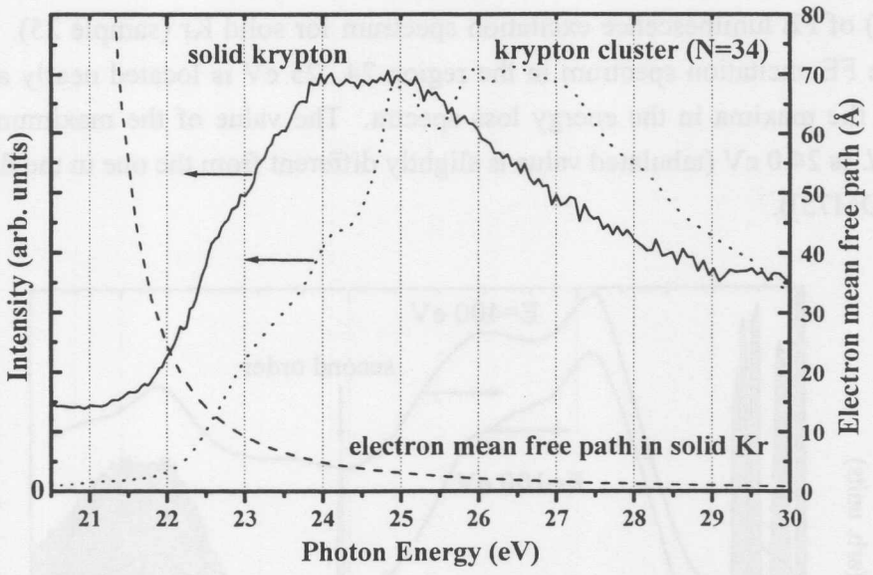

Figure 4.20: *Excitation spectrum of FE luminescence of solid Kr in the 'hot' time-window (Δt=0.94 ns, δt=0 ns) at 5 K (solid line, present work), excitation spectrum of spectrally- and time-integrated VUV luminescence of krypton clusters (mean size N=34 atoms, dotted line) [Kar93], and the electron mean free path in solid krypton (dashed line) [Sch76].*

dependent from cluster size, since both excitations are created simultaneously at the 'same' site. However, the threshold for the electronic polaron complex cannot be expected at $E_{th}=E_g+E_{ex}$ as in a solid, but at $E_{ion}^N+E_{ex}^N$. Especially, the ionization energy of the clusters E_{ion}^N depends significantly on the cluster size and for small clusters essentially exceeds E_g (*e.g.* $E_{ion}^{N=30}$ is 0.8 eV larger than E_g). It means, that the threshold energy for the creation of an electronic polaron complex in the clusters depends on the cluster size. Therefore, it is possible to explain the threshold at $E_{th}=E_g+E_{ex}$ in solid Kr and the threshold in Kr clusters at $E_{ion}^N+E_{ex}^N$ as well in the framework of the electronic polaron complex.

Summarizing previous discussion, the comparison between the photoexcitation spectra of solid Kr and Kr clusters supports both possibilities that the threshold originates from electron-electron scattering as well as from the creation of electronic-polaron complexes.

4.8.2 Electron energy loss experiments

The energy loss spectra show, how much energy electrons lose during their transit through the sample. The maximum above the threshold E_g+E_{ex}, discussed before for luminescence excitation spectra, is observable also in the electron energy-loss spectra of solid Kr [NGDM75, FS72]. Fig. 4.21 shows two energy-loss spectra for solid Kr [NGDM75] (primary electron beams with energies 100 eV and 400 eV) and the 'hot' time-window (Δt=0.94

ns, δt=0 ns) of FE luminescence excitation spectrum for solid Kr (sample 25). The maximum in the FE excitation spectrum in the region 24...25 eV is located nearly at the same position as the maxima in the energy loss spectra. The value of the maximum given by Nuttall *et al.* is 24.0 eV (tabulated value is slightly different from the one in the figure of the paper [NGDM75]).

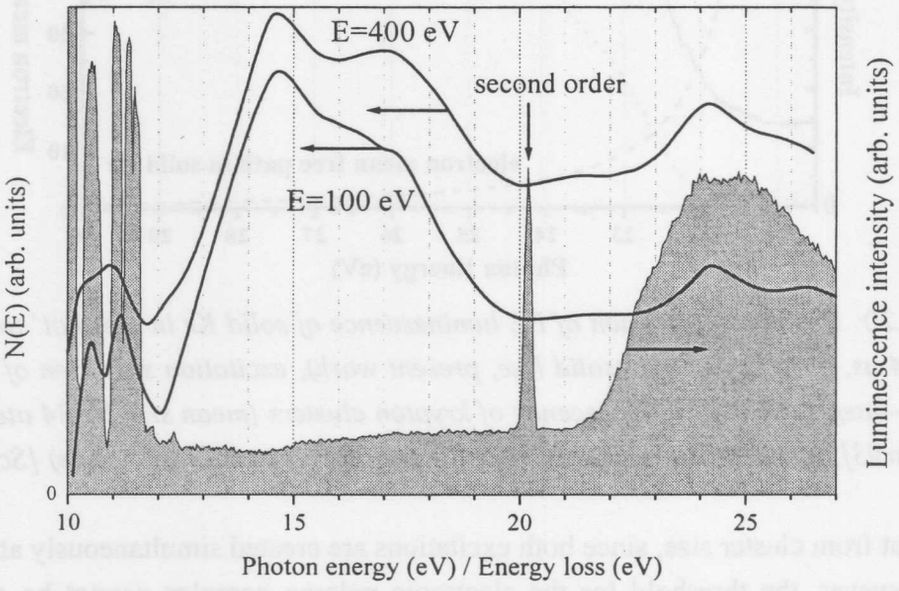

Figure 4.21: *Comparison between energy loss data [NGDM75] and the 'hot' time-window in photoexcitation spectrum of FE for solid Kr (this work). The energy loss spectra were measured with two different primary beam energies (400 eV and 100 eV) at 10 K (black solid lines). The 'hot' time-window of FE excitation spectra (δt=0 ns, Δt=0.94 ns) was recorded from sample 25 (grey area).*

Energy loss spectroscopy reveals only primary energy-losses (*i.e.* one-step processes). Therefore, above E_{th} two-step electron-electron scattering processes can not contribute to signal intensity in the energy-loss spectra. The maximum at 24.0 eV in energy loss spectra can be explained in two ways. One possibility is the creation of two excitations (*i.e.* electronic polaron complex) in a one step process. On the other hand, the maximum in the energy loss spectra may originate from a density of states effect or a variation of quantum mechanical transition matrix elements. Note, *e.g.*, the strong broad maxima at $\sim$15 eV and at $\sim$17 eV which are due to such effects [NGDM75]. In solid Xe and Ar, analogous maxima are present above $E_{th}=E_g+E_{ex}$ in the photoexcitation as well as in the energy loss spectra [Ste99, Gmi00]. It supports the creation of the electronic polaron complex, because it seems to be unlike, that a maximum in the density of the states of the conduction band has

a peculiarity slightly above E_g+E_{ex} in all three RGS.

4.8.3 Cathodoluminescence excitation spectra

In the following, a comparison between photoexcitation spectra of this work and cathodoluminescence excitation spectra will be presented. Coletti and Debever measured the intensity of the STE luminescence at 8.25 eV in solid Kr as a function of the kinetic energy of an external electron beam [CD83]. They used electrons with a kinetic energy from a few eV to 80 eV. The sample used, was a thin layer (a thickness roughly 50 Å) condensed at about 8 K.

The time-integrated STE photoexcitation spectrum and the results of Coletti and Debever are plotted in Fig. 4.22. In the original work, Coletti and Debever presented the cathodoluminescence excitation spectra in an energy scale, in which the electron energy was measured from the bottom of the conduction band [CD83]. Therefore, in Fig. 4.22, the band gap energy was added to the original curve. Even then, both curves do not have a completely correct energy scale, since in the case of photoexcitation also holes beside electrons obtain some kinetic energy (see Eq. 3.27 and 3.28). Electrons can pass through the sample only, if their energy exceeds the vacuum level energy E_g+E_A. E_A is the electron affinity (0.3 eV).

As is demonstrated in Fig. 4.22, the threshold for photoexcitation is about 2 eV **lower** than the one in electron excitation. This seems to exclude the possibility, that the threshold at E_g+E_{ex} is caused by electron-electron scattering. Taking into account the dispersion of the valence band, the threshold for electron-electron scattering in the photoexcitation spectrum should locate even at **higher energy** than in the cathodoluminescence excitation spectrum. Consequently, a comparison between photoexcitation and cathodoluminescence data supports the interpretation of the threshold at E_g+E_{ex} as the creation of electronic-polaron complex. But the electron-electron scattering contributes definitely to the maximum above the threshold.

The cathodoluminescence excitation spectrum, as discussed above, has been measured for the irregular thin layer. Hence, the cathodoluminescence spectrum, measured for the sample with 'good' crystal structure can show a slightly different behaviour as data from [CD83].

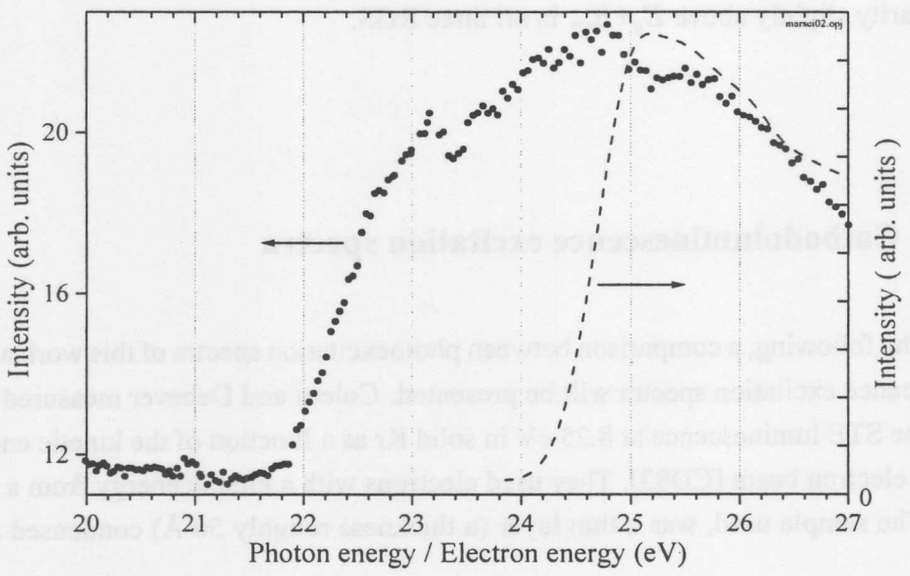

Figure 4.22: *The time-integrated photoexcitation spectrum of STE luminescence (• • •, present work) and the cathodoluminescence excitation spectrum of STE luminescence (- - -) [CD83]. In the STE photoexcitation spectrum, only the part exceeding a constant background is shown. The STE photoexcitation spectrum was measured from sample 25 (T=6 K,* $\Delta\lambda_{excit}$*=2.2 Å,* $\Delta\lambda_{lum}$*=11 Å).*

4.8.4 Conclusions

Some conclusions can be drawn from the previous sections.

- The comparison between the photoexcitation spectra of solid Kr and Kr clusters supports both possibilities, that the threshold may originate from electron-electron scattering as well as from the creation of electronic-polaron complexes.
- The comparison between the photoexcitation spectra and the energy loss spectra of solid Kr affirms that the threshold is due to the creation of the electronic-polaron complex. However, it does not exclude additional electron-electron scattering.
- The comparison of the photoexcitation spectra and the cathodoluminescence excitation spectra of solid Kr supports the idea, that the threshold is caused by the creation of an electronic-polaron complex in a one-step process, and that electron-electron scattering contributes above E_{th}.

Therefore, 'prompt' creation of excitons above E_{th} is ascribed to a superposition of both processes. At threshold itself, the creation of electronic polaron complexes is the dominant process, and at higher excitation energies, electron-electron scattering may dominate.

4.9 Results of the recombination model

In the present work, the 'slow' component of experimental FE decay curves, excited above the forbidden gap, was fitted using the electron-hole recombination model (see section 3.5.1). The fitting procedure is very sensitive regarding the initial carrier density N_0. This again depends strongly on the alignment of mirrors in the beamline as well as on the storage ring current and on the number of bunches. Also the surface quenching plays an important role, depending on the particular sample. Therefore, the numerical values obtained from model calculations for one sample cannot be used for other samples. The FE decay curves of 'good quality' sample 14 (FE/STE intensity ratio 0.84) are used as an example in this section.

The first step in the fitting process is to fix a set of initial parameters (*e.g.* $C = E_d^2 m_e^{5/2}$, N_0 , Γ_{nr}). Then, the respective FE decay curve and the difference between the 'slow' component of experimental FE decay curve and the calculated curve were computed. The difference was calculated on the basis of the least square method, using a sum

$$S = \sum_j \left(I_{\text{exp}}^j - I_{fit}^j\right)^2,$$

where I_{exp}^j is the intensity in the j-th channel of the experimental decay curve and I_{fit}^j is the corresponding calculated value.

This procedure was repeated using various sets of initial parameters. The decay curve corresponding to the smallest value of S, was accepted as the best fit. The time-region of decay curve, where the 'prompt' component dominates, was excluded from the calculations.

Similar calculations were performed for solid Xe using a one-dimensional fitting method [Ste99]. It means, that all parameters were fixed, except one which was varied during the fit. In the present work, a multi-dimensional fitting procedure was used and up to three parameters were varied during one fit. The multidimensional fit requires more time, since the number of calculated curves increases essentially.

The quantities $C{=}E_d^2 m_e^{5/2}$ and N_0 significantly affect the shape of a decay curve. The same is true for Γ_{nr} only, if $\Gamma_{nr} \gtrsim 5{\cdot}10^7$ 1/s. At first sight, it seems possible to determine values for those quantities from the model calculations. But this is not true. The model calculations of this work verified, that there is no well-defined minimum for S, *i.e.* one fixed set of parameters, giving the best fit. On the contrary, several sets of significantly different parameters can be found, which all provide a similar shape of the decay curve. Fig. 4.23 shows fitting results for three different values of the parameter $C{=}E_d^2 m_e^{5/2}$ (at fixed $\Gamma_{nr}{=}0$). The initial carrier density N_0 for every particular coefficient $C{=}0.5 \cdot C_{\text{exp}}$, $C{=}C_{\text{exp}}$ and $C{=}1.5 \cdot C_{\text{exp}}$ was found from the fit. C_{exp} is the experimental value taken from

literature, but as discussed before, it can be somewhat overestimated (see section 3.5.1). As Fig. 4.23 clearly demonstrates, a variation of the coefficient $C = E_d^2 m_e^{5/2}$ by factor of 3 changes the value for the initial carrier density N_0 50 times. At the same time, the change of the calculated FE decay curve shape is rather small. Consequently, in principle the theoretical model simulates the experimental curves sufficiently well, but especially the values of $C = E_d^2 m_e^{5/2}$ and N_0 depend very strongly on each other. Therefore, from the model calculations is not possible to find 'real' values for all three parameters $C = E_d^2 m_e^{5/2}$, N_0 and Γ_{nr}. In principle, using fitting one can find a good estimate for one quantity, but only in the case, if two others are well known.

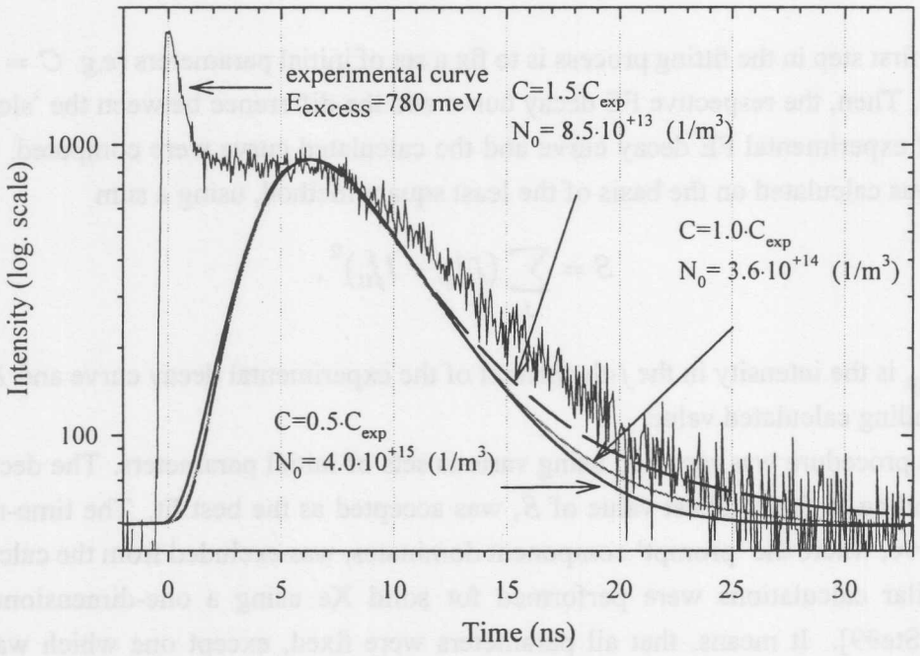

Figure 4.23: *Experimental FE decay curve ('good quality' sample 14 at 6 K, DORIS current 99 ... 93 mA) and the results of model calculations in the case of different coefficients* $C = E_d^2 m_e^{5/2}$: $C = 0.5 \cdot C_{\text{exp}}, C = C_{\text{exp}}$ *and* $C = 1.5 \cdot C_{\text{exp}}$. *The modified Abakumov's cross-section [RGK+99] was used, neglecting nonradiative losses. The respective values of the initial carrier density* N_0 *obtained from the fits are also given in the figure.*

Fig. 4.24 depicts the best possible fits using three different cross sections, *i.e.* from three different theoretical approaches (see chapter 3.5.1). N_0 is always determined from model calculations using fixed values Γ_{nr}=0 and C=C_{exp}. The cross-section $\sigma_{[RGK+99]}$ for FE creation (Eq. 3.43) gives the best accordance with experiment. This figure also demonstrates, that a change of the theoretical approximation for the cross-section causes variation of the initial carrier density N_0, found from the fit, by a factor of ~20. It is important to

remind that a serious hidden assumption concerns the use of cross-section $\sigma_{[RGK+99]}$, which is valid for *mobile* holes and electrons. For RGS, it is generally assumed that holes self-trap after their creation within pico-seconds. Therefore, the values found on the basis $\sigma_{[RGK+99]}$ are only approximate. Additional theoretical investigations, concerning the cross-section of mobile electron and localized hole recombination into FE state are necessary.

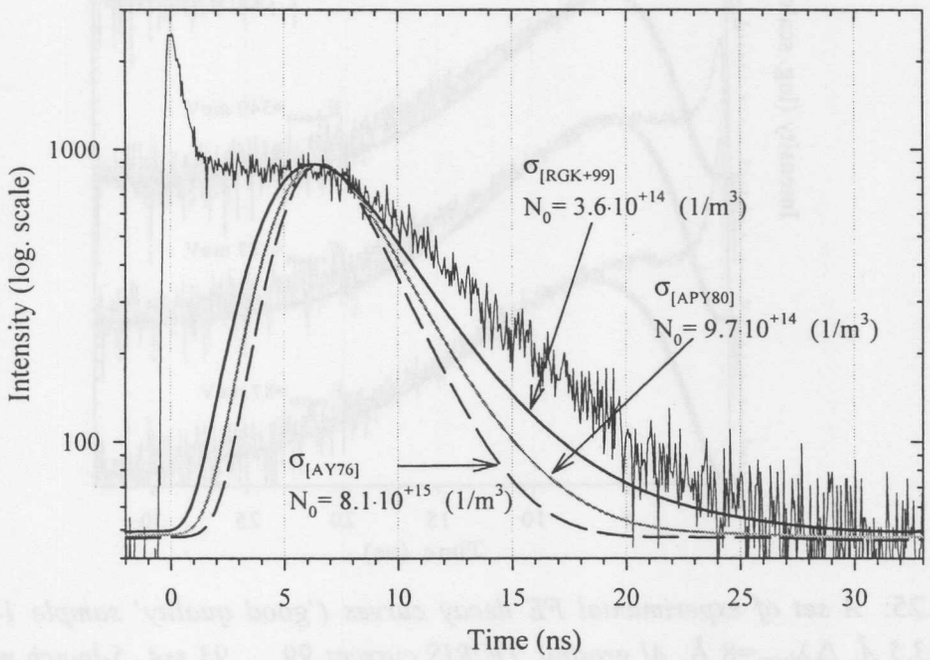

Figure 4.24: *Experimental FE decay curve ('good quality' sample 14 at 6 K, DORIS current 99 ... 93 mA, E_{excess}=780 meV) and the best fits for three different theoretical cross-sections at fixed Γ_{nr}=0 and C=$C_{\exp}$. The initial carrier densities N_0, found from the fitting, are shown in the figure as well.*

As Fig. 4.24 shows, the value of initial carrier density N_0, obtained from the fit using cross-section $\sigma_{[RGK+99]}$, is ~2000 times smaller than the density estimated for the electron-hole creation process itself. As discussed in section 3.5.1, the initial excitation volume has a thickness of the order $1/\alpha \approx 10$ nm. However, even the mean free path of the created electrons can be much longer. Plenkiewicz *et al.* estimated that the mean free path of electrons with kinetic energy ~1 eV in solid Ar is more than 200 nm [PJPP86]. Cartier and Pfluger [CP88] also estimated ~200 nm (Ar) and ~500 nm (Xe) for electrons with kinetic energy ~1 eV. No estimates exist for Kr, however, the value should be somewhere between the values for Ar and for Xe. As a consequence of the transverse size of the excitation volume (length, width $\gg 1/\alpha$), the diffusion of carriers can be treated as an one-dimensional problem. Under these particular excitation conditions, the carrier diffusion during their

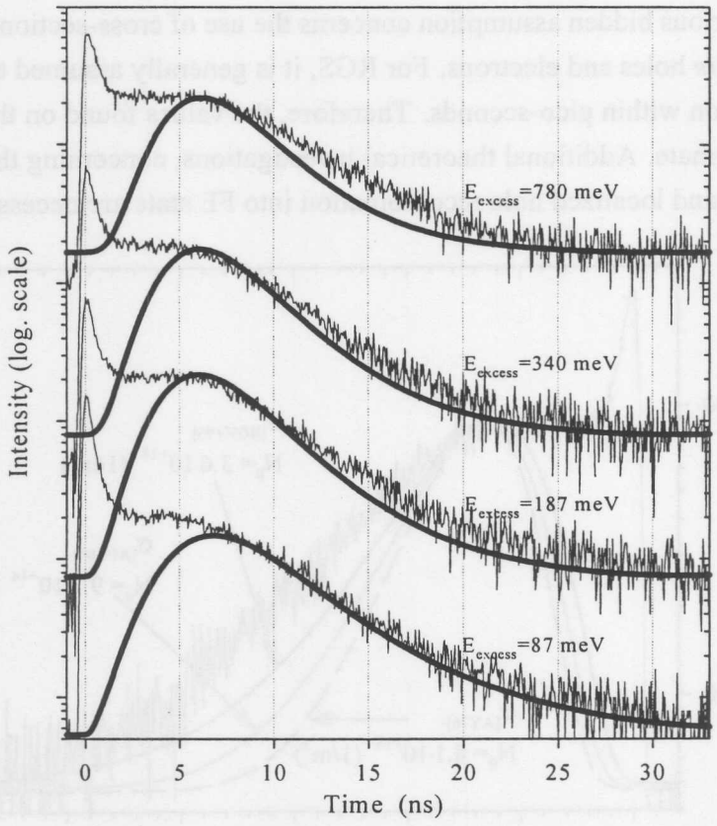

Figure 4.25: *A set of experimental FE decay curves ('good quality' sample 14 at 6K, $\Delta\lambda_{excit}$=3.5 Å, $\Delta\lambda_{lum}$=8 Å, Al grating, DORIS current 99 ... 93 mA, 5-bunch mode) together with the respective fitting results. An initial carrier density N_0=3.6·10^{14} m^{-3} was determined from the fit of the curve with the excess energy E_{excess}=780 meV. All other curves were calculated without any change in initial parameters. The modified Abakumov's cross-section was used [RGK+99] neglecting non-radiative losses.*

cooling may account for expansion of the charge cloud into the bulk of the sample, thus enlarging the excitation volume. The capture of carriers in traps and non-radiative surface quenching under the conditions of the present experiment play also a role and decrease the carrier density. Additionally, a significant problem is connected with experimental value $C_{exp} = E_d^2 m_e^{5/2}$, which can be overestimated (see section 3.5.1).

It is important to point out that experimental decay curves (see *e.g.* Fig. 4.23) demonstrates a plateau in the time-range from ~2 to ~6 ns. At the same time, this plateau is not present in the calculated decay curves. The reason is that the theory does not take into account diffusion of the charge carriers. Namely, a few nanoseconds later the carrier density is considerable reduced due to the diffusion process. Whereas the model accounts for carrier

	Unit	Value
Effective electron mass, m_e	m_0	0.42
Effective hole mass, m_h	m_0	3.6
Initial carrier density (at E_{excess}=780 meV), N_0	$1/m^3$	$3.6 \cdot 10^{14}$
$C_{exp} = E_d^2 m_e^{5/2}$	$J^2 kg^{5/2}$	$4.83 \cdot 10^{-114}$
Longitudinal sound velocity, v_l	(m/s)	1370
Crystal temperatur, T_L	(K)	5.5
Non-radiative losses, Γ_{nr}	1/s	0*
Density of solid Kr (at 5K), ρ	kg/m^3	3092.6

Table 4.7: *The values of the parameters, used for the computer simulations of the decay curves. *If the value of non-radiative losses is smaller than $\sim 5 \cdot 10^7$ 1/s, its influence on the fitting results can be neglected.*

density change caused only by recombination. Therefore, it is obvious that the rising part of the theoretical decay curves is most probably underestimated. The relevance of diffusion processes is also justified by the 'small' value of the carrier density, found as result of the fitting.

Figure 4.25 shows the experimental FE decay curves as well as the results of the model calculations at different excitation energies above the band gap. The excess energy $E_{excess}=h\nu - E_g$ is given for each curve as an energetic parameter. As discussed before (section 3.5.1), the electron-hole recombination model is applicable with an excess energy $E_{excess} \lesssim 1.5$ eV. Therefore, only curves with small excess energy are shown. The initial carrier density $N_0=3.6 \cdot 10^{14}$ m^{-3} was determined from the fit of the upper experimental curve (E_{excess}=780 meV). All other curves were calculated using the same initial carrier density N_0, corrected for the initial photon flux and the absorption coefficient at the respective excitation energies as well as for the storage ring current. The values of the parameters used for the simulations are collected in table 4.7.

The most important results of the simulations using the electron-hole recombination model are:

•The electron-hole recombination model describes quite well the shape of the 'slow' component of FE decay curve.

•Compared with earlier calculations for solid Xe [RGK+99, Ste99], the values for the electron effective mass m_e and the deformation potential E_d, based on the theoretical consid-

erations, were replaced by an experimentally determined coefficient $C_{\text{exp}} = E_d^2 m_e^{5/2}$. Such a substitution is assumed to increase the accuracy of fitting results, even if C_{exp} includes some error.

•The value of the initial carrier density N_0 from the fitting is ~2000 times smaller than estimated from the experimental conditions. The following factors play a main role here:
(i) The carrier diffusion can cause a very significant decrease of the carrier density. Namely, as a consequence of the transverse size of the excitation volume (length, width $\gg$ thickness), the diffusion of carriers can be treated as an one-dimensional problem. The initial thickness of the excitation volume is ~100 Å, but already a few diffusion steps can enlarge the excitation volume drastically (see p. 117).
(ii) The experimental value of $C_{\text{exp}} = E_d^2 m_e^{5/2}$ is probably overestimated (see section 3.5.1). As demonstrated, its increase by factor of two already causes an underestimation of the initial carrier density by more than an order of magnitude. New measurements of the low-field electron mobility at low temperature in 'good quality' samples are necessary to improve the value of $C_{\text{exp}} = E_d^2 m_e^{5/2}$.
(iii) It is possible that the cross-section $\sigma_{[RGK+99]}$ includes some inaccuracy. More detailed theoretical investigations concerning the recombination cross-section are necessary.
(iv) The incident photon flux may be considerably overestimated.

4.10 Irradiation effects

Ionizing radiation has considerable influence on the optical properties of wide-gap solids. During experiments with solid krypton, irradiation effects were observed as well. Namely, if the monochromatized synchrotron radiation spot was directed to a 'fresh' position of the sample, the 'slow' component of the FE decay curve increased during the first 5 ... 15 min of irradiation. 'Fresh' means that the sample surface has never been illuminated by synchrotron radiation earlier.

This behaviour may be explained in the following way. Concerning recombination, there exist two possibilities, (i) recombination of free electrons and free holes, and (ii) recombination of free electrons and self-trapped holes. It is important to remind that self-trapping of the holes occurs on a time-scale of a few ps.

As was shown by Kink *et al.* [KKK+97] electrons can be trapped in RGS as well. The traps established by Kink *et al.* in solid Kr are deep traps (with the depths of 43, 60, 69, 82 meV) so that the trapped electrons are lost for recombination. However, there is a fundamental difference between hole trapping and electron trapping. Self-trapping of holes is an intrinsic effect, whereas electron trapping is an extrinsic effect, requiring already

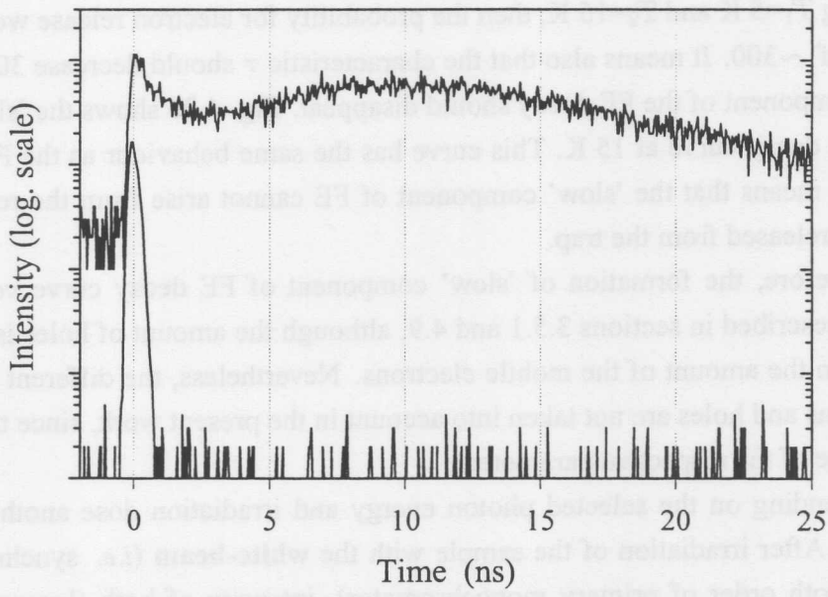

Figure 4.26: *FE decay curve (sample 16 at 15 K, $\Delta\lambda_{excit}$=2.6 Å, $\Delta\lambda_{lum}$=7 Å) excited by 21.0 eV photons.*

present impurities (like oxygen) or structural defects. Therefore, after a certain dose of illumination, the extrinsic trapping sites may be saturated. That means, after saturation, more mobile electrons are present for recombination than in a 'fresh' sample. Moreover, the (self-trapped) holes corresponding to the trapped electrons, are still ready to recombine with mobile electrons.

Although traps play a distinct role in the decay kinetics of luminescence, those decays are not trap controlled in the usual sense, where the shape of the decay curve arises from the probability of electron escape from the trap. The electron probability to escape from a trap is given by

$$p(T) = \frac{1}{\tau} = s \cdot \exp\left(-\frac{E_{tr}}{k_B T}\right), \tag{4.4}$$

where s is the frequency factor of the order of a phonon frequency, τ is the characteristic time for electron release, and E_{tr} is the energetic depth of the trap. A rough value for the frequency factor in solid Kr is $s \sim 10^{12}$ 1/s [KV76]. Assuming that the 'slow' component of FE decay curves is caused by traps, then a typical τ for such traps should be roughly $\tau \sim 5$ ns at 5 K. A typical depth of such trap should be $E_{tr} \sim 4$ meV (from Eq. 4.4). An increase of sample temperature from T_1 to T_2 then would increase the probability for electrons to be released from the traps,

$$p(T_2)/p(T_1) = \exp\left(-\frac{E_{tr}}{k_B T_2}\right) / \exp\left(-\frac{E_{tr}}{k_B T_1}\right) = \exp\left(\frac{E_{tr}}{k_B}\frac{T_2 - T_1}{T_2 \cdot T_1}\right). \tag{4.5}$$

Assuming T_1=5 K and T_2=15 K, then the probability for electron release would increase by a factor of ~300. It means also that the characteristic τ should decrease 300 times and the 'slow' component of the FE decay should disappear. Fig. 4.26 shows the 'slow' component of the FE decay curve at 15 K. This curve has the same behaviour as the FE decay curves at 5 K. It means that the 'slow' component of FE cannot arise from the recombination of electrons released from the trap.

Therefore, the formation of 'slow' component of FE decay curve very likely takes place as described in sections 3.5.1 and 4.9, although the amount of holes is most probably larger than the amount of the mobile electrons. Nevertheless, the different initial densities of electrons and holes are not taken into account in the present work, since this needs better knowledge of the respective parameters.

Depending on the selected photon energy and irradiation dose another effect is observable. After irradiation of the sample with the **white-beam** (*i.e.* synchrotron radiation in the zeroth order of primary monochromator), intensity of both ('prompt' and 'slow') components of FE decay curve decreases (Fig. 4.27). Such a strong irradiation influences essentially the crystal structure of the sample. A significant increase of the amount of the defects causes an enhancement of the probability of FE trapping at perturbed sites, while the probability for the radiative decay of FE does not change. As a result, the total intensity of the FE emission decreases (see section 3.4.1). However, such an interpretation is tentative and additional investigations are needed.

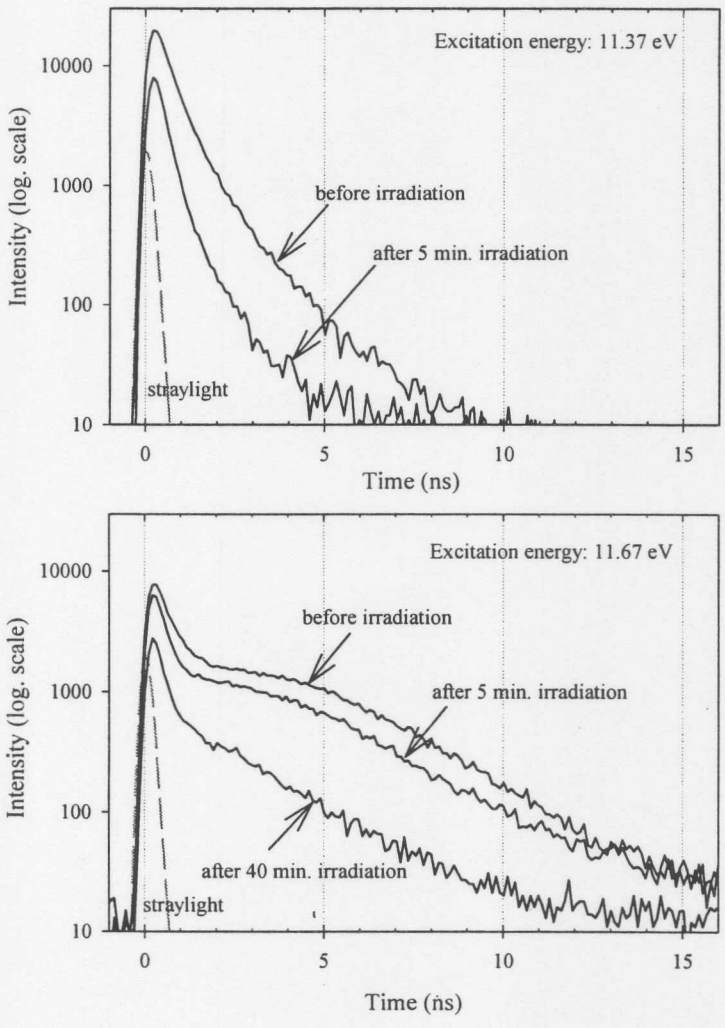

Figure 4.27: *Irradiation effects on the shape of FE decay curve under irradiation by the 'white beam' (i.e. with zero order of primary monochromator). On top: FE decay curve, excited below the forbidden gap. Bottom: FE decay curve, excited above the forbidden gap. Intensities of the curves are shown as measured in order to demonstrate the decrease of the total intensity of FE emission.*

Chapter 5

Summary

Kr crystals exhibit simultaneously strong broad-band self-trapped exciton (STE) luminescence as well as considerable narrow-band luminescence of free excitons (FE) in VUV region. The main purpose of the present work was an investigation of the different exciton creation processes in the case of photoexcitation, where the photon energy is exceeding the band gap energy. Both, narrow-band luminescence from the lowest FE state and the singlet ($^1\Sigma_u^+$) component of the STE emission were used as probes.

For the first time, the time-resolved excitation spectra of FE luminescence in solid Kr were measured using photoexcitation up to ~35 eV. Also the FE luminescence decay curves were systematically investigated in the energy range up to ~35 eV in this work. Such measurements were possible due to the intense FE emission, connected with very good 'quality' of the samples and using Kr gas with very high purity. Series of samples were grown and investigated demonstrating a good reproducibility of the main experimental results.

Delayed creation of excitons via electron-hole recombination and 'prompt' (in the meaning of the time-resolution of experimental set-up) creation of excitons were clearly separated using the time-resolved experimental technique. If the exciting photon energy is smaller than the band gap, $h\nu < E_g$ (E_g=11.59 eV), direct optical creation of excitons occurs. After their creation, excitons relax 'promptly' to the lowest FE state and then emit the FE emission or become self-trapped. Using primary excitation energy exceeding the forbidden gap energy ($h\nu > E_g$), *i.e.* creating electron-hole pairs, the FE decay curve exhibits besides the 'prompt' component (maximum is conforming with the excitation pulse) also a 'slow' component with an additional delayed maximum.

A detailed model for the dynamics of electron-hole recombination into the FE state was developed. This model includes (i) thermalization via scattering on acoustic phonons and (ii) recombination cross-section which depends on the actual carrier temperatures. In ear-

lier calculations for solid Xe [RGK+99], the values for the electron effective mass m_e and the deformation potential E_d were based on theoretical considerations. But in this work, these values were derived from the experimental value of the low-field electron mobility [MHS68]. This permitted to reduce the number of fitting parameters. The delayed component of FE decay curves was reproduced with model calculations for excess energies up to $\sim$1.5 eV. A reasonable agreement between experiment and theory was found.

In time-resolved excitation spectra, it was experimentally shown that beside the excitonic region 'prompt' creation of FE takes place in the region above the threshold $h\nu = E_{th} \approx$21.7 eV. Also the shape of the decay curves changes significantly above this threshold. The experimental threshold value is nearly equal to the sum of the band gap energy and the free exciton energy (E_{th}=E_g+E_{ex}). 'Prompt' creation of excitons above E_{th} is ascribed to a superposition of two processes: (i) inelastic scattering of the electrons in the framework of the multiple-parabolic-branch band model (two-step process) and (ii) creation of the electronic polaron complex (one-step process). At threshold itself, the creation of the electronic polaron complex is the dominant process, and at higher excitation energies, electron-electron scattering may prevail. In particular, a comparison of experimental data of the present work and cathodoluminescence data of Coletti and Debever [CD83] supports such a conclusion.

In general, Kr gas contains a Xe impurity, causing the appearance of the Xe-connected emission bands. Some of them overlap with the STE luminescence band of Kr, complicating significantly luminescence analysis. In this work, due to the practically Xe-free Kr gas, the 'pure' STE luminescence band of solid Kr was observed for the first time.

Also, time-resolved excitation spectra of STE luminescence of 'good quality' Xe-free samples were measured for the first time. The smooth behaviour of the FE/STE ratio spectra above the band gap strongly supports the idea that the STE originating from electron-hole recombination has FE states as precursors. In other words, recombination leads to the creation of free excitons which then either decay radiatively or get localized into the STE state.

The influence of the sample 'quality' on the shape and on the location of the STE band was observed directly using 'good quality' (homogeneous sample with relatively big crystallites and small amount of as grown defects) and 'snow-like' (sample consisting of tiny crystallites and looking like snow in visual observation) Xe-free samples. It was clearly demonstrated that the defects in the crystal induce a red shift of the STE luminescence band. This behaviour is known for other RGS as well.

Besides luminescence measurements, new high-resolution reflection measurements were performed in the present work. Due to the good 'quality' of the samples and excellent vacuum conditions, especially important for the reflection measurements, a new member of the

exciton series (n=5) was revealed. On the basis of high-resolution reflection measurements, more accurate values of several parameters concerning excitons in solid Kr (reduced mass of the exciton, binding energy of exciton *etc.*) were determined.

Additionally, a decomposition of the luminescence bands of Xe-doped solid Kr into three different sub-bands is shown in appendix A. For the first time, the time-resolved excitation spectra of the Xe impurity luminescence peaked at ~9.7 eV and decay kinetics of the same emission were investigated.

Appendix A

Xenon-doped krypton

The investigation of Xe-doped solid Kr was not the main purpose of the present work, but a comparison was made to reveal Xe impurity connected effects and to distinguish from those due to the intrinsic luminescence of pure solid Kr. Such data are also interesting for luminescence spectroscopy and therefore, experimental results are presented here, but without any profound analysis. All results presented in this appendix were measured for the sample 31 (~30 ppm Xe). Accordingly, the following discussion is based on self-consistent data.

As it was mentioned before, solid Kr has not been as popular as solid Xe concerning the investigation of intrinsic luminescence phenomena. One of the reasons is the fact that a Xe impurity, which is always present in 'nominally pure' Kr gas, complicates the investigation of the intrinsic luminescence of solid Kr. On the other hand, several studies have been performed dealing with luminescence of Xe-doped Kr in the solid and in the liquid phase [LGM$^+$89, BKP$^+$86, KG91, Laa92, Var94, CRJ73]. More is known about the (XeKr)* excimer centre in a Kr matrix, but the luminescence connected with the atomic Xe centre in Kr is less well studied.

The STE emission band of 'good quality' solid Kr samples with the highest purity available has a gaussian-like line shape, and the deviations from this shape are due to the site effects and luminescence arising from the different vibrational levels (see section 4.3). On the contrary, the luminescence band of Xe-doped samples shows a strongly asymmetric shape in the same region (see Fig. 4.1). This happens, since besides the STE of krypton, (XeKr)* and Xe_2^* centres, as well as atomic centres of the Xe impurity contribute to the broad luminescence band. The Xe-connected bands strongly overlap with the intrinsic STE luminescence band of Kr. A collection of literature data about Xe-related emission bands near the STE band in solid Kr is shown in table A.1.

The emission of the (XeKr)* centre was identified by Nowak and Fricke, who bom-

Band origin	Reference	Position (eV)	FWHM (meV)	Excitation
(XeKr)*	[NF85]	7.95	280	$Xe(^3P_2)^\dagger$
	[Laa92]	7.92	370	$h\nu$=9.79 eV
	[KG91]	7.98	440	$h\nu$=9.0 eV
(XeKr)*	[Laa92]	8.33	380	$h\nu$=9.95 eV
	[Var94]	8.37	420	$h\nu$=10.05 eV
$Xe(^3P_1)$	[Var94]	$8.58^{\dagger\dagger\dagger}$	$89^{\dagger\dagger\dagger}$	$h\nu$=10.05 eV
	[Laa92]	$8.46^\ddagger$	$55^\ddagger$	$h\nu$=8.99 eV
$Xe(^3P_1)$	[Var94]	$8.67^{\dagger\dagger\dagger}$	$92^{\dagger\dagger\dagger}$	$h\nu$=10.05 eV
	[Laa92]	8.68	$100^{\dagger\dagger}$	$h\nu$=8.99 eV

Table A.1: *A collection of experimental data for the Xe-connected luminescence bands in solid Kr. Data of different luminescence bands are separated with double lines.* †*Bombardment with excited Xe atoms.* ††*The width of this band depends strongly on excitation energy.* †††*Results of a deconvolution.* ‡*Very weak band.*

barded solid krypton with Xe atoms in the metastable $^3P_2$ state [NF85]. They found that due to the (XeKr)* centre an emission band arises with a maximum at 7.95 eV and a FWHM 280 meV. Laasch studied the luminescence of Xe-doped Kr at different exciting photon energies below the FE energy in solid Kr [Laa92] and obtained similar results (see table A.1). However, in the same work it was shown, that photoexcitation with 9.95 eV photons leads to the appearance of a new strong band at 8.33 eV. The same band was observed by Varding as well (see table A.1). Laasch classified this band as the STE luminescence of solid Kr, whereas Varding assigned it to the (XeKr)* centre. Taking into account the results of the present work, the latter interpretation seems to be more realistic.

A comparison between the luminescence spectra of Xe-doped and nominally pure Kr samples demonstrates clearly that additional Xe-connected sub-band(s) exist(s) also in the region 8.5 .... 8.8 eV (see Fig. 4.1). However, the literature data about this region are rather poor. Only in the case of excitation below excitonic region of Kr, Laasch [Laa92] was able to separate a luminescence band with the maximum at 8.68 eV and a very weak band peaking at 8.46 eV. In that work these bands were interpreted as luminescence of the Xe $^3P_1$ centre at two different lattice sites [Laa92].

Fig. A.1 shows the broad-band luminescence of Xe-doped solid Kr and its separation into different sub-bands. In the present work, only three gaussians were used for the decomposition, corresponding to the Kr STE band (maximum at 8.58 eV, FWHM 300 meV), to the

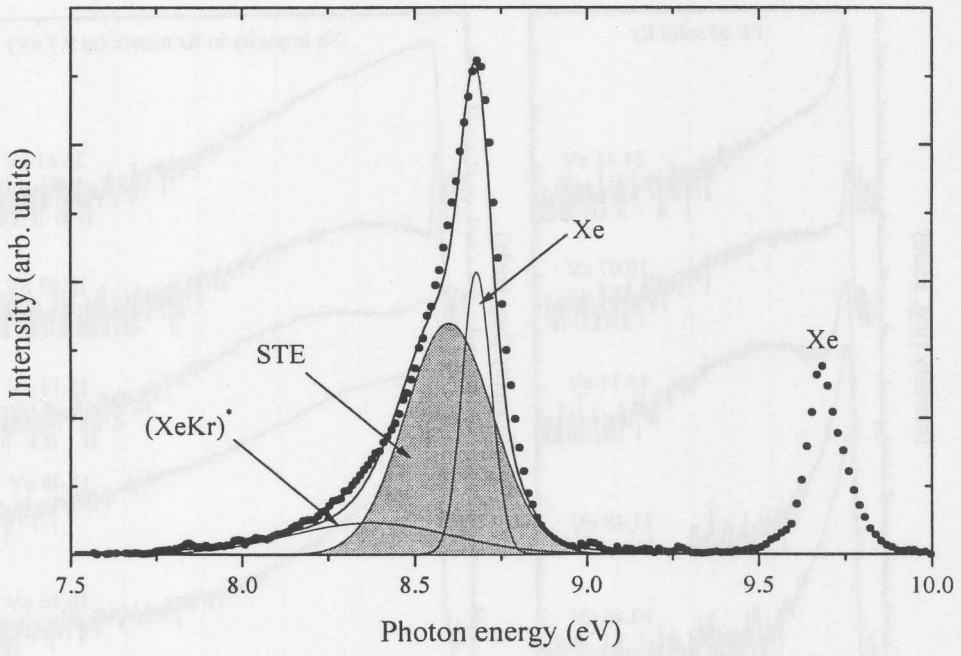

Figure A.1: *Luminescence spectrum of Xe-doped (~30 ppm) solid Kr at 6 K (• • •, sample 31). A decomposition into three gaussians and a sum of these gaussians are also shown (solid lines). Luminescence was excited by 10.42 eV photons* ($\Delta\lambda_{exc}$=3.3 Å) *and measured with the high-flux VUV-1 monochromator (resolution* $\Delta\lambda_{lum}$=*12 Å).*

(XeKr)* excimer band (maximum at 8.37 eV, FWHM 550 meV) and to the luminescence originating from the Xe $^3P_1$ state (maximum at 8.68 eV, FWHM 100 meV), respectively. This decomposition is not a fit in the usual sense, since all the energetic positions of the Xe-connected sub-bands were taken from earlier studies [Laa92, Var94]. The parameters of the Kr STE luminescence band were taken from the results of the present work (see table 4.1). The widths of the sub-bands were varied, starting from the values given in table A.1. The widths were reproduced quite well with one exception, namely the width of the (XeKr)* excimer. The relative intensities were the only completely free parameters. As a result, the sum of the three sub-bands coincides satisfactory with the experimentally observed luminescence band.

The decomposition shown in Fig. A.1, is different from that of by Varding [Var94]. In the region 8.5 .... 8.8 eV, Varding used not one, but two gaussians with *comparable intensities* and maxima located at 8.58 eV and 8.67 eV, respectively (see table A.1). An inclusion of the additional band peaking at 8.58 eV was based on the fact that Laasch [Laa92] observed an *extremely weak* band at 8.46 eV. Therefore, the author of the present work has the opinion, that using two gaussians with *comparable intensities,* but different positions of maxima representing the Xe $^3P_1$ luminescence in Kr matrix is not justified. Of course, it

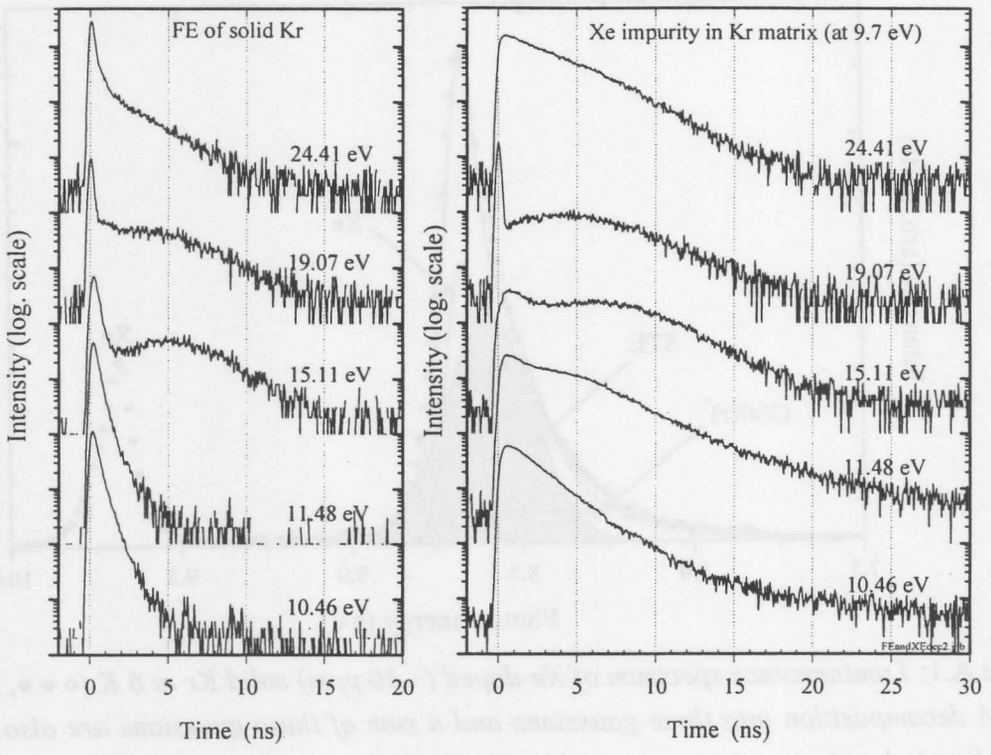

Figure A.2: *Decay curves of the Kr FE luminescence band (10.14 eV) as well as of the Xe-connected band (9.7 eV) in a Xe-doped (~30 ppm) solid Kr sample at various excitation energies (sample 31, T=5 K, $\Delta\lambda_{exc}$=3.3 Å, $\Delta\lambda_{lum}$=12.5 Å). The excitation energies are shown in the figure. Time t=0 corresponds to the maximum signal intensity of the excitation pulse.*

gives a better fit in the 'mathematical sense'.

Additionally, the luminescence spectrum shows a strong Xe-connected band with its maximum at ~9.7 eV. A detailed high-resolution investigation showed [Var94] that it consist of a 'strong' sub-band (maximum at 9.70 eV) and a 'weak' sub-band (maximum at 9.66 eV). The band at 9.70 eV is probably connected with the Xe $^1P_1$ state [Var94], whereas the origin of the band at 9.66 eV remains unknown.

Fig. A.2 shows the decay curves of the Kr FE luminescence and of the Xe $^1P_1$ band at ~9.7 eV at different exciting photon energies. It seems reasonable that the excitation of the Xe band at ~9.7 eV occurs mainly via energy transfer by FE of Kr to the impurity. This is in good agreement with luminescence experiments. Namely, if the Xe-luminescence band at ~9.7 eV is observable in luminescence, then the intensity of the Kr FE luminescence band is extremely weak or even absent. The time-behaviour of ~9.7 eV luminescence band is probably governed by the time-behaviour of FE band and by the lifetime of Xe-centre.

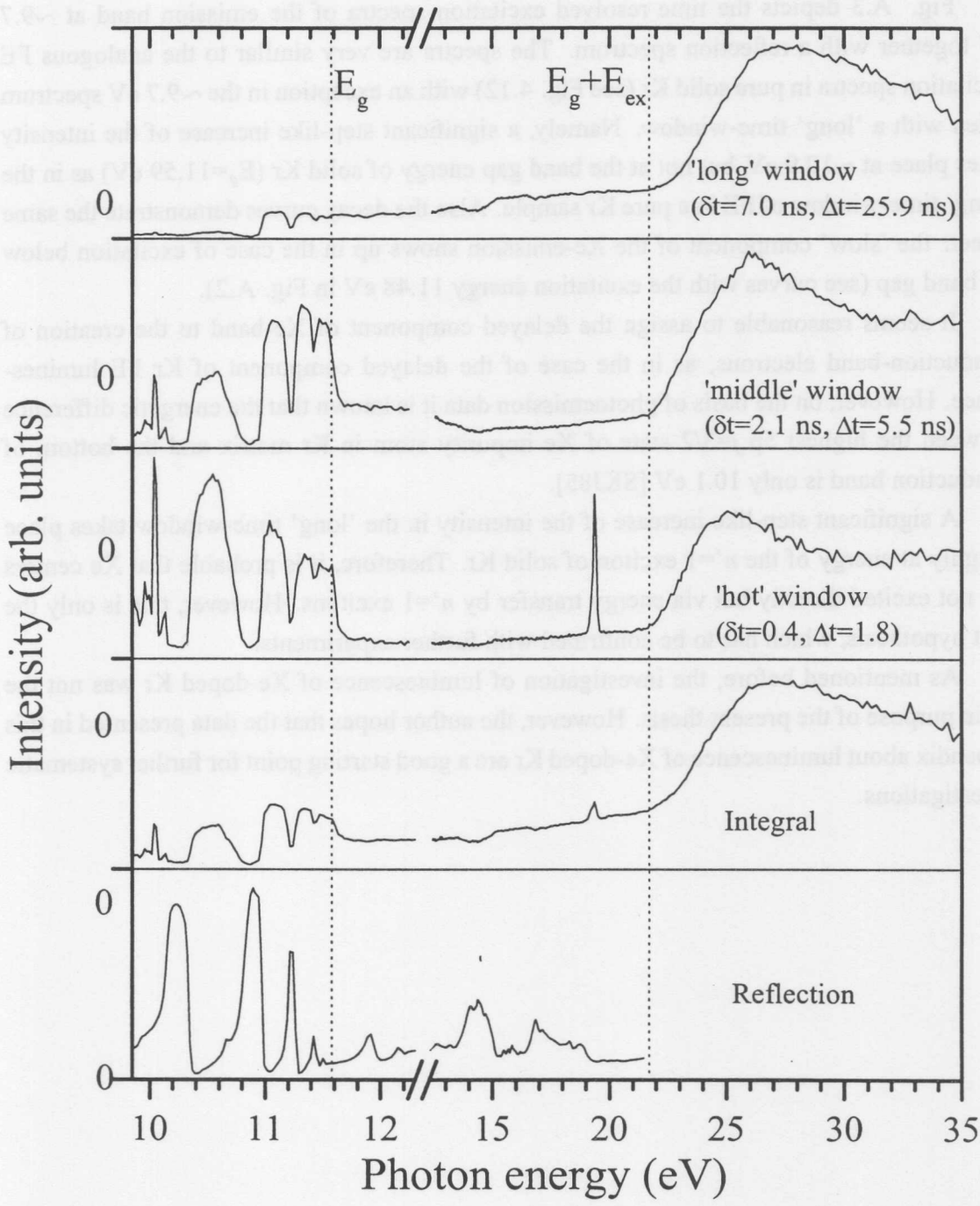

Figure A.3: *Time-integrated and time-resolved excitation spectra of the Xe impurity (~30 ppm) luminescence at ~9.7 eV in a Kr matrix (sample 31, T=5 K, $\Delta\lambda_{exc}$=3.3 Å, $\Delta\lambda_{lum}$=12.5 Å). The reflection spectrum is also shown. The sharp peaks at ~19 eV, pronounced in the 'hot' time-window and integral spectra, are caused by the second order of the secondary monochromator. The parameters of the time-windows are denoted in the figure.*

Fig. A.3 depicts the time-resolved excitation spectra of the emission band at ~9.7 eV together with a reflection spectrum. The spectra are very similar to the analogous FE excitation spectra in pure solid Kr (see Fig. 4.12) with an exception in the ~9.7 eV spectrum taken with a 'long' time-window. Namely, a significant step-like increase of the intensity takes place at ~10.9 eV, but not at the band gap energy of solid Kr (E_g=11.59 eV) as in the 'long' time-window of FE in a pure Kr sample. Also the decay curves demonstrate the same effect: the 'slow' component of the Xe-emission shows up in the case of excitation below Kr band gap (see curves with the excitation energy 11.48 eV in Fig. A.2).

It seems reasonable to assign the delayed component of Xe-band to the creation of conduction-band electrons, as in the case of the delayed component of Kr FE luminescence. However, on the basis of photoemission data it is known that the energetic difference between the highest 5p j=3/2 state of Xe impurity atom in Kr matrix and the bottom of conduction band is only 10.1 eV [SKJ85].

A significant step-like increase of the intensity in the 'long' time-window takes place roughly at energy of the n'=1 exciton of solid Kr. Therefore, it is probable that Xe centers are not excited directly but via energy transfer by n'=1 excitons. However, this is only the first hypothesis, which has to be confirmed with further experiments.

As mentioned before, the investigation of luminescence of Xe-doped Kr was not the main purpose of the present thesis. However, the author hopes that the data presented in this appendix about luminescence of Xe-doped Kr are a good starting point for further systematic investigations.

Appendix B

Analytical solution for electron temperature

This appendix shows, how an analytical solution for the effective electron temperature as a function of time, $T_e(t)$, was found. The averaged energy loss rate per electron (hole) in the case of Maxwellian distribution and effective temperature T_e (T_h) is given by

$$\left\langle \frac{dE_{e,h}}{dt} \right\rangle_{ac} = -\frac{8\sqrt{2}E_d^2 m_{e,h}^{5/2}}{\pi^{3/2}\hbar^4\rho}(k_B T_{e,h})^{3/2}\left(\frac{T_{e,h}-T_L}{T_{e,h}}\right) \quad \text{[Con67]}. \tag{B.1}$$

The relation between the electron energy, $E_e(t)$, and the effective electron temperature, $T_e(t)$, is

$$T_e(t) = \frac{2}{3k_B}E_e(t). \tag{B.2}$$

After replacing the energy $E_e(t)$ in equation B.1 by the electron temperature, the differential equation has the form

$$\frac{dT_e(t)}{dt} = -\frac{16\sqrt{2}E_d^2 m_e^{5/2}\sqrt{k_B}}{3\pi^{3/2}\hbar^4\rho}\sqrt{T_e}\,(T_e - T_L)\,. \tag{B.3}$$

Substituting all constants by A, this equation reads

$$\frac{dT_e(t)}{dt} = -A\sqrt{T_e}\,(T_e - T_L)\,. \tag{B.4}$$

Now it is necessary to solve the integral equation

$$\int_{T_0}^{T_e} \frac{dT_e(t)}{\sqrt{T_e}\,(T_e - T_L)} = -A\int_0^t dt, \tag{B.5}$$

where T_0 is the initial electron temperature at time $t = 0$ and T_e is the electron temperature at time t. The integral has the analytical solution [Rad97]

$$\frac{1}{\sqrt{T_L}} \ln\left(\frac{\sqrt{T_e} - \sqrt{T_L}}{\sqrt{T_e} + \sqrt{T_L}}\right)_{T_0}^{T_e} = -At. \tag{B.6}$$

After inserting T_0 and T_e, we obtain

$$\frac{1}{\sqrt{T_L}} \ln\left(\frac{\sqrt{T_e} - \sqrt{T_L}}{\sqrt{T_e} + \sqrt{T_L}}\right) - \frac{1}{\sqrt{T_L}} \ln\left(\frac{\sqrt{T_0} - \sqrt{T_L}}{\sqrt{T_0} + \sqrt{T_L}}\right) = -At. \tag{B.7}$$

After some simple modifications, it is possible to find the direct expression for the electron temperature:

$$\ln\left(\frac{\sqrt{T_e} - \sqrt{T_L}}{\sqrt{T_e} + \sqrt{T_L}}\right) = -At\sqrt{T_L} + \ln\left(\frac{\sqrt{T_0} - \sqrt{T_L}}{\sqrt{T_0} + \sqrt{T_L}}\right), \tag{B.8}$$

$$\sqrt{T_e} - \sqrt{T_L} = \left(\sqrt{T_e} + \sqrt{T_L}\right) \exp\left(-At\sqrt{T_L} + \ln\left(\frac{\sqrt{T_0} - \sqrt{T_L}}{\sqrt{T_0} + \sqrt{T_L}}\right)\right), \tag{B.9}$$

$$\sqrt{T_e} = \sqrt{T_L} \frac{1 + \exp\left(-At\sqrt{T_L} + \ln\left(\frac{\sqrt{T_0} - \sqrt{T_L}}{\sqrt{T_0} + \sqrt{T_L}}\right)\right)}{1 - \exp\left(-At\sqrt{T_L} + \ln\left(\frac{\sqrt{T_0} - \sqrt{T_L}}{\sqrt{T_0} + \sqrt{T_L}}\right)\right)}. \tag{B.10}$$

Therefore, the analytical solution for the electron temperature in the framework of the used model is

$$T_e(t) = T_L \left[\frac{1 + \exp\left(-At\sqrt{T_L} + \frac{1}{\sqrt{T_0}} \ln\left(\frac{\sqrt{T_0} - \sqrt{T_L}}{\sqrt{T_0} + \sqrt{T_L}}\right)\right)}{1 - \exp\left(-At\sqrt{T_L} + \frac{1}{\sqrt{T_0}} \ln\left(\frac{\sqrt{T_0} - \sqrt{T_L}}{\sqrt{T_0} + \sqrt{T_L}}\right)\right)}\right]^2. \tag{B.11}$$

List of Figures

List of Tables

Bibliography

[And89] H.L. Anderson, editor. *A Physicist's Desk Reference*. American Institute of Physics, 1989.

[APY80] V.N. Abakumov, V.I. Perel', and I.N. Yassievich. Binding of electrons and holes into excitons. *Soviet Physics - JETP*, 51(3):626, 1980.

[AS91] E. Audouard and F. Spiegelmann. Theoretical Study of the Excited States of the Kr_2^* Excimer: Potential Curves Including Ab Initio Spin-Orbit Coupling. *The Journal of Chemical Physics*, 94(9):6102, 1991.

[Asc89] G. Ascarelli. Hall Mobility of Electrons in Liquid and Solid Argon. *Physical Review B*, 40(3):1871, 1989.

[AY76] V.N. Abakumov and I.N. Yassievich. Cross section for recombination of an electron with a positively charged center in a semiconductor. *Soviet Physics - JETP*, 44(2):345, 1976.

[Bal62] G. Baldini. Ultraviolet Absorption of Solid Argon, Krypton, and Xenon. *Physical Review*, 128(4):1562, 1962.

[BBC+74] A. Bonnot, A.M. Bonnot, F. Coletti, J.M. Debever, and J. Hanus. Luminescence des gaz rares solides excité par bombardement électronique. *Journal de Physique*, 35:C3, 1974.

[Bec97] J. Becker. *Lumineszenzspektroskopische Untersuchung der intrinsischen Emission von BaF_2 und der Energietransfer-Prozesse in $BaF_2 : Dy$*. Dissertation, Universität Hamburg, Hamburg, 1997. (DESY-THESIS-1998-037).

[BKM+96] S. Bar-Ad, P. Kner, M.V. Marquezini, D.S. Chemla, and K. El Sayed. Carrier Dynamics in the Quantum Kinetic Regime. *Physical Review Letters*, 77(15):3177, 1996.

[BKP+86] A.G. Belov, A.D. Klementov, S.A. Pendyur, I.Ya. Fugol, and E.M. Yurtaeva. Spectroscopic Study of the Eximer State of the Kr-Xe System. *Opt. Spectrosc.*, 61(5):601, 1986.

[BPCS84] G. Bader, G. Perluzzo, L.G. Caron, and L. Sanche. Structural-Order Effects in Low-Energy Electron Transmission Spectra of Condensed Ar, Kr, Xe, N_2, CO, and O_2. *Physical Review B*, 30(1):78, 1984.

[BPP88] N.C. Bacalis, D.A. Papaconstantopoulos, and W.E. Pickett. Systematic Calculations of the Band Structures of the Rare-Gas Crystals Neon, Argon, Krypton, and Xenon. *Physical Review B*, 38(9):6218, 1988.

[BTB72] P.A. Bezuglyi, L.M. Tarasenko, and O.I. Baryshevskii. Sound Velocity and Elastic Properties of Polycrystalline Krypton and Xenon. *Soviet Physics - Solid State*, 13(8):2003, 1972.

[BWS87] K. Barzein, P. Wollenweber, and H. Schmoranzer. Empirical Determination of the Potential Curves of the Ground State and the First Two Excited States of Kr_2. *Chemical Physics Letters*, 142(1,2):79, 1987.

[CD83] F. Coletti and J.M. Debever. Cathodoluminescence excitation spectra of solid rare gases. *Solid State Communications*, 47(1):47, 1983.

[CG90] M. Casabloni and U. Grassano. Applications of Synchrotron Radiation in Defect and Color Center Research. *Journal of Physics and Chemistry of Solids*, 51(7):805, 1990.

[Con67] E.M. Conwell. *High Field Transport in Semiconductors*, volume 9 of *Solid State Physics*. Academic Press, New York and London, 1967.

[CP88] E. Cartier and P. Pfluger. Experimental Determination of Energy Dependent Inelastic and Elastic Scattering Rates of Hot Electrons in Large Bandgap Insulators. *Physica Scripta*, T23:235, 1988.

[CRJ73] O. Cheshnovsky, B. Raz, and J. Jortner. Emission spectra of xenon impurity states in solid and liquid krypton. *The Journal of Chemical Physics*, 59(10):5554, 1973.

[Dav76] A.S. Davydov. *Teoriya tverdogo tela*. Nauka, Moskva, 1976.

[DK65] D.L. Dexter and R.S. Knox. *Excitons*. John Wiley & Sons, New York, 1965.

[DKC72] J.T. Devreese, A.B. Kunz, and T.C. Collins. A Resonance of the Electronic Polaron Appearing in the Optical Absorption of Alkali Halides. *Solid State Communications*, 11:673, 1972.

[Dru71] S.D. Druger. Vacancy-Limited Electron Transport in Rare-Gas Solids. *The Journal of Chemical Physics*, 54(6):2339, 1971.

[EGLP47] F.R. Elder, A.M. Gurewitsch, R.V. Langmuir, and H.C. Pollock. *Physical Review*, 71:829, 1947.

[FBYS86] I.Ya. Fugol', A.G. Belov, E.M. Yurtaeva, and V.N. Svishchev. Exciton kinetics in xenon–krypton cryocrystals. *Sov. J. Low Temp. Phys.*, 12(1):39, 1986.

[FGS82] I.Ya. Fugol', O.N. Grigorashchenko, and E.V. Savchenko. Polariton and Spatial Dispersion Effects in Exciton Spectra of Xenon Cryocrystals. *physica status solidi (b)*, 111(1):397, 1982.

[FJ91] C. Ferradini and J.-P. Jay-Gerin, editors. *Excess Electrons in Dielectric Media*. CRC Press, 1991.

[Fow63] W.B. Fowler. Electronic Band Structure and Wannier Exciton States in Solid Krypton. *Physical Review*, 132(4):1591, 1963.

[Fre31] J.A. Frenkel. On the Transformation of Light into Heat in Solids. II. *Physical Review*, 37:1276, 1931.

[FS72] H.H. Farrell and M. Strongin. Scattering of Low-Energy Electrons from Rare-Gas Crystals Grown on the (100) Face of Nb. II. Inelastic Scattering and Energy-Loss Spectra. *Physical Review B*, 6(12):4711, 1972.

[FSOG93] I.Ya. Fugol', E.V. Savchenko, A.N. Ogurtsov, and O.N. Grigorashchenko. Electronically induced changes in structural properties of solid Kr. *Physica B*, 190:347, 1993.

[Fug78] I.Ya. Fugol'. Excitons in Rare-Gas Crystals. *Advances in Physics*, 27(1):1, 1978.

[Fug88] I.Ya. Fugol'. Free and Self-Trapped Excitons in Cryocrystals: Kinetics and Relaxation Processes. *Advances in Physics*, 37(1):1, 1988.

[GKLS92] G.N. Gerasimov, B.E. Krylov, A.V. Loginov, and S.A. Shchukin. Second VUV Continua of Xenon, Krypton, and Argon Emitted from a Supersonic Jet Excited by a DC Discharge. *Opt. Spectrosc.*, 73(6), 1992.

[Gmi00] E. Gminder. *Lumineszenzspektroscopische Untersuchung der Erzeugung sekundärer Exzitonen in den festen Edelgasen Argon und Neon.* Dissertation, Universität Hamburg, Hamburg, 2000.

[GRZP83] P. Gürtler, E. Roick, G. Zimmerer, and M. Pouey. Superlumi: A High Flux VUV Spectroscopic Device for Luminescence Measurement. *Nuclear Instruments and Methods in Physics Research*, 208(1-3):835, 1983.

[Hag89] H. Hagedorn. *Inbetriebnahme und Test eines orts- und zeitauflösenden Photonendetektors für hochaufgelöste Lumineszenzspektroskopie.* Diplomarbeit, Universität Hamburg, Hamburg, 1989. (Interner Bericht, DESY HASYLAB 89-10).

[Her69] J.C. Hermanson. Two-Quantum Excitations in Alkali Halides. *Physical Review*, 177(3):1234, 1969.

[HHM78] S.S. Hasnain, T.D.S. Hamilton, and I.H. Munro. Absorption Coefficient in the n=1 [$\Gamma(3/2)$, $\Gamma(1/2)$] Exciton Region of Solid Krypton. *Journal of Physics C*, 11(7):L261, 1978.

[HKK+70] R. Haensel, G. Keitel, E.E. Koch, M. Skibowski, and P. Schreiber. Reflection Spectrum of Solid Krypton and Xenon in the Vacuum Ultraviolet. *Optics Communications*, 2(2):59, 1970.

[HS76] V.V. Hizhnyakov and A.V. Sherman. Adiabatic Surfaces and Optical Spectra of Self-Trapping Excitons. *Trudy Inst. Fiz. Akad. Nauk Estonian SSR*, 46:120, 1976.

[ILL65] E.R. Ilmas, G.G. Liidya, and Ch. B. Lushchik. Photon Multiplication in Crystals. I and II. *Opt. Spectrosc.*, 18:255;359, 1965.

[Kam89] S. Kampf. Bedienungsanleitung für den schnellen mechanischen Chopper. Technical Report Interner Bericht, DESY HASYLAB 89-01, 1989.

[Kar93] R. Karnbach. *Strahlender Zerfall und Relaxation von Edelgasclustern untersucht mit Methoden der Lumineszenzspektroskopie.* Dissertation, Universität Hamburg, Hamburg, 1993. (Interner Bericht, DESY HASYLAB 93-11).

[KDS95] M.J. Kiik, P. Dube, and B.P. Stoicheff. Spectroscopic Study of Rare-Gas Excimer Formation in a Direct-Current Discharge with Supersonic Expansion. *The Journal of Chemical Physics*, 102(6):2351, 1995.

[KG91] M. Kraas and P. Gürtler. Rare-Gas-Exciplex-Hydrides in Rare-Gas Matrices: Luminescence Spectra and Radiative Lifetimes. *Chemical Physics Letters*, 183(3,4):264, 1991.

[Kit86] C. Kittel. *Introduction to Solid State Physics*. John Wiley and Sons, New York, 6th edition, 1986.

[KKK+97] M. Kink, R. Kink, V. Kisand, J. Maksimov, and M. Selg. Recombination luminescence of rare gas crystals. *Nuclear Instruments and Methods in Physics Research B*, 122:668, 1997.

[KKLN87] R. Kink, K. Kalder, A. Lôhumus, and H. Niedrais. Effect of Pressure on the Luminescence of Trapped Excitons in Xe Crystals. *physica status solidi (b)*, 139:321, 1987.

[Kli95] C.F. Klingshirn. *Semiconductor Optics*. Springer Verlag, Berlin Heidelberg, 1995.

[Klo89] T. Kloiber. *Erosion fester Edelgase durch Photonenstimulierte Desorption neutraler Edelgasatome und -moleküle*. Dissertation, Universität Hamburg, Hamburg, 1989. (Interner Bericht, DESY HASYLAB 89-09).

[KM73] A.B. Kunz and D.J. Mickish. Study of the Electronic Structure and the Optical Properties of the Solid Rare Gases. *Physical Review B*, 8(2):779, 1973.

[KMC97] A.V. Kanaev, L. Museur, and M.C. Castex. Size-Effects on Energy Relaxation and Excited-Species Desorption in Krypton Clusters: Fluorescence Lifetime Measurements with 10 eV Laser Excitation. *The Journal of Chemical Physics*, 107(10):4006, 1997.

[Kno63] R.S. Knox. *Theory of Excitons*, volume 5 of *Solide State Physics*. Academic Press, New York and London, 1963.

[Kör97] S. Körding. *Lumineszenzspektroskopische Untersuchung der Erzeugung und Relaxation elektronischer Ein- und Mehrfachanregungen in festem Xenon*. Diplomarbeit, Universität Hamburg, Hamburg, 1997.

[KS79] R. Kink and M. Selg. Polariton Effects in Crystalline Xenon. *physica status solidi (b)*, 96:101, 1979.

[KS87] H.J. Kmiecik and M. Schreiber. Tunneling through the self–trapping barrier in rare gas solids. *Journal of Luminescence*, 37:191, 1987.

[Kun79] C. Kunz, editor. *Synchrotron Radiation Techniques and Applications*, volume 10 of *Topics in Current Physics*. Springer, 1979.

[KV76] M. L. Klein and J. A. Venables, editors. *Rare Gas Solids*, volume I. Academic Press, London, 1976.

[KV77] M. L. Klein and J. A. Venables, editors. *Rare Gas Solids*, volume II. Academic Press, London, 1977.

[Laa92] W. Laasch. *Fluoreszenzspektroskopische Untersuchung der Elektron–Phonon–Wechselwirkung in Ar-, Kr- und Xe- dotierten Edelgasmatrizen*. Dissertation, Universität Hamburg, Hamburg, 1992. (Interner Bericht, DESY HASYLAB 92-07).

[LFK+96] A. Lushchik, E. Feldbach, R. Kink, Ch. Lushchik, M. Kirm, and I. Martinson. Secondary excitons in alkali halide crystals. *Physical Review B*, 53(9):5379, 1996.

[LGM+89] P. Laporte, P. Gürtler, E. Morikawa, R. Reininger, and V. Saile. Time- and Energy–Resolved Luminescence of the XeKr Exciplex. *Europhysics Letters*, 9(6):533, 1989.

[LKL95] A. Lushchik, M. Kirm, and Ch. Lushchik. Multiplication of Anion and Cation Electronic Excitations in Luminescent Wide-Gap Ionic Crystals. *Radiation Measurements*, 24(4):365, 1995.

[Mar88] G. Margaritondo. *Introduction to Synchrotron Radiation*. Oxford University Press, New York, 1988.

[MHS68] L.S. Miller, S. Howe, and W.E. Spear. Charge Transport in Solid and Liquid Ar, Kr, and Xe. *Physical Review*, 166(3):871, 1968.

[Mik87] V.V. Mikhailin. Excitation of Secondary Processes in the Vacuum Ultraviolet Range. *Nuclear Instruments and Methods in Physics Research*, A261:107, 1987.

[MKZ85] T. Möller, T. Kloiber, and G. Zimmerer. SUPERLUMI: Der neue 1-m Monochromator zur Fluoreszenzanalyse ist in Betrieb. HASYLAB Jahresbericht, 1985.

[Möl86] T. Möller. *Reaktive Stöße in Elektronisch Angeregten Edelgas-Wasserstoff-Gemischen: Bildung und Zerfall der Edelgashydride*. Dissertation, Universität Hamburg, Hamburg, 1986. (Interner Bericht, DESY HASYLAB 86-07).

[Moo58] C.E. Moore. Atomic energy levels. *National Bureau of Standards*, 467, 1949-1958.

[Mot38] N.F. Mott. *Proceedings of the Royal Society of London A*, 167:384, 1938.

[MRG+89] E. Morikawa, R. Reininger, P. Gürtler, V. Saile, and P. Laporte. Argon, Krypton, and Xenon Excimer Luminescence: From the Dilute Gas to the Condensed Phase. *The Journal of Chemical Physics*, 91(3):1469, 1989.

[Mul70] R.S. Mulliken. Potential Curves of Diatomic Rare-Gas Molecules and Their Ions, with Particular Reference to Xe_2^*. *The Journal of Chemical Physics*, 52(10):5170, 1970.

[NF85] G. Nowak and J. Fricke. The Heteronuclear Excimers ArKr*, ArXe* and KrXe*. *Journal of Physics B*, 18:1355, 1985.

[NGDM75] J.D. Nuttall, T.E. Gallon, M.G. Devey, and J.A.D. Matthew. The electron energy loss spectra of the solid rare gases for low primary beam energies. *Journal of Physics C*, 8:445, 1975.

[NT81] K. Nasu and Y. Toyozawa. Tunneling Process from Free State to Self-Trapped State of Exciton. *Journal of the Physical Society of Japan*, 50(1):235, 1981.

[NTA80] S. Nakajima, Y. Toyozawa, and R. Abe. *The Physics of Elementary Excitations*, volume 12 of *Springer Series in Solid-State Sciences*. Berlin Heidelberg, 1980.

[PJPP86] P. Plenkiewicz, J.-P. Jay–Gerin, B. Plenkiewicz, and G. Perluzzo. Electron mean free path and conduction–band density of states in solid argon. *Solid State Communications*, 57(3):203, 1986.

[Rad97] L. Rade. *Springers mathematische Formeln*. Springer, 1997.

[Ras81] E.I. Rashba. Self-Trapping of Excitons in Solids. In V.M. Tuchkevich and K.K. Shvarts, editors, *Defects in Insulating Crystals*. Zinatne / Springer, 1981.

[Ras82] E.I. Rashba. Self-Trapping of Excitons. In E.I. Rashba and M.D. Sturge, editors, *Excitons*, page 543. North Holland Publish. Comp., Amsterdam, 1982.

[Rat96] A.M. Ratner. Free Atoms and the Simplest Atomic Crystals. *Physics Reports*, 269:197, 1996.

[RGK+99] I. Reimand, E. Gminder, M. Kirm, V. Kisand, B. Steeg, D. Varding, and G. Zimmerer. An Analysis of Electron-Hole Recombination in Solid Xenon with Time-Resolved Luminescence Spectroscopy. *physica status solidi (b)*, 214:81, 1999.

[Roi84] E. Roick. *Relaxationsprozesse in festen Edelgasen untersucht mit energie- und zeitaufgelöster Lumineszenzspektroskopie*. Dissertation, Universität Hamburg, Hamburg, 1984. (Interner Bericht, DESY HASYLAB 84-07).

[Rös70] U. Rössler. Electron and Exciton States in Solid Rare Gases. *physica status solidi*, 42:345, 1970.

[Run97] M. Runne. *Dynamik angeregter Edelgasatome auf der Oberfläche Edelgas-dotierter Edelgasfestkörper*. Dissertation, Universität Hamburg, Hamburg, 1997. (Interner Bericht, DESY HASYLAB 97-04).

[SA73] I.T. Steinberger and U. Asaf. Band-Structure Parameters of Solid and Liquid Xenon. *Physical Review B*, 8(2):914, 1973.

[Sai76] V. Saile. *Optische Anregungen der Valenzelektronen von Argon, Krypton und Xenon in festem und gasförmigem Zustand zwischen 6 eV und 20 eV*. Dissertation, Universität München, München, 1976.

[Sai80] V. Saile. One- and two–photon spectroscopy with rare gas solids. *Applied Optics*, 19(23):4115, 1980.

[Sam67] J.A.R. Samson. *Techniques of Vacuum–Ultraviolet Spectroscopy*. Wiley, London, New York, Sydney, 1967.

[Sch76] N. Schwentner. Mean–free path of electrons in rare–gas solids derived from vacuum-uv photoemission data. *Physical Review B*, 14(12):5490, 1976.

[SE98] J.A. Samson and D.L. Ederer, editors. *Vacuum Ultraviolet Spectroscopy I*. Experimental Methods in Physical Sciences. Academic Press, 1998.

[Sel81] M. Selg. *Relaxation and Hot Luminescence of Self-Trapped Excitons in Rare Gas Crystals.* Dissertation, Institute of Physics, Tartu, 1981.

[SGK+99] B. Steeg, E. Gminder, M. Kirm, V. Kisand, S. Vielhauer, and G. Zimmerer. Creation of electronic polaron complexes in solid xenon observed in free-exciton luminescence under selective photon excitation. *Journal of Electron Spectroscopy and Related Phenomena*, 101-103:879, 1999.

[SHK+00] M. Selg, V. Hizhnjakov, R. Kink, M. Kink, and J. Maksimov. Stationary and Time-Resolved Hot Luminescence of Self-Trapped Excitons in Rare Gas Solids. *Journal of Low Temperature Physics*, 2000.

[Sho61] W. Shockley. Problems Related to P-N Junctions in Silicon. *Czech. J. Phys. B*, 11:81, 1961.

[SHS+75] N. Schwentner, F.J. Himpsel, V. Saile, M. Skibowski, W. Steinmann, and E.E. Koch. *Physical Review Letters*, 34(9):528, 1975.

[SKJ85] N. Schwentner, E.E. Koch, and J. Jortner. *Electronic Excitations in Condensed Rare Gases*, volume 107 of *Springer Tracts in Modern Physics*. Springer-Verlag, Berlin Heidelberg, 1985.

[SMW77] I.T. Steinberger, P. Maaskant, and S.E. Webber. Optical Constants of Solid Krypton. *The Journal of Chemical Physics*, 66(10):4722, 1977.

[SOGG94] E.V. Savchenko, A.N. Ogurtsov, O.N. Grigorashchenko, and S.A. Gubin. Electronically induced defect formation in Xe–doped solid Kr. *Chemical Physics*, 189:415, 1994.

[SRLB92] D.W. Snoke, W.W. Rühle, Y.-C. Lu, and E. Bauser. Evolution of a nonthermal electron energy distribution in GaAs. *Physical Review B*, 45(19):10979, 1992.

[Ste99] B. Steeg. *Erzeugung sekundärer Exzitonen in festem Xenon untersucht mit Hilfe der Lumineszenzspektroskopie.* Dissertation, Universität Hamburg, Hamburg, 1999. (DESY -THESIS-2000-005).

[SW71] S.R. Scharber and S.E. Webber. Optical Constants of Simple Molecular Crystals. II. Results for Kr and Xe. *The Journal of Chemical Physics*, 55(8):3985, 1971.

[Var94] D. Varding. *Lumineszenzspektroskopische Untersuchungen dynamischer Eigenschaften freier Exzitonen in den festen Edelgasen Krypton und Xenon*. Dissertation, Universität Hamburg, Hamburg, 1994. (Interner Bericht, DESY HASYLAB 94–05).

[Vas00] A.N. Vasil'ev. Private Communication. 2000.

[VBF+93] D. Varding, J. Becker, L. Frankenstein, B. Peters, M. Runne, A. Schröder, and G. Zimmerer. Free-exciton luminescence of solid xenon and solid krypton. *Low Temp. Phys.*, 19(5):427, 1993.

[VFM99] A.N. Vasil'ev, Y. Fang, and V.V. Mikhailin. Impact production of secondary electronic excitations in insulators: Multiple-parabolic-branch band model. *Physical Review B*, 60(8):5340, 1999.

[Vie02] S. Vielhauer. Dissertation, Universität Hamburg, Hamburg, 2002. (in preparation).

[VRZ94] D. Varding, I. Reimand, and G. Zimmerer. Time–Resolved Luminescence of Exciton–Polaritons in Solid Xenon. *physica status solidi (b)*, 185:301, 1994.

[Wan37] G.H. Wannier. The Structure of Electronic Excitation Levels in Insulating Crystals. *Physical Review*, 52:191, 1937.

[WBHS83] H. Wilcke, W. Böhmer, R. Haensel, and N. Schwentner. High Flux and High Resolution VUV Beamline for Luminescence Spectroscopy. *Nuclear Instruments and Methods in Physics Research*, 208:59, 1983.

[Zim62] J.M. Ziman. *Electrons and Phonons: The Theory of Transport Phenomena in Solids*. Clarendon, 1962.

[Zim87] G. Zimmerer. Creation, motion and decay of excitons in rare gas solids. In U. M. Grassano and N. Terzi, editors, *Excited state spectroscopy in solids*, page 37, Amsterdam, 1987. North Holland Physics Publishing.

[Zim91] G. Zimmerer. Status report on luminescence investigations with synchrotron radiation at HASYLAB. *Nuclear Instruments and Methods in Physics Research*, A308:178, 1991.

Acknowledgments

First of all, I am grateful to my supervisor Professor Dr. Georg Zimmerer for his guidance, support and continuous interest in my research.

My special thanks belong to Dr. Marco Kirm for many experimental tips, stimulating discussions, innumerable coffee-times, and proof-reading of my work.

I would like thank all members of the SUPERLUMI team for a pleasant and stimulating working atmosphere. Especially I would thank Dr. Barbara Steeg, who supported me during my first beamtime at SUPERLUMI. Also the help and support by Sebastian Vielhauer, Dr. Elke Gminder and Evgueni Negodine is acknowledged.

I am grateful to Dr. Rein Kink, Dr. Matti Selg, Professors Cheslav and Aleksandr Lushchik from Institute of Physics in Tartu for stimulating discussions. Dr. Andrey Vasil'ev is acknowledged for the extensive discussion of MPBB model.

Finally I can not forget Mare, my family and all my friends who supported me during last years.

This work was supported by the *Deutsche Forschungsgemeinschaft* (DFG) under project numbers DFG-Zi 159/2-1, 2-2, and 2-3.